Understanding the Sensitivity of Detachment location to External Control on JET

Simon Orchard

Doctor of Philosophy
University of York
Physics, Engineering and Technology

April 2021

Abstract

In this thesis, comparisons of predictions of detachment front location sensitivity model ('DLS model'[1]) were made in one L-mode (no N_2-seeding), and three H-mode detached discharges (N_2-seeding). Although the DLS model and experiment are qualitatively in agreement the model overestimates the sensitivity of the movement along a field line for a given amount of change in two control variables – upstream density, n_u and the power entering the scrape-off layer, P_{SOL}. The quantitative mismatch between the DLS model and experiment is not unexpected given the simplicity of the DLS model. Under the assumption that the exponents of n_u & P_{SOL} in the DLS model could be incorrect, new exponents were derived for both control variables from the L-mode experimental data in periods of the L-mode case where first only n_u, and then both n_u & P_{SOL} were varied. The new 'empirical' exponents were reduced from the DLS predictions by a factor of ∼2.5. Those 'empirical' exponents in the DLS model were then applied to the prediction of divertor impurity concentration, f_z for two H-mode cases which had divertor N_2-seeding show reasonable consistency with the variation in core Z_{eff} and variations in P_{SOL}.

As part of this work, a measure for the detachment front location was developed based on the transition of the ratio of $\frac{D_\gamma}{D_\alpha}$ emissivities from high (recombination-dominated) to low (excitation-dominated). The detachment extent along a field line, $\hat{z}$, was found to be inversely proportional to the outer divertor total ion current which may lead to new insights to the relationship between detachment and target ion current loss. The quality of this relationship was unexpected due to many nonlinear divertor processes that could have affected it.

Declaration

I declare that this thesis is a presentation of original work and I am the sole author. This work has not previously been presented for an award at this, or any other, University. All sources are acknowledged as references.

Parts of this thesis were adapted from a paper in progress.

Acknowledgements

I can't thank my supervisors Professor Bruce Lipschutz and Dr James Harrison enough for all their hard work and patience to help me progress the research in this thesis. I know it must not have been easy for them and all their help means so much.

Friends I have made during the course of my study on the fusion CDT, my housemates, and my family have all supported me through my studies and I don't think I'd have finished without the people who have been with me every step of the way.

I would like to additionally thank Stuart Henderson for specifically getting nitrogen concentration measurements where he could and Chris Bowman for showing me the Bayesian way and helping with stored energy measurements. I would like to thank the JET team for the experimental data that was taken.

This work was funded by the United Kingdom Engineering and Physical Sciences Research Council under grant EP/L01663X/1 and the European Communities under the contract of Association between EURATOM and CCFE. The views and opinions expressed herein do not necessarily reflect those of the European Commission.

Contents

1 Introduction

Momentum in fusion energy research has risen significantly in recent years. This can be seen in the increased public interest in current fusion research, and significant funding from government[2] and private companies[3] to new fusion projects[4]. Ongoing international projects like ITER and DEMO[5], which have many years of advanced planning[6], are partially transferable to others. Motivation for fusion energy comes from the fact that the fuel requires only raw materials of Lithium and Deuterium which can be extracted from seawater. Fusion can produce a large amount of energy in a fundamental reaction that occurs regularly throughout the universe. This is enforced through the fact that no greenhouse gases are released in the process, and has the potential to bypass the negativity of past fission reactors concerns of nuclear proliferation, high level radioactive waste and no possibility of a runaway reaction.

Fusion reactions produce energy due to the slight difference in mass between the sum of individual reactants and the mass of the combined nucleus, which releases energy according to Einstein's equation $E = mc^2$. This fundamentally favours the lower atomic number Z atoms to release more energy up until Z reaches a stable iron nucleus. To fuse together, the reactant ions must exceed (or tunnel through) the coulomb repulsion. Two ions must reach a proximity that allows the strong nuclear force to exceed the coulomb force to fuse together, so having highly energetic ions is a prerequisite.

Producing efficient fusion on Earth fundamentally requires high temperatures and densities for a long enough period of time to provide sufficient energy from fusion products, which can then maintain those high temperature conditions indefinitely. Getting plasma to conditions for more energy out than in (ignition) has not been achieved yet on earth, but a number of avenues of research exist. The gravitational confinement in stars can produce temperatures and densities high enough hydrogen fusion to occur extremely slowly[7] compared to what would be required for a reactor. Inertial confinement fusion (ICF) has much shorter confinement times but higher density[8]. The focus of this thesis is on magnetic confinement fusion (MCF). Plasma confinement using magnetic fields requires keeping high temperature ($>$ 100 million K) plasma away from any solid surfaces. At these temperatures, matter reaches the plasma state separating electrons and from their ions and can be influenced by electric and magnetic fields. In this category of magnetic confinement, tokamaks have had the most research[9] and success to date compared to the alternative concepts such as the Stellarator[10] and most plans for future scaling to ignition relevant conditions involve tokamaks.

1.1 Reaching conditions for ignition

Achieving the ignition condition requires a fusion plasma to remain sustained from heat from the by-products of fusion reactions alone, so the power from fusion products must be equal to or greater than power loss. Power loss of $\frac{3nk_bT_{i/e}V}{\tau_E}$ is approximated from the thermal energy of electrons and ions $(\frac{3}{2}nk_bT_{i/e})$[11], the plasma volume V and the energy confinement time τ_E where k_b is the Boltzmann constant, and ions and electrons are assumed to be at the same temperature T and density n. The power from confined fusion products (alpha particles) is $\frac{n^2}{4} < \sigma v > E_r$ from a reaction rate of $n_1n_2 < \sigma v >$, where successful collisions have a reactivity $< \sigma v >$. Each reactant density n_1 and n_2 can be assumed equal, and E_r is the energy carried confined fusion products. The balance can be rearranged to $nT\tau_E = \frac{12k_bT^2V}{<\sigma v>E_r}$ which is known as the fusion triple product[11;12].

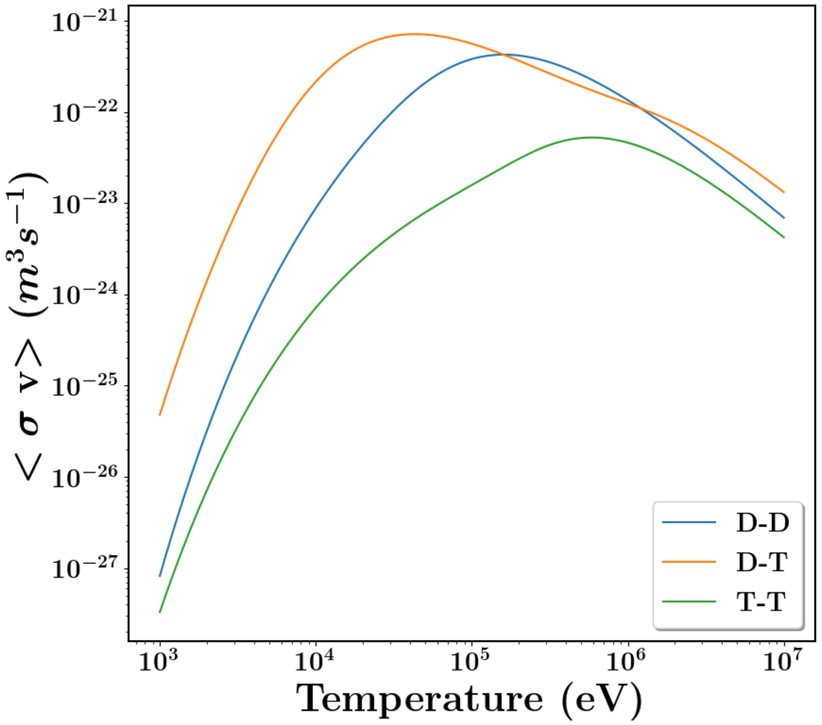

Figure 1: The reaction rate of three fusion reactions, showing that D-T fusion has a higher reactivity at lower temperature[13].

Chosen fusion fuels are efficient at the lowest possible temperature to minimise the required heating power and plasma temperature for the highest reaction rate. The reaction in proton-proton ($^1_1$H) fusion is too slow to be considered for a rector, but other hydrogen isotopes, Deuterium D ($^2_1$H) and Tritium T ($^3_1$H), are more favourable. Reactivity $< \sigma v >$, for each particle with velocity v averaged over a Maxwellian distribution, for combinations of reactants are shown in figure 1. A fitted form of cross-section $\sigma(E)$[13] as a function of energy E is integrated, assuming a Maxwell-Boltzman distribution of velocities with both reactants at the same temperature. The peak of the D-T reaction reaches a higher reactivity and at a much lower temperature, which makes it an ideal reaction to achieve a good reaction rate.

The reaction for D-T fusion in equation 1 shows the energy split due to momentum conservation that produces a 14MeV neutron and an alpha particle ($^4_2$He). The D-D reaction is made up of several separate reactions that would eventually reach ($^4_2$He). There is less energy released in D-D fusion[14], so the neutrons in this reaction have reduced energies compared with D-T fusion.

$$^2_1\mathrm{D} +^3_1\mathrm{T} \rightarrow^4_2 \mathrm{He}(3.52\mathrm{MeV}) +^1_0 n(14.06\mathrm{MeV}) \tag{1}$$

Deuterium is naturally present in seawater[15] because of its nuclear stability, but the half-life of Tritium of ~ 13[16] years means there is a limited supply and is only available when produced. The reaction(s) of lithium and a neutron produce Tritium which means lithium is considered a Tritium "breeder" material which will likely line the edge of future fusion reactors to capture neutrons for Tritium breeding[14]. This is why both Deuterium and Tritium can be considered sustainable.

1.2 Tokamak magnetic confinement

The movement of charged particles in a magnetic field is helical around magnetic field lines, so that the centres of their orbits are mostly moving in the direction of the field lines. To reduce losses from a fusion device, field lines are bent around and connected end to end, but in doing so creates a gradient of magnetic field ∇B between field lines of different magnetic field strength. A magnetic field can be generated by magnetic field coils on a tokamak, which are poloidally structured to generate a toroidal field, where the toroidal and poloidal direction is shown in figure 3a. With a toroidal field alone, the ∇B of the magnetic field causes drifts which would lead to loss of particle confinement[11].

To counteract drifts, one magnetic confinement device called a Stellarator uses angled geometry[17] of different coils, but in a tokamak, the plasma itself is relied upon to achieve this effect.The poloidal magnetic field is introduced by a current in the plasma that is generated due to the movement of confined charged particles. This plasma current is induced on start up by varying the current through the central solenoid by "ramping up" the magnetic field. Current tokamaks are not designed for steady state operation, but operate in separate "pulses" also called shots or discharges. Charged particles which follow the resultant total magnetic field are shown in figure 2.

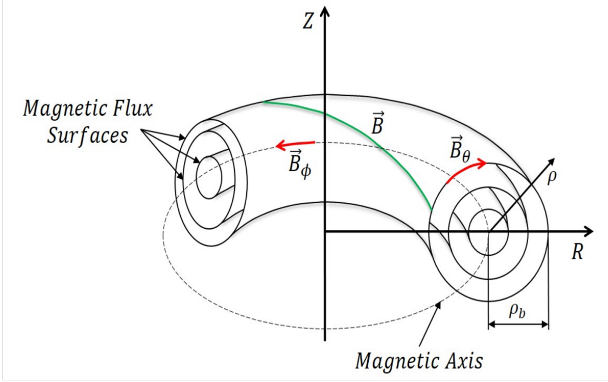

Figure 2: Representation of toroidal magnetic flux surfaces in a tokamak plasma. With the magnetic axis as the central flux surface at the plasma core. The toroidal and poloidal magentic field directions are represented on the flux surfaces.[18]

$$\psi_p = \int_S \mathbf{B_p}.\mathbf{dA} \tag{2}$$

The magnetic field lines lie on surfaces of constant magnetic flux defined in equation 2[19] as the poloidal flux through an circlular surface S extending from R=0 outwards at a given Z. The gradient in flux is perpendicular to the path of magnetic field lines, so the constant regions of flux that the magnetic field lines are on are referred to as toroidal "Flux surfaces" shown in figure 2. Flux surfaces therefore appear as nested layers in the poloidal plane that extend from a central point in the plasma called the magnetic axis also shown in figure 2. Extending outwards from the magnetic axis in the R direction is defined as the "midplane". This magnetic field structure is referred to as "The equilibrium" from now onwards.

Flux surfaces closer to the magnetic axis will not intercept any solid objects (a closed flux surface), and flux surfaces that make contact with a solid object are open flux surfaces. The last closed flux surface (LCFS) is the closed flux surface defined before the transition to open flux surfaces. Normalised flux Ψ_n, which is zero at the magnetic axis and one at the LCFS, is used as a reference flux in the equilibrium. The scrape-off layer (SOL) is the range of open flux surfaces after the LCFS. Figure 3b shows some reference positions of key flux surfaces. Due to transport mechanisms[20], particles and heat will be transported across flux surfaces to the plasma's edge while retaining their high parallel velocity towards a solid surface.

Limiters were the first dedicated armour used to protect plasma-facing components (PFCs) and limit core losses, but they are still used in some regimes and during plasma start-up. A limiter intercepts the separatrix at a lower flux surface, limiting the position of the LCFS. The limiter still makes

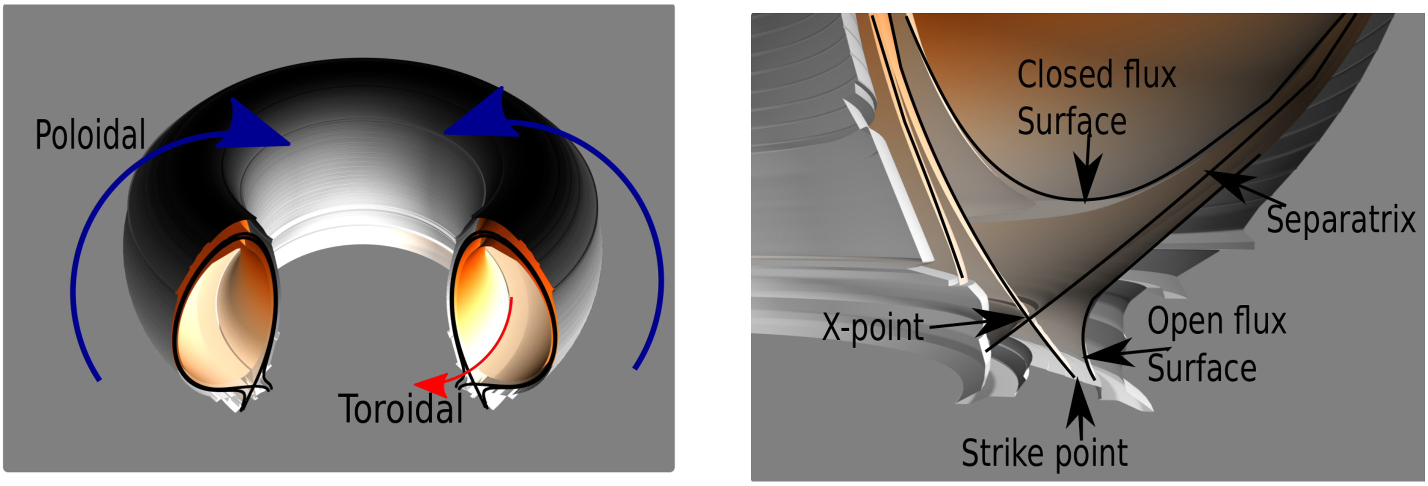

(a) Visualisation of the toroidal and poloidal directions in a tokamak

(b) Visualisation of the tokamak flux surfaces close to the X-point and key surrounding flux surfaces

Figure 3

contact near closed flux surfaces, where sputtered material off limiters can cause energy confinement loss in the core.

Introducing another magnetic field is a solution to keeping the confined plasma from direct contact with materials. An additional poloidal field can "divert" the flux surfaces from the LCFS and outwards into the SOL so that the intersection of the field lines does not reach a solid surface until passing far away from the core plasma. This configuration is called a divertor. All the fast-moving plasma can now pass along field lines uninterrupted until it has reached a position far from the plasma core and reaches the divertor target plate at the strike point. The introduction of this poloidal field produces a magnetic null point called an 'X-point' that lies on the boundary between open and closed flux surfaces called the "separatrix". Tokamak magnetic field configurations can operate in single (1 X-point typically below the core plasma) or double null (X-points above and below the core) configuration. Additional X-points can be introduced in these regions to produce special configurations such as the snowflake configuration[21]. Figure 4 shows the positioning of some key features for a single null X-point.

If the core plasma is separated by a physical barrier from the strike point to contain recycled neutrals[22], the divertor is considered "closed". This has an impact on keeping impurities and neutrals in the divertor region instead of more easily reaching the core[23].

Plasma heating will affect the core confinement, as the shift from resistive heating of the plasma (ohmic) and radio frequency (e.g. ion cyclotron resonance heating ICRH) to more heating from neutral beam injection (NBI) can lead to a increase in the energy and particle confinement from low

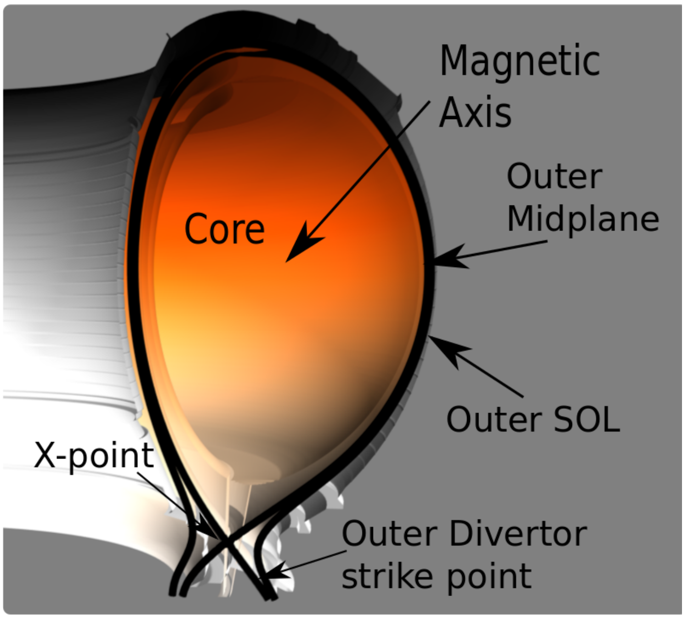

Figure 4: Visualisation of the tokamak with key points labelled.

confinement (L-mode) to high confinement (H-mode). Larger tokamaks are more likely to operate in H-mode than L-mode to achieve high performance, but it has drawbacks. In H-mode there is a much steeper gradient in densities and temperatures between flux surfaces approaching and crossing the LCFS in a region called the pedestal. Instabilities driven by pedestal gradients cause edge localised modes (ELMs) that cause the transport barrier to collapse and release power and particles onto open flux surfaces. ELMs collapse the density and temperature profiles in the pedestal during the intra-ELM period to build them back up between ELMs in the inter-ELM period, causing monetarily high heat fluxes. One measure of the confinement $\beta = \frac{p}{(B^2/2\mu_0)}$, the ratio of the plasma pressure the magnetic pressure increases after reaching the power threshold for an L-H transition P_{L-H}.

1.3 Controlling the divertor

The divertor concept described so far provides significant benefits to core confinement compared to non-divertor solutions; however, engineering constraints on the edge of the plasma also have to be considered. Heat fluxes to surfaces cannot significantly exceed values of the order $10MWm^{-2}$ [24] before causing unacceptable divertor target damage and erosion. Higher SOL power in large reactors would need a larger SOL channel that the power flows through, called the scrape-off-layer radial width λ_q [25] [26], for the same heat fluxes. Without further reductions in heat fluxes, target heat and particle fluxes could rise beyond the material limits. Larger reactors may face challenges from scaling scrape-off-layer radial width λ_q [27]. Reducing target heat fluxes through changing the geometry of the SOL to increase the divertor outer leg length, the effects of total flux expansion [28] and/or moving the strike point over the divertor tiles repeatedly (known as strike point sweeping[29]) aids the heat flux problem. However, more reductions are most likely required. Reductions to target parallel heat fluxes through detachment (described in chapter 2) on current devices may come at the cost of incurring some core confinement degradation[30]. For large devices, such as ITER and DEMO, divertor heat fluxes will need even greater reductions with a minimised effect on the core. In these cases it may also be important to have sophisticated control of the level of detachment. It is predicted that ITER will require some level of detachment for operation[31;24].

Target heat fluxes can be reduced by spreading more energy and particles away from the divertor target. During detachment, a lower pressure region expands from the target towards the X-point due to neutrals and impurities, increasing the potential energy dissipation. The sharp temperature gradient parallel to the field lines is called the "thermal front". By increasing the level of detachment, the radiating region that largely follows the temperature gradient moves from the target towards the X-point and becomes closer to the confined plasma. The radiating region is useful for dispersing energy in the divertor. Closer to the X-point, energy can also be lost from the core plasma, potentially reducing confinement. Keeping the thermal front at an optimised location between the target and X-point will be a trade-off between reducing the heat flux enough and not excessively degrading core energy confinement[32;33;34;35;36;37;22;38;39;40;41] through exposing the core to excessive neutral and impurities present at lower temperatures regions[32;33;34;36;42;43;44;45;41]. Divertor impurity compression reduces impurity transport to the core[46] while also allowing the divertor to pump helium. Impurity compression can be negatively affected by increased levels of detachment[47;48;49;50;51]. To optimally position the thermal front along the divertor leg, an understanding of how to manipulate thermal front movement based on a set of control parameters needs to be developed.

The choice of detachment state measurement to act as a sensor in a detachment control feedback system depends on whether a measured parameter can respond to control parameter changes. Detachment state measurements must represent either a low temperature, particle or heat flux, indicating changes in the plasma state during detachment. The temperature profile predominantly sets emission and radiation profiles, and the thermal front can be passively observed. Transitioning to a deeper detached regime will move radiation and emission fronts from the target towards the X-point. It makes sense to track either the total emission, a specific atomic transition representing temperature, or the ion flux to the target. These different measures for the state of detachment can vary in studies that aim to control detachment onset or a state of deeper detachment.

Detachment onset occurs when an expected increase to target particle flux for an attached plasma is a decrease in particle flux and begins to detach, known as "rollover". The transition is not instant, as the rate of ion flux increase gradually starts to drop. Using the target ion current[52] [53] to develop real-time control is effective, as during detachment the ion current drops after rollover, but it must be established after a rollover point. The ion target current can be used to estimate the heat fluxes, or as an estimate of the divertor temperature[54] [33], making it useful for measuring the state of detachment. High-frequency signals can be used to resolve the state of detachment intra-ELM and inter-ELM (during an ELM event and after respectively).

Instead of measuring the target conditions, the X-point conditions are influenced by the detachment state, so can be used as a sensor, e.g. by keeping radiation levels measured by bolometers[36] [42] or other radiation detection methods[55] within some bounds. Increasing the spatial coverage of bolometer chords to measure the total divertor radiation for feedback control with impurity seeding[56] has also been used for control. These methods are specifically aimed to prevent the radiation becoming too strong near the X-point, which can lead to a reduction in confinement[57].

More recent methods have shown that higher frame rate cameras can be used to control the detachment front when filtered for specific wavelengths[58;59;60;61]. The C-III (465 nm) brightness images of the divertor are identified as a transition more dominantly dependent on temperature. Along a flux tube, the position that C-III brightness drops to 50% of the maximum value between the C-III peak and the target is used as a measure of detachment front location. This measurement is well-defined before the onset of detachment with low or no emission and then increasing afterwards, but it needs a carbon source.

For control parameters to be most effective, they should be easily changed and affect the state of divertor detachment on a short time scale. Experiments almost always use an impurity, usually N_2-seeding as an actuator.

In Lipschultz et al. [2016] the change of a control parameter predicted to move the detachment front from the target at detachment onset to the X-point is derived. The total change in a control parameter required to move the detachment front from the target to the X-point is known as the "detachment window". The rate of the position change with a change in control parameter is known as the "detachment sensitivity", and both window and sensitivity are introduced in section 2. The model also includes terms for the magnetic field on a flux surface, potentially making it useful for predicting the sensitivity of detachment to external control in different divertor magnetic geometries.

Detachment windows have been observed in ranges of core line averaged densities[62] or by considering NII line intensity changes in the divertor[63]. More information about detachment windows for a greater range of parameters can be investigated by considering more pulses (experimental plasma discharges). It may be a problem using one single parameter for control; for example, if only impurity concentration was used as a control parameter, then increasing it too much is detrimental to core energy confinement. The need for flexibility for detachment control will therefore be key for optimising it, so in this thesis, investigations are made using multiple control parameters based on what is predicted to cause the detachment front to move from Lipschultz et al. [2016].

1.4 Relevance of this thesis for detachment control

The importance of getting desired low level of target heat fluxes, but not at the cost of excessive core confinement loss, means the analytical model in Lipschultz et al. [2016] is of interest for detachment control research. The model has not previously been evaluated experimentally, which requires diagnostic information from the divertor, midplane and geometry throughout.

In this thesis, the detachment front position is measured and compared to control parameters from the model: power entering the scrape-off layer P_{SOL}, upstream density n_u and impurity concentration f_z. These control parameters are found in a way to reasonably compare to the model in Lipschultz et al. [2016], then the detachment window and sensitivity are measured and compared. Data shown in this thesis are aimed to pinpoint changes in each control variable separately before combining each contribution together.

The front position is measured by tracking the ratio $\frac{D_\gamma}{D_\alpha}$ emission in the divertor. A recombining plasma is much colder than an excitation emission-dominated one. Without considering molecular effects, the deuterium Balmer line D_γ increases proportionally more than D_α with reduced temperature. The ratio $\frac{D_\gamma}{D_\alpha}$ dropping from the target to the X-point represents an increase in temperature because of a decrease in the relative amount of recombination to excitation. This is justified as a good measure of detachment front location in the thesis by arguments from atomic models and comparison to the total ion flux.

The results of this work suggest that the sensitivity of detachment to external control is lower than predicted for changes in upstream density and power entering the SOL. This section introduces detachment to a level for understanding the motivation of thesis work. However, section 2 will go into detail, from the specific definitions and scalings to details on detachment key processes and analytical models for detachment. Section 3 introduces the camera data, which are the key data used to measure the detachment state in this thesis. The unique method of tracking the detachment front and methods for determining suitable control parameters are outlined in section 4 before comparing measured and DLS predicted detachment front location sensitivity to external control in section 5. A quantitative mismatch was found between the DLS (Detachment location sensitivity) model and experiment in section 5.2.2 but is not unexpected given the simplicity of the DLS model. Given that the sensitivity of detachment to n_u & P_{SOL} changes could be incorrect, new exponents of n_u & P_{SOL} in the DLS model are derived in section 5.3 for both control variables from the L-mode experimental data in periods of the L-mode case where first only n_u, and then both n_u & P_{SOL} were varied. The new 'empirical' exponents were reduced from the DLS model exponents by a factor of ∼2.5. The 'empirical' exponents in the DLS model are applied to predict the divertor impurity concentration f_z in section 5.4, for three H-mode cases which had divertor N_2-seeding. The predictions show reasonable consistency with the variation in core Z_{eff} and variations in P_{SOL} with an agreement between all four analysed pulses. The consequences of the 'empirical' exponents in the DLS model are discussed by scaling to ITER-scenarios in section 6.1, and possible reasons for the new 'empirical' exponents are discussed in section 6.3.

2 Divertor detachment theory

As fusion technology pushes towards the goal of achieving net energy gain, an increase in heat fluxes to divertor surfaces would likely reach the point where damage would be done to divertor surface if no heat flux is dissipated in the SOL or divertor. Scaling the core plasma to meet fusion requirements is essential, but these lead to poor scaling of target heat fluxes, as explained below.

The width of the SOL is defined through heat fluxes parallel to the magnetic field $q_{||}$ that fall at larger distances from the separatrix $r = R - R_{sep}$ because of the slow perpendicular transport in the SOL compared to the fast parallel transport. Assuming an exponential perpendicular decay width only, equation 3[26] represents the fall off of heat flux and approximate SOL width from the fall off width λ_q. The perpendicular profile changes towards the target due to perpendicular transport, but the SOL width λ_q still affects the profile shape[27].

$$q(r) = q_{||} e^{-r/\lambda_q} \tag{3}$$

For sustainable fusion, the power from fusion products P_{fus} must be at least greater than the total input heating power P_{in}. The factor $Q = \frac{P_{fus}}{P_{in}}$ defines how the efficiency of the scenario would perform for a reactor with net energy gain. So far, Q has not reached one yet for "breakeven". Since the record Q was achieved on JET[64], the effort has focused on investigating physics that will improve our understanding of tokamak physics to optimise devices that operate in a parameter space to exceed $Q = 1$ significantly. Q has been shown in engineering models not to be strongly dependent on magnetic field or size R, but primarily increases due to confinement enhancement factors and P_{fus}, which increases for higher core temperature and density[12].

Increasing P_{fus} to achieve better core performance is predicted to impact divertor performance by increasing heat fluxes to the divertor target[65]. More unmitigated heat flux $q_{||}$ increases the power across the separatrix P_{sep}. More P_{sep} decreases λ_q[65]. Even with the geometrical changes in larger devices, λ_q is likely to reduce and increase parallel heat fluxes. λ_q reduction coupled with increases to P_{sep} are likely to produce much higher heat fluxes in devices with larger Q. This means that additional methods will need to be implemented for mitigating this heat flux.

The heat flux needs to be dissipated before reaching the target plate. Operation in a detached regime and novel divertor concepts[66;67] are promising candidates for the power exhaust problem. A detached regime aims to minimise target heat fluxes using available physical and atomic processes in the SOL and divertor while minimising impact on the core performance.

In this section, the atomic and physical processes that are present in different operational regimes are reviewed as the components of divertor detachment. The divertor regimes which use these processes are then described, including the detached regime. These are linked to divertor analytical models, starting with the basic 2-point model before introducing models with radiation and magnetic field dependence.

2.1 Physical and atomic processes in the divertor overview

The processes that affect the transport of heat and particles in the divertor are key to understanding the divertor state and how it can be optimised to reduce heat fluxes. The divertor and SOL geometry is often represented as a straightened-out flux tube between the midplane (upstream) and the target, as shown in figure 5. Processes in the divertor and SOL can change the energy and transport of particles depending on the process considered[68]. It is important to consider these processes and how they can reduce the target particle and power fluxes as much as possible.

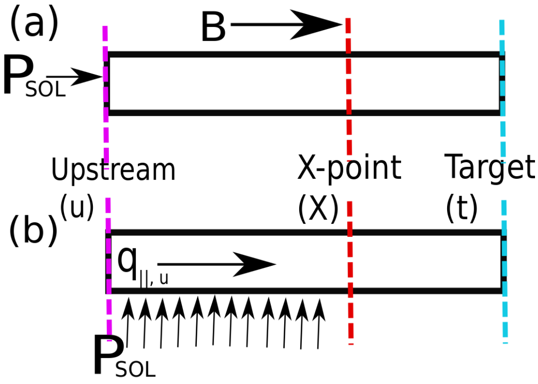

Figure 5: Two simple representations of the SOL and divertor stretched out along a flux tube. Power enters either (a) at the upstream point or (b) between the upstream point and the X-point.

Resonant charge exchange transfers an electron between an ion D_α^+ and neutral D_b^0 in the following process: $\mathbf{D_\alpha^+ + D_b^0 \rightarrow D_\alpha^0 + D_b^+}$. The ions from the core plasma have high energy, and any collision with cold neutral particles has the chance to transfer an electron in a process called charge exchange to produce a hot neutral and cold ion. Lower energy ions will follow the magnetic field to the target, while the high energy neutral that was created will be transported without being bound to the magnetic field, reducing the energy from the hot regions reaching the strike point. The loss of energy helps to reduce the temperature in the SOL.

Neutral hydrogen atoms can be ionised with energy between the current energy level and an excited state through the process of electron ionisation: $\mathbf{e^- + D^0 \rightarrow 2e^- + D^+}$. The energy can be supplied from a photon of the correct wavelength or collisions with electrons. An atom can become ionised with high enough energy transfer if more energy than the potential energy that binds the electron to the atom is transferred. The ion will then follow the magnetic field lines in the tokamak. Ionisation is much more likely to occur at higher temperatures, reducing the downstream electron temperature. More ionisation will increase the number of ions in parts of the SOL but will reduce the temperature, allowing different interactions to occur.

If an atom is excited instead of ionised, the bound electron will relax to a lower energy state after some time and emit a discrete wavelength photon. The magnetic field does not bind this photon, so the total energy is distributed in different directions, reducing the total energy towards the target.

At low enough temperatures below $\sim 1eV$[69], it becomes increasingly likely that ions in the divertor recombine with electrons in the bulk of the plasma. The process reduces the temperature by distributing the resulting neutrals and photons released away from the divertor target. Two paths include radiative recombination: $\mathbf{e^- + D^+ \rightarrow D^0 + h\nu}$ and three-body recombination: $\mathbf{e^- + e^- + D^+ \rightarrow D^0 + e^- + h\nu}$

Similarly to charge exchange, elastic collisions between an atom and ion will transfer momentum and energy between the faster population of ions to neutrals in the process $\mathbf{D_\alpha^{+,0}(\tilde{v}_1) + D_b^0(\tilde{v}_2) \rightarrow D_b^0(\tilde{v}_2^{'}) + D_b^0(\tilde{v}}$ where $\vec{v}_1 \neq \vec{v}_1^{'}$ and $\vec{v}_2 \neq \vec{v}_2^{'}$. These cause the momentum in the plasma to reduce along the field line.

Under low temperature conditions, molecules are present in the plasma and increase the number of possible interactions. Some possible interactions are similar to those described above, but with additional dependence of the vibrational state of the molecule[70]. These molecular reactions are not predicted to be an important power sink compared to processes such as impurity radiation[71], but are diagnostically important when interpreting Deuterium Balmer emission.

2.2 Atomic process modelling

The emission of different spectral lines corresponding to atomic transitions can help determine the varying plasma properties in the divertor with the help of emission models. Relaxation from higher energy levels to lower energy levels with emission of photon energy equal to the difference in energy levels[72] is a key diagnostic of the divertor due to the predicted temperature and density dependence of the different transitions.

For higher density plasmas than corona models, collisional radiative models are suited to calculate rate coefficients for different atomic processes dependent on temperature and density. A commonly used model ADAS[73], is based on a generalised collisional radiative model. Collisions between atoms and electrons and radiation are given as couplings for each transition $i \rightarrow j$ along with ionisation and recombination factors taken into account. Population level balances are made using rate equations to calculate rates of individual transitions stored for each transition or atomic process as photon emission coefficients (PECs). PECs can be used to construct the total emission based on the population of different states, with different charges $Z+$. The total generalised formula from ADAS is shown in equation 4 without metastable states. In this case the charge exchange for any atom is written as colliding with a hydrogenic atom with neutral density n_0.

$$\epsilon_{i\to j} = PEC^{exc}_{i\to j} n_e n^{Z+} + PEC^{rec}_{i\to j} n_e n^{(Z+1)+} + PEC^{CX}_{i\to j} n_o n^{(Z+1)+} \tag{4}$$

For hydrogenic atoms this is simplified significantly as there is only 1 charge state other than neutral, which means the neutral density $n_0 = n^{(Z+1)+}$ in this case. The charge exchange term will not contribute to emission in the case of hydrogen-hydrogen collisions don't produce enough energy for a photon to be produced in this case, but is still important for transferring momentum and energy in the plasma. Assuming electron and ion density are equal then this simplifies to $n^{Z+} = n_{ion} = n_e$ to equation 5.

$$\epsilon_{i\to j} = PEC^{exc}_{i\to j} n_e^2 + PEC^{rec}_{i\to j} n_e n_0 \tag{5}$$

The total rates for some key atomic processes are plotted in figure 6. This is plotted in a log-log format due to the need to see the rate changes at low temperatures. As the temperature is lowered, the probability that enough energy is available for ionisation is reduced, which causes the ionisation rate to reduce sharply when lowering the temperature. The recombination rate changes by orders of magnitude as temperatures are lowered from 1eV to 0.1eV, where 0.1eV is the limit of the ADAS database entry plotted here.

In this thesis and the literature, impurity line emission is given by the charge state of the impurity and the transition wavelength. A Roman numeral gives the charge state of the impurity; for example, an impurity with a neutral charge would be shown as I, whereas once ionised (1+) would be II. The photon's wavelength in the atomic transition is then given afterwards[74].

2.3 The Sheath

Particles at the plasma edge will interact with a surface to form an equilibrium balance of ions and electrons. If the surface is not grounded, a floating potential is reached that causes a balance in charge flow in a region called the sheath. Instead of ions and electrons flowing unimpeded to the wall, a sheath region is formed, reducing the electron flow and enhancing ion flow.

The sheath is formed for a floating potential on the wall because electrons have higher mobility than

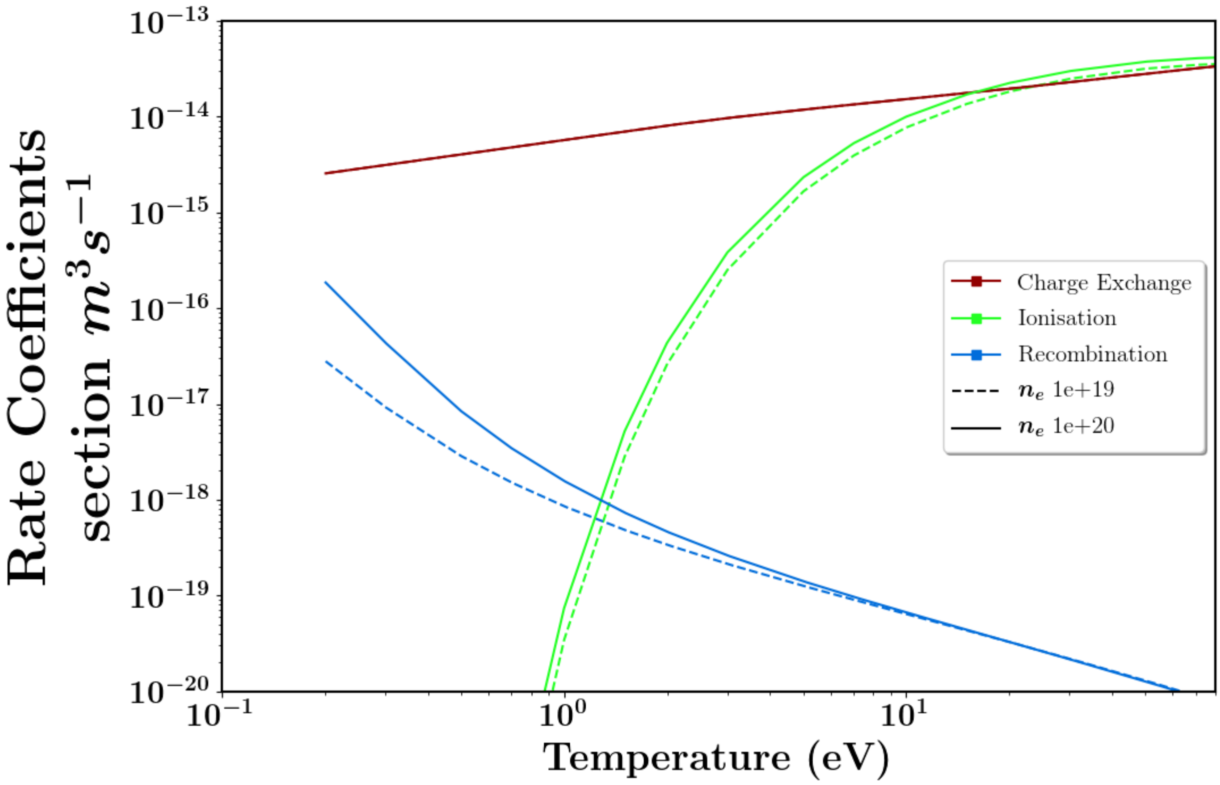

Figure 6: The total rate coefficients plotted from ADAS[73] for main divertor processes as a function of temperature.

ions so an initial greater electron flux would build a negative charge on the wall. The higher flux of electrons would mean that a current flows towards the wall, which would violate the quasi-neutrality condition of the plasma. Instead, the flux is balanced when the potential from electrons at the wall builds up, and the ions are now accelerated towards the wall while electrons from the plasma are decelerated.

The plasma forms a sheath by debye shielding. The debye shielding screens the charge by building a barrier of positive space charge in front of the wall, increasing ion density to compensate for the lower speed. The ions must move into the sheath with a large enough velocity to overcome the charge in the sheath and maintain the already built-up charge. They are required to move at greater than the sound speed c_s. This condition is known as the Bohm sheath criterion shown in equation 6 with ion mass m_i and equal ion and electron temperature.[75]

$$v_0 \geq c_s = (\frac{2k_B T_e}{m_i})^{\frac{1}{2}} \tag{6}$$

The pre-sheath region between the plasma and sheath has a local electric field and accelerates ions through the sheath region. Changes in the charge balance near the sheath will change the electron and ion densities by restoring a new charge balance. For example, if there is an increase in negative charge in the sheath, ions from further away are accelerated by the potential from the wall that is now less well screened.

$$c_{st} = \left(\frac{2k_B T_t}{m_i}\right)^{1/2} \tag{7}$$

The sound speed at the target is c_{st} as shown in equation 7. The Mach number at the target M_t must be equal to or greater than 1 to maintain the Bohm sheath criterion in equation 6.

The amount of parallel heat flux reaching the target $q_{||t}$ is calculated from equation 8 where the sheath transmission coefficient γ is the ratio of the power to the particle flux, predicted to be $\sim 7-8$[76] with target density and temperature n_t and T_t respectively.

$$q_{||t} = \gamma M_t n_t k_B T_t c_{st} \tag{8}$$

2.4 Target processes

Eventually ions collide with the target where a few different processes occur, including the ion sink of surface recombination. The ions striking a solid insulated surface combine with electrons to form neutrals. The neutrals are adsorbed or reflected by the change in momentum back into the divertor where they eventually reach temperatures where they are re-ionised, or pumped out.

The processes that ions can interact with the wall include adsorption, implantation, desorption, evaporation and sputtering.[77] Material can be deposited on the vessel walls, then released upon impact called desorption. If the heat load from the plasma evaporates material off the surface it is called evaporation.

Upon impacting the divertor target, ions can give enough energy to the material surface to eject atoms from the surface in a process called physical sputtering.[78] The ion energy must exceed the binding energy of the material to break the material bonds and give energy to the sputtered atom.

Hydrogenic ion interactions on carbon wall machines cause weakening of the surface or release as hydrocarbons, which is an additional source of erosion called chemical sputtering[77]. When molecules are sputtered off the surface they will increase the impurity concentration in the divertor which can reach the core plasma too. High atomic number atoms would cause more core radiation, but also be less likely to be sputtered. Reducing the target temperature T_t and particle flux is key to reducing the amount of physical sputtering.[79]

2.5 Divertor regimes

The divertor and SOL operation can be categorised into "regimes" to classify wide ranges of temperature and density of different species, which can simplify or complicate combinations of conditions that could be present. Different regimes have distinct dominant underlying physical mechanisms, which are associated with assumptions used in modelling.[80]

2.5.1 Sheath-limited regime

In the sheath-limited regime, the plasma has no significant sources or sinks except the source from cross-field transport from the core plasma and sink at the target, with almost no temperature reduction along flux tubes. The temperature along the flux tube can be isothermal if there is either a weak temperature gradient in the SOL or a low enough frequency of particle collisions (low collisionality, at lower density) that heat transport from movement of particles in the SOL (convection) parallel to the magnetic field rather is greater than heat transport from particle collisions (conduction). The low temperature reduction means it is only important to consider the boundary conditions entering the plasma and leaving into the sheath, which is why it is called the sheath-limited regime. Many of the processes in section 2.1 such as volume recombination, ionisation and neutral interactions, will not be significant in this regime. Heat can be transferred along the flux tube either by convection or conduction, but for convection, parallel heat fluxes are shown in equation 9 for equal ion and electron thermal energy $\frac{5}{2}k_BT$ with ion mass m_i and parallel particle flux $\Gamma_{||}$.

$$q_{||} = (5k_BT + \frac{1}{2}m_iv_{||}^2)\Gamma_{||} \tag{9}$$

2.5.2 Conduction-limited regime

In plasma conditions with a temperature gradient or high collisionality, heat transfer along the scrape-off layer can be dominated by conductive transport rather than convective transport. The collisionality can be raised by increased electron density and a drop in temperature compared to sheath-limited regimes, increasing the parallel heat transfer in the SOL. The temperature will drop from the upstream to the target, so it does have the advantage of low target temperature T_t, which helps reduce sputtering and heat flux. When parallel heat conduction is the primary energy transfer mechanism, the heat flux is shown in equation 10. κ_{0e} is the electron heat conduction coefficient, much larger than the ion heat conduction coefficient. The majority of heat is therefore transferred through electron conduction with strong temperature dependence.

$$q_{||} = -\kappa_{0e} T_e^{5/2} \frac{dT_e}{dx} \tag{10}$$

Pressure conservation and ionisation along the SOL determine the drop in temperature and density increase along a flux tube. The conservation of total pressure, the sum of dynamic (ram) and static pressure, means that any drop in p_{static} along the leg will increase $p_{dynamic}$, so raising the velocity and momentum (which the latter is assumed conserved in this regime). Pressure conservation is shown in equation 11 and can be used to simplify models by connecting plasma conditions at different positions along field lines.

$$\begin{aligned} p_{tot} &= p_{static} + p_{dynamic} \\ &= nk_BT_i + nk_BT_e + nmv^2 \end{aligned} \tag{11}$$

Another assumption is that neutrals created through surface recombination are re-ionised close to the target. This is why the conduction-limited regime is also known as a high recycling regime as recombination remove ions at the target only for them to be re-ionised again[76;80]. This has the effect of increasing heat and ion fluxes between the position where ionisation occurs (the ionisation front) and the target.

The radiative regime or the strongly radiating regime overlaps with the conduction-limited regime. However, it adds more radiation near the target, as the divertor temperature falls low enough, but these losses need to be considered in models. Seeded impurities help reduce the T_t and can reduce the target temperature to $\sim 5eV$[81] depending on the seeded impurity. In some scenarios, the radiating region can form close to the target and not spread the energy very effectively to reduce target power loads.

2.5.3 Detached regime

By increasing upstream density n_u, the impurity concentration f_z, or decreasing P_{SOL}, a detached regime can be reached, which further reduces the target heat flux and target temperature with additional atomic and molecular processes at temperatures less than 5eV[82]. The pressure along field lines is not conserved as target pressure and particle flux drops when there are significant momentum losses in the plasma but has to be combined with power loss to reduce the heat flux and be considered detached.

From the key processes reviewed, the overall behaviour in detachment is an expansion of the conduction-limited regime where the ion source has moved away from the target and/or reduced to allow processes that enable pressure, momentum, temperature and target ion flux to drop. On a flux tube from the outboard midplane to the target in order is described below in a potential detached divertor regime.

- Power enters the SOL at high temperatures between the midplane and the X-point shown in figure 5(b). Some very basic models approximate this as all particles entering at the midplane in figure 5(b). Models in section 2.6 emphasize how upstream quantities such as the upstream density can be considered important boundary conditions to the rest of the SOL and divertor.

- In regions of higher temperatures close to the midplane high energy particles can lose energy from charge exchange with neutrals. In this region heat is often transported by conduction because higher upstream densities favour detached conditions. Conduction reduces the temperature from the midplane down towards the X-point and target, and follows many of the conditions valid in the conduction limited regime.

- At some point up the divertor leg neutrals from the divertor are ionised[83]. The ionisation requires energy to be high enough to occur, and reduces the energy in the divertor while increasing the ion flux. Ion fluxes have to be dissipated after the ionisation source to be considered detached, even though reducing momentum is still important[84].

- The temperature reduction along a field line shown as a cartoon in figure 7a allows certain impurity emission lines shown in yellow in figure 7b to emit before reducing emission at lower temperatures further down field lines. Confinement of impurities to the divertor region is important to keep separate them from the core and to keep high enough divertor concentrations to radiate more power in the divertor region[46;85;48]. The ratio of impurity concentrations in the core and divertor is known as impurity enrichment or impurity compression. Radiation balance models shown in section 2.6 show that radiation being used as a dominant energy sink shifts the temperature profile along the SOL.

- For hydrogenic atomic transitions, recombination rates increase at lower temperatures (see figure 6), which can remove ions and electrons from the plasma and can be observed through emission. The recombination region is an ion sink considered in ion balance that is set up in the divertor. After recombination events, neutrals are not bound to the magnetic field and are transported throughout the divertor and can be pumped away. Some neutrals are re-ionised in

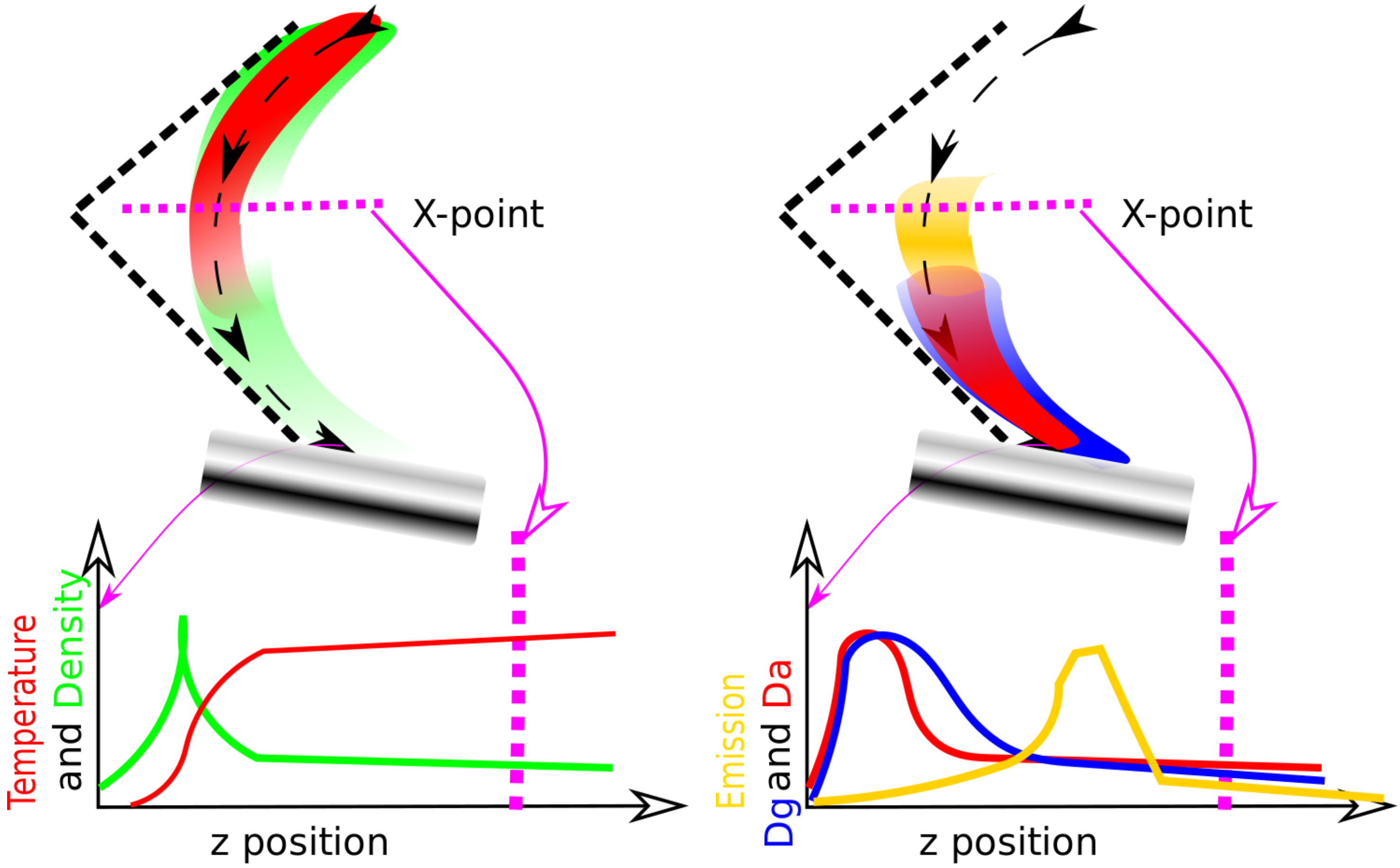

(a) (b)

Figure 7: Cartoon of the Density, temperature, radiation and individual D_γ and D_α emission.

the ionisation region, and some are transported around the divertor, which inevitably reduces particle fluxes. Ion-neutral interactions will be important in this region to produce drops to momentum[80], which are predicted from 2D simulations[86;87]. Target ion flux drops through either recombination and ion source reduction[88;89]. The majority of ion-neutral interactions have to be modelled more completely by larger simulations in order to be included.

- Near the sheath, ions are accelerated as described in section 2.3. The sheath will limit the ion fluxes to the target by accelerating ions into it. Target-based particle interactions such as sputtering are sources of neutrals and impurities at the walls.

The total length of the outer leg of the divertor can be increased to give more opportunity for plasma to interact on its way to the strike point along with moving the target to a lower magnetic field region that spreads flux tubes over a larger target wetted area[28]. This effect will be explored in the upcoming tokamak MAST-U. Analytical investigations are possible using the DLS model introduced in section 2.6.3.

From the previously mentioned divertor regimes, models and simulations attempt to reconstruct the SOL and divertor under different conditions. 2D simulations[86] [24] have been used to model many of the more important processes in the divertor and analytical models[90] help to simplify this understanding to show how to optimise the divertor.

2.6 Models

Having a high level of complexity to evaluate the divertor state means that simulations take into account as much physics and realistic geometry as possible. Divertor solvers such as SOLPS[91;82;87;28;92], EDGE2D[71], or Soledge2D[93] are widely used to replicate and understand experimental scenarios to explain divertor changes and make predictions for future experiments. Modelling neutral interactions to investigate detachment in low temperature conditions adds many interactions at the cost of the increased complexity of the system. Analytic models can make predictions much faster with simplified geometry and atomic physics. The scaling of different parameters can be shown without running many time consuming simulations at the cost of representing the problem more simply.

This section will discuss basic analytic models for detachment as well as the Lipschultz et al. [2016] model that is used for model comparison in this thesis.

To model the divertor analytically, the geometry of the flux tube is described as the SOL length and flux expansion from an upstream point to the target. The flux tube sources and sinks of particles and energy are defined along with boundary conditions then simplified to contain variables that can be found and estimated experimentally.

2.6.1 Basic Two point model

The basic two-point model starts off with simplified assumptions about the flux tube starting by unravelling the flux tube to a straight geometry, ignoring magnetic field changes as shown in figure 5. The top of the geometry is the “Upstream” (subscript u) part and the bottom is the target (subscript t). The two point model focuses on modelling at the upstream and target points, although positions in between may be modelled too. It is assumed that the recycling region extends only a short distance from the target when balancing particle fluxes in the model, so particle conservation equations are not required and requires pressure balance to link the upstream and target points together. The basic two point model is not generally expected to agree quantitatively with divertor conditions. However the proportionality with certain variables may match very specific attached conditions where no heat flux is lost and pressure is conserved. The two point model is introduced in this thesis for the purpose of contrasting how different upstream quantities scale the target temperature, target ion flux, or target heat flux.

Starting from equation 11 balancing pressure at both upstream and target gives equation 12 where ion and electron temperatures are assumed equal and there is no upstream ion velocity and momentum of electrons is neglected. The velocity that ions enter the sheath are required to be equal to the sound speed due to the Bohm criterion, so equation 7 is substituted in to equation 12. This shows that although total pressure is conserved under these assumptions, the static pressure is reduced at the target as it has been transferred to dynamic pressure.

$$\begin{aligned}2n_u k_B T_u &= 2n_t k_B T_t + n_t m v_t^2 \\ 2n_u k_B T_u &= 2n_t k_B T_t + n_t m\left(\frac{2k_B T_t}{m_i}\right) \\ n_u T_u &= 2n_t T_t\end{aligned} \tag{12}$$

Equation 12 is valid in sheath and conduction limited regimes. Assuming the SOL is considered conduction limited, equation 10 can be integrated over the SOL length along a field line (L_{para}) between upstream and target to give equation 13, assuming that there are no sources or sinks of parallel heat flux that would mean $q_{||}$ is constant along the SOL.

$$\begin{aligned}\int_{x=0}^{x=L_{para}} q_{||}dx &= -\kappa_{0e}\int_{T_t}^{T_u} T_e^{5/2}dT_e \\ q_{||}L_{para} &= -2/7\kappa_{0e}(T_u^{7/2}-T_t^{7/2}) \\ T_u^{7/2} &= T_t^{7/2} + \frac{7}{2}q_{||}\frac{L_{para}}{\kappa_{0e}}\end{aligned} \tag{13}$$

Under these conditions, equations 7, 8, 12 and 13 can't be reduced to a single variable as function of one other variable using this number of equations and unknowns. The upstream density and upstream parallel heat flux would affect the target temperature.

To evaluate T_t dependence on upstream variables, the approximation that $T_t^{7/2} << T_u^{7/2}$is invoked, which means T_t can be ignored in equation 13 this term to give an approximate of T_u. This can then be rearranged along with equation 8, 7 and 12 to give equation 14 to show the target temperature dependence on upstream variables. It shows approximately that $T_t \propto \frac{T_u^5}{L_{para}^2 n_u^2}$, upstream temperature increases and drops with increases of upstream density.

$$T_t \sim T_u^5 \frac{8}{49} \frac{1}{(\gamma M_t n_u)^2} \frac{m_i}{k_B^3} \left(\frac{\kappa_{0e}}{L_{para}} \right)^2 \tag{14}$$

Additionally it is important to also look at the dependence of particle flux and heat flux on the target temperature. Parallel heat flux dependence is simply from equation 13 rearranged and assuming $T_u >> T_t$ then $q_{||} \sim T_u^{7/2} \frac{\sqrt{2}}{7} \left(\frac{\kappa_{0e}}{L_{para}} \right)$. The heat flux is therefore simply predicted to be a function of upstream temperature.

The particle flux dependence is worked out using $\Gamma_t = n_t M_t c_{st}$. By similarly eliminating all determined quantities ($q_{||}$ and T_t) the particle flux is $\Gamma_t \propto \frac{n_u^2 L_{para}}{T_u^{3/2}}$, strongly increasing due to upstream density, and decreasing from increasing upstream temperature.

$$\Gamma_t \sim \frac{7n_u^2}{4T_u^{3/2}} \gamma M_t^2 \left(\frac{k_B^2}{m_i} \right) \left(\frac{L_{para}}{\kappa_{0e}} \right) \tag{15}$$

These equations show that overall for increasing upstream density in tokamaks, the target flux will increase but target temperature decreases, but the heat flux won't change as it was enforced as a constant in equation 13. For increasing upstream temperature the target temperature will decrease, the heat flux will increase and the target flux will reduce. This does not model a detached regime which would predict a drop in heat flux, target temperature and target flux. At the onset of detachment and increasing upstream density, the ion flux will stop increasing, level off and decrease instead. The point that this occurs is called the "rollover" of the ion flux. Additional loss terms for pressure and heat flux are needed to describe detached conditions.

2.6.2 Lengyel Formulation

The Lengyel formulation introduces an analytic form of impurity radiation loss. Local changes to the energy in a flux tube volume per second (H) are used to define the heat flux changes over a length dx as shown in equation 16. It is assumed that there is no ionisation in the SOL so that the sources from the upstream can be balanced with radiation losses. P_{SOL} can be assumed to enter at the upstream point or over the length of the SOL as shown in figure 5. The total energy change is $\frac{1}{A}\frac{dP_{SOL}}{dx}$ where A is the area of the flux tube. The radiation term used is $n_e n_z Q(T) = n_e^2 f_z Q(T)$, where the impurity concentration is defined as $f_z = \frac{n_z}{n_e}$, n_z is the density of the impurity species and $Q(T)$ is the radiation loss "cooling curve" function. To simplify, the impurity concentration and electron density should be constant over the emission region.

$$\frac{dq_{||}}{dx} = H = S - n_e n_z Q(T) \tag{16}$$

For no energy source term after the upstream point $S = 0$ and multiplying both sides of equation 16 and integrating gives equation 17. The substitution of $\frac{dT}{dx}$ from the conduction equation 10 is used assuming heat conduction is dominant.

$$\begin{aligned}
\int_{q_{||t}}^{q_{||u}} dq_{||}\frac{dT}{dx} &= -\int_{T_t}^{T_u} n_e n_z Q(T)dT \\
\int_{q_{||t}}^{q_{||u}} (\frac{-q_{||}}{\kappa_{0e}T_e^{5/2}})dq_{||} &= -\int_{T_t}^{T_u} n_e n_z Q(T)dT \\
\int_{q_{||t}}^{q_{||u}} q_{||}dq_{||} &= \int_{T_t}^{T_u} (\kappa_{0e}T_e^{5/2})n_e n_z Q(T)dT \\
\\
\frac{(q_{||u}^2 - q_{||t}^2)}{2} &= \int_{T_t}^{T_u} (\kappa_{0e}T_e^{5/2})n_e n_z Q(T)dT \\
q_{||t} &= \left(q_{||u}^2 - \int_{T_t}^{T_u} (\kappa_{0e}T_e^{5/2})n_e n_z Q(T)dT\right)^{1/2}
\end{aligned} \tag{17}$$

Equation 17 shows how the heat flux falls from the upstream value with increased radiation and density. The cooling curve function has to be an integrable function that doesn't diverge at high or low temperatures. By making substitutions to equation 17 the particle flux, heat flux and target temperature can be compared.

Enforcing the sheath condition in equation 8 and pressure balance from equation 12, then rearranging gives an estimate for the target temperature. The target temperature, therefore, depends on upstream density and temperature with the loss in heat flux from radiation as an offset, as shown in equation 18.

$$\begin{aligned}
\gamma M_t n_t k_B T_t c_{st} &= \left(q_{||u}^2 - \int_{T_t}^{T_u} (\kappa_{0e}T_e^{5/2})n_e n_z Q(T)dT\right)^{1/2} \\
T_t &= \left(\frac{\sqrt{2}m_i}{\gamma M_t k_B^{3/2} n_u T_u}\right)^2 \left(q_{||u}^2 - \int_{T_t}^{T_u} (\kappa_{0e}T_e^{5/2})n_e n_z Q(T)dT\right)
\end{aligned} \tag{18}$$

For particle flux the first section of equation 18 has been substituted into $\Gamma_t = n_t \gamma M_t c_{st}$ and T_t from equation 18 to determine equation 19. No ionisation sources or recombination sinks of particles are assumed. This is the similar to the basic 2 point model dependence on n_u if the first term in equation 19 with n_u^2 is dominant, but as much larger fractions heat flux are radiated, the density dependence of the radiation term would have the opposite effect.

$$\begin{aligned}\gamma M_t n_t k_B T_t c_{st} &= \left(q_{||u}^2 - \int_{T_t}^{T_u} (\kappa_{0e} T_e^{5/2}) n_e n_z Q(T) dT \right)^{1/2} \\ \gamma k_B T_t \Gamma_t &= \left(q_{||u}^2 - \int_{T_t}^{T_u} (\kappa_{0e} T_e^{5/2}) n_e n_z Q(T) dT \right)^{1/2} \\ \Gamma_t &= \left(\frac{\gamma^{1/2} M_t k_B^{1/2} n_u T_u}{\sqrt{2} m_i} \right)^2 \left(q_{||u}^2 - \int_{T_t}^{T_u} (\kappa_{0e} T_e^{5/2}) n_e n_z Q(T) dT \right)^{-1/2}\end{aligned} \tag{19}$$

2.6.3 DLS Model

The model from Lipschultz et al. [2016] is an extension of the Lengyel formulation. Geometry is set up by considering the magnetic field and geometry for source term differently, as described in this section. The length and position of the radiation zone are also considered differently, with the position defining the edge of the detachment front. Other approximations at the front position allow it to be viewed as a "virtual" target compared to other models that can be located between the target and X-point. Explicit dependencies in this model allow exploration into total flux expansion effects caused by changes in magnetic field strength along a flux tube, the length of the divertor leg along field lines and control parameter dependence.

The source energy term S enters the geometry above the X-point from the midplane, which is assumed to enter evenly in this space as shown in figure 5(b). The total length of the radiation zone is assumed to be small compared with the length of the flux tube and whether the radiation begins above or below the X-point sets up the problem slightly differently. In this section, we assume that the radiating region is below the X-point. It is assumed that the midplane to X-point region is the only source of energy and particles and that there is no ionisation source in this region. Balancing net energy $H = S - E$ along the scrape-off layer introduces the magnetic field through a flux surface of a magnetic flux tube. The heat flux in vector form is shown in equation 20 and in energy balance at equilibrium where $\frac{dq}{dt} = 0$ in equation 21.

$$\overrightarrow{q} = -\overrightarrow{\kappa}.\overrightarrow{\nabla} T \tag{20}$$

$$\begin{aligned}\overrightarrow{\nabla}.\overrightarrow{q} &= H \\ \overrightarrow{\nabla}.(\overrightarrow{\kappa}.\overrightarrow{\nabla}T) &= -H\end{aligned} \tag{21}$$

By converting to parallel coordinates $(\frac{\mathbf{B_p}}{B})\nabla_{||} = \nabla = B\frac{d}{dl}$ and using the parallel spitzer heat conductivity $\overrightarrow{\kappa} = \frac{\overrightarrow{B}}{B}\frac{\overrightarrow{B}}{B}\kappa_{||}$ is a square matrix from the outer product of magnetic field as a matrix parallel to the magnetic field $\overrightarrow{\kappa} = \kappa_{||}\frac{(B_{||},0)}{B} \otimes \frac{(B_{||},0)}{B}$, which is that $\overrightarrow{B}$ is parallel to the field.

$$\begin{aligned}\overrightarrow{\nabla}.(\frac{\overrightarrow{B}}{B} \otimes \frac{\overrightarrow{B}}{B}\kappa_{||}.\overrightarrow{\nabla}T) &= -H \\ \overrightarrow{\nabla}.(\frac{\overrightarrow{B}}{B}\frac{\overrightarrow{B}^T}{B}\kappa_{||}.\overrightarrow{\nabla}T) &= -H\end{aligned} \tag{22}$$

Given that $\overrightarrow{\nabla}.(\overrightarrow{B}g) = \overrightarrow{B}\overrightarrow{\nabla}g$ (where in this case $g = \frac{\overrightarrow{B}^T}{B}\kappa_{||}.\overrightarrow{\nabla}T$ is a scalar), one factor of $\overrightarrow{B}$ can be taken out of the bracket then taking the direction parallel to the field gives equation 23 by using $\overrightarrow{\nabla} = \frac{d}{dl}$ and $\overrightarrow{B} = B$

$$\begin{aligned}\overrightarrow{B}\overrightarrow{\nabla}.(\frac{\overrightarrow{B}^T}{B^2}\kappa_{||}.\overrightarrow{\nabla}T) &= -H \\ -H &= B\frac{d}{dl}(\frac{\kappa_{||}}{B}\frac{dT}{dl})\end{aligned} \tag{23}$$

A different measure of the detachment front position is introduced by using a normalised volume along the flux tube. Each segment of volume dV has a length component dl along B, and an area component perpendicular to B, inversely proportional to the local magnetic field strength. To convert dl to dz, this component has to be normalised to a reference area. Here we choose a value along the flux tube close to the X-point with total magnetic field $B_\times$. To convert between dz and the poloidal distance l_p using the local poloidal magnetic field B_p shown in equation 24.

$$dz = \frac{B_\times}{(B)_1}dl = \frac{B_\times}{(B_{pol})_1}dl_p \tag{24}$$

The equivalent of equation 16 is shown in equation 25 by redefining $q_s = q\frac{B_\times}{B}$

$$\frac{dq_s}{dz} = H = S - n_e n_z Q(T) \tag{25}$$

Substituting dl from equation 24 into the scalar version of equation 20 and multiplying both sides by $\frac{B_\times}{B}$ gives equation 26. This is expanded by changing $\kappa_{||} = \kappa_1 \frac{B_\times^2}{B^2} T^{5/2}$ as the Spitzer conductivity and additional normalisation of κ is included.

$$\begin{aligned} q_s = q_{||}\frac{B_\times}{B} &= -\kappa_{||}\frac{dT}{dl}\frac{B_\times}{B} \\ q_s &= -\kappa_1 T^{5/2}\frac{B_\times^2}{B^2}\frac{dT}{dz}(\frac{B}{B_\times})\frac{B_\times}{B} \\ q_s &= -\kappa_1 T^{5/2}\frac{B_\times^2}{B^2}\frac{dT}{dz} \end{aligned} \tag{26}$$

Multiplying equation 26 by equation 25 at a value of z below the X-point with no source term $S = 0$ results in equation 27. The result of cancelling z dependence and integrating between region of radiation from the cold side (c) to the hot side (h) of the front is also included in equation 27.

$$\begin{aligned} q_s\frac{dq_s}{dz} &= n_e^2 f_z Q(T)\kappa_1 T^{5/2}\frac{B_\times^2}{B^2}\frac{dT}{dz} \\ q_s dq_s &= n_e^2 f_z Q(T)\kappa_1 T^{5/2}\frac{B_\times^2}{B^2}dT \\ \int_{q_c}^{q_h} q_s dq_s &= -\int_{T_c}^{T_h} n_e^2 f_z Q(T)\kappa_1 T^{5/2}\frac{B_\times^2}{B^2}dT \end{aligned} \tag{27}$$

Assuming that the front is small, the impurity concentration and pressure can be approximated as constant across the length. This means that these quantities can be taken out of the integral and using $p = n_e T_e = n_u T_u = n_h T_h$ and is constant between the cold end of the front to the upstream point to get equation 28. The model then simplifies with $q_c \sim 0$.

$$\begin{aligned} \frac{q_h^2 - q_c^2}{2} &= -p^2 f_z \kappa_1 \frac{B_\times^2}{B^2}\int_{T_c}^{T_h} Q(T)T^{1/2}dT \\ q_h &= -p\frac{B_\times}{B}\sqrt{2 f_z \kappa_1}\sqrt{\int_{T_c}^{T_h} Q(T)T^{1/2}dT} \\ q_h &= -n_u T_u\frac{B_\times}{B}\sqrt{2 f_z \kappa_1}\sqrt{\int_{T_c}^{T_h} Q(T)T^{1/2}dT} \end{aligned} \tag{28}$$

The upstream temperature can be worked out by substituting equation 26 into equation 25 for the region between the hot end ($z = z_h$) of the front to the midplane ($z = L$) where there is no radiation in this region so $H = S$. Equation 29 sets up the integral between a point z'.

$$\begin{gathered}
\frac{d(-\kappa_1 T^{5/2} \frac{B_\times^2}{B^2} \frac{dT}{dz})}{dz} = -S \\
\int d(\kappa_1 T^{5/2} \frac{B_\times^2}{B^2} \frac{dT}{dz}) = \int_{z'}^{L} S dz \\
\kappa_1 T^{5/2} \frac{B_\times^2}{B^2} \frac{dT}{dz} = \int_{z'}^{L} S dz
\end{gathered} \tag{29}$$

The source term is segmented so that S evenly entering the SOL between $z_\times$ and L and has no additional contribution below the X-point. This segmentation requires all further functions of z to be segmented, first applied to the integral in equation 29. Above the X-point $S = S_0$ and below $S = 0$.

$$\begin{gathered}
z' < z_\times \\
\int_{z'}^{L} S dz = \int_{z'}^{z_\times} (0) dz + S_0 \int_{z_\times}^{L} dz = 0 + S_0(L - z_\times) \\
z' > z_\times \\
\int_{z'}^{L} S dz = S_0 \int_{z'}^{L} dz = S_0(L - z')
\end{gathered} \tag{30}$$

The source term integral in equation 29 is also equal to the heat flux entering from upstream (q_i) between L and $z_\times$. This is then integrated a second time in equation 31 to get T_u, where in the final step the distance between the hot end of the front and the midplane is large enough that there is a significant temperature drop to assume $T_u^{7/2} >> T_h^{7/2}$ just from the conduction equation to ignore $T_h^{7/2}$.

$$
\begin{aligned}
\kappa_1 T^{5/2}\frac{B_\times^2}{B^2}dT &= (S_0(L-z_\times)|_{z_h}^{z_\times} + S_0(L-z')|_{z_\times}^{L})dz' \\
\int_{T_h}^{T_u} T^{5/2}dT &= \frac{S_0}{\kappa_1}\left[(L-z_\times)\int_{z_h}^{z_\times}\frac{B^2}{B_\times^2}dz' + \int_{z_\times}^{L}\frac{B^2}{B_\times^2}(L-z')dz'\right] \\
\frac{2}{7}(T_u^{7/2}-T_h^{7/2}) &= -\frac{S_0}{\kappa_1}\left[(L-z_\times)\int_{z_h}^{z_\times}\frac{B^2}{B_\times^2}dz' + \int_{z_\times}^{L}\frac{B^2}{B_\times^2}(L-z')dz'\right] \\
T_u &\sim \left[\frac{7S_0}{2\kappa_1}\left[(L-z_\times)\int_{z_h}^{z_\times}\frac{B^2}{B_\times^2}dz' + \int_{z_\times}^{L}\frac{B^2}{B_\times^2}(L-z')dz'\right]\right]^{2/7}
\end{aligned}
\tag{31}
$$

The magnetic field can be described in different ways. In Lipschultz et al. [2016] the total magnetic field is approximated as linearly increasing between the target B_t and the Xpoint $B_\times$, then constant $B_\times$ above the X-point. This is described at point h as $B_h = B_t + (B_\times - B_t)\frac{z_h}{z_\times}$ with gradient $\frac{dB_h}{dz} = \frac{(B_\times - B_t)}{z_\times}$

This splits the integral into 2 separate regions between the hot end of the front and the X-point, and the X-point to the midplane. The derivation of T_u is found in appendix section A and shown in equation 32.

$$
T_u \sim \left[\frac{7S_0(L-z_\times)}{2\kappa_1}\left[\frac{(z_\times - z_h)}{3}[1+\frac{B_h}{B_\times}+\frac{B_h^2}{B_\times^2}] + \frac{(L-z_\times)}{2}\right]\right]^{2/7}
\tag{32}
$$

Substituting back into equation 28 gives equation where $U = \left[\frac{7}{2\kappa_1}\right]^{2/7}\sqrt{2\kappa_1}\sqrt{\int_{T_c}^{T_h} Q(T)T^{1/2}dT}$

$$
\begin{aligned}
q_h &= n_u\left[\frac{7S_0(L-z_\times)}{2\kappa_1}\left[\frac{(z_\times - z_h)}{3}[1+\frac{B_h}{B_\times}+\frac{B_h^2}{B_\times^2}] + \frac{(L-z_\times)}{2}\right]\right]^{2/7}\frac{B_\times}{B_h}\sqrt{2f_z\kappa_1}\sqrt{\int_{T_c}^{T_h} Q(T)T^{1/2}dT} \\
q_h &= -Un_u\sqrt{f_z}\frac{B_\times}{B_h}\left[S_0(L-z_\times)\left[\frac{(z_\times - z_h)}{3}[1+\frac{B_h}{B_\times}+\frac{B_h^2}{B_\times^2}] + \frac{(L-z_\times)}{2}\right]\right]^{2/7}
\end{aligned}
\tag{33}
$$

The heat flux balance assumes that the heat flux input $-S_0(L-z_\times) = q_i$ balances with the heat flux dissipated in the front $q_f = q_h - q_c$ where $q_f \sim q_h$ assuming all heat flux is dissipated in the thermal front giving $-S_0(L - z_\times) = q_h$.

$$S_0(L - z_\times) = U n_u \sqrt{f_z} \frac{B_\times}{B_h} \left[S_0(L - z_\times) \left[\frac{(z_\times - z_h)}{3} [1 + \frac{B_h}{B_\times} + \frac{B_h^2}{B_\times^2}] + \frac{(L - z_\times)}{2} \right] \right]^{2/7} \tag{34}$$

The parallel heat flux upstream is assumed to follow a profile with a width λ_q and with a distance poloidally around the tokamak of $2\pi R$. The distance around the tokamak that intercepts the flux tube is scaled by the ratio of the poloidal to total magnetic field to give a total area $A = 2\pi R \lambda_q B_{pol}/B$ which the total power crossing the scrape-off layer P_{SOL} passes through so balancing the total energy gives the $S_0(L - z_\times) = P_{SOL}/2\pi R \lambda_q (B_{pol}/B)$. In this scenario, above the X-point the total magnetic field $B = B_\times$, so it is included in this term. This expands the list of assumed constant terms to $U_1 = [2\pi R \lambda_q B_{pol}/B_\times]^{5/7} U$.

$$\begin{aligned} \frac{P_{SOL}^{5/7}}{n_u \sqrt{f_z}} &= U_1 \frac{B_\times}{B_h} \left[\left[\frac{(z_\times - z_h)}{3} [1 + \frac{B_h}{B_\times} + \frac{B_h^2}{B_\times^2}] + \frac{(L - z_\times)}{2} \right] \right]^{2/7} \\ \frac{n_u \sqrt{f_z}}{P_{SOL}^{5/7}} &= U_1^{-1} \frac{B_h}{B_\times} \left[\left[\frac{(z_\times - z_h)}{3} [1 + \frac{B_h}{B_\times} + \frac{B_h^2}{B_\times^2}] + \frac{(L - z_\times)}{2} \right] \right]^{-2/7} \end{aligned} \tag{35}$$

2.6.4 DLS model normalisation

So far there are variables contained within U_1 of equation 35 that are not expected to change over a pulse while some parameters cannot be evaluated accurately enough for model evaluation, particularly with current diagnostic coverage. By evaluating equation 35 at a reference point, the left and right hand side of this equation are effectively normalised at this reference point. Any relative change in control parameter (P_{SOL}, n_u, f_z) on the left hand side of equation 35 would result in a change of z_h position on the right hand side. In Lipschultz et al. [2016] it makes sense to normalise to the X-point, since $B_h = B_\times$ and $z_h = z_\times$ simplify the right hand side of equation 35. Experimentally data are found for several pulses at different levels of detachment. For some of these there is no available data at the X-point as it did not fully detach, so it is not practical to use these.

Normalisation was initially changed to the target as detachment front position must begin at the target and this would also make some simplifications to the model. However one problem with this is that certain time regions of each pulse must be analysed separately to isolate changes in individual control parameters, and not all of these pass through the target. There is also some uncertainty in where the position of the target is located poloidally, from sources such as the equilibrium and estimating the poloidal strike point location on angled tiles on JET. This uncertainty is a problem because any change in control parameter with the front position around the target should result in a change in front position, but if the divertor is still attached then this movement won't happen. If the normalisation at the target is made before the front position responds to control parameters but within uncertainty (i.e. the divertor could still be attached), then an offset in a prediction is introduced.

To get around the problem of selecting a fixed normalisation point, normalisation is generalised at a point (1) to calculate a prediction at the second point (2). This is shown in equation 36 when equation 35 at point (2) is divided by left and right hand side of the same equation at point (1).

$$\frac{\left(\frac{n_u f_z^{1/2}}{P_{SOL}^{5/7}}\right)_2}{\left(\frac{n_u f_z^{1/2}}{P_{SOL}^{5/7}}\right)_1} = \frac{B_2}{B_1} \frac{\left[\frac{z_\times - z_2}{3}\left(1 + \left|\frac{B_2}{B_\times}\right| + \left|\frac{B_2}{B_\times}\right|^2\right) + \frac{L - z_\times}{2}\right]^{-2/7}}{\left[\frac{z_\times - z_1}{3}\left(1 + \left|\frac{B_1}{B_\times}\right| + \left|\frac{B_1}{B_\times}\right|^2\right) + \frac{L - z_\times}{2}\right]^{-2/7}} \tag{36}$$

When evaluating a change in front position, the contributions of all three control parameters are separately evaluated to be combined into a total derivative of front position as shown in equation 37.

$$dz_h = \frac{\partial z_h}{\partial P_{SOL}} dP_{SOL} + \frac{\partial z_h}{\partial n_u} dn_u + \frac{\partial z_h}{\partial f_z} df_z \tag{37}$$

Each partial derivative term in equation 37 is found by differentiating equation 35 with respect to each variable, keeping the other two variables constant. To do this, the equation is generalised as C^{X_c} where C is either n_u, f_z or P_{SOL} and X_c is the corresponding exponent. Here it is seen from replacing each variable in equation 35 with C^{X_c}, would mean X_c is 1, 1/2 and -5/7 for n_u, f_z or P_{SOL} respectively.

Appendix section B shows the full derivation of this generalised to variable C in a similar form as in Lipschultz et al. [2016].

$$\frac{\partial z_h}{\partial C} = \frac{X_c}{C}\left\{\frac{2}{7}\frac{B_h^2}{B_\times^2}\left[\frac{2(z_\times - z_h)}{3(L - z_\times)}\left(1 + \left|\frac{B_h}{B_\times}\right| + \left|\frac{B_h}{B_\times}\right|^2\right) + 1\right]^{-1} + \left(1 - \frac{B_t}{B_\times}\right)\frac{B_\times}{B_h}\frac{1}{z_\times}\right\}^{-1} \tag{38}$$

Equation 38 describes the particular importance of how the exponent X_c effects the sensitivity. At any front position z_h, we have $\frac{\partial z_h}{\partial C} \propto \frac{X_c}{C}$, which shows that the change in z_h position is proportional to the relative change in a control parameter $\frac{\partial C}{C}$, and has a strength change shown from X_c. The sensitivity $\frac{\partial z_h}{\partial C}$ would be larger for higher magnitude of X_c, which is highest for n_u, than P_{SOL} and lowest for f_z changes. The negative sign of X_c for P_{SOL} means the movement of the detachment front will oppose the increase or decrease in P_{SOL}.

In different discharges the field line length from the target to the X-point and midplane will differ, so we have further normalized the z position by $z_\times$ to create $\hat{z}$ in equation 39. This is necessary to compare properly between discharges or even if the magnetic geometry varies within a discharge.

$$\hat{z} = \frac{z_2}{z_\times} \tag{39}$$

2.6.5 DLS model with alternative magnetic field assumptions for JET

An assumption of linear increase in magnetic field from the target to the X-point is introduced in the previous section to keep the model analytic. Magnetic field structure varies on different devices and configurations, for example MAST-U will eventually run complex field structures that will violate this assumption with the use of super-X configurations. A simpler model in this case makes it much easier to explain dependences in this model. The two approximations in section 2.6.5.1 and 2.6.5.2 before being compared in section 2.6.5.3. This is done to make sure that the 3 variants of the model are not significantly different in analysed JET pulses and to make sure that the DLS magnetic field model characterisation is not important for evaluating the DLS model in this thesis.

On JET from the X-point to target there is only a small change in magnetic field and the length (in z position) in this region is quite small. JET can operate with a horizontal or vertical target, which the magnetic field can be described to a reasonable degree as a linear increase in either case. However since magnetic field strength is proportional to the major radius the horizontal target case has very little change in total magnetic field from target to X-point. This magnetic field change is small enough to approximate magnetic field as constant $B_h = B_\times = B_t$.

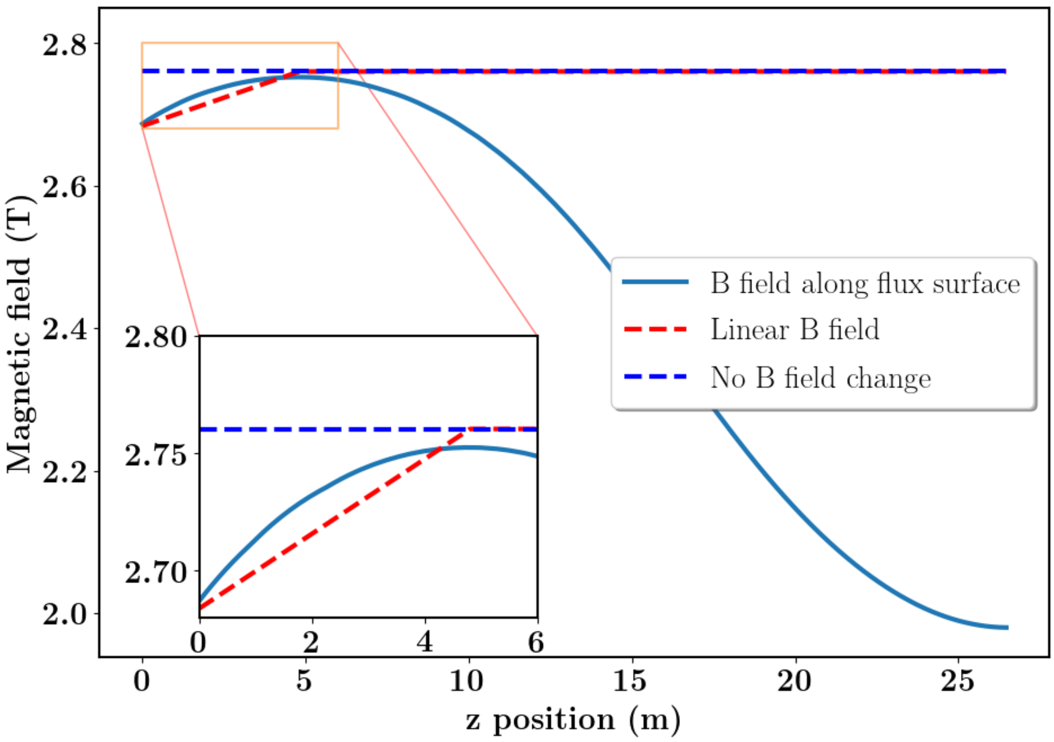

Figure 8: The total magnetic field on JET along a flux surface (solid light blue) with a linear magnetic field assumption (dashed red) and a constant magnetic field (dashed blue). These difference are compared to determine the importances of DLS model assumptions on the analysis in this thesis. The highlighted region between the X-point and the target is shown on the mini-figure region.

2.6.5.1 Generalising the magnetic field

For a general magnetic field structure, the equivalent of equation 36 is shown in equation 40, with derivation in Appendix section C.1. Terms are calculated separately above and below the X-point as before, but taking into account the magnetic field above the X-point changing as shown in figure 8 is a larger difference in the JET case. This constant term $\int_{z_\times}^{L} \frac{B^2(z)(L-z)}{L-z_\times} dz$ is very different in magnitude from the equivalent value of $B_\times^2\left[\frac{L(L-z_\times)}{L-z_\times} - \frac{(L^2-z_\times^2)}{2(L-z_\times)}\right] = B_\times^2\left[L - \frac{(L+z_\times)}{2}\right] = B_\times^2\left[\frac{(L-z_\times)}{2}\right]$, which is evaluated for $B(z) = B_\times$. For a large portion of the SOL above the X-point, the flux tube is at a greater radius R, which implies a lower magnetic field strength.

In this derivation P_{SOL} has a factor of $1/B$, so $\int_{z'}^{L} S dz = 2\pi P_{SOL} R \lambda_q B_{pol} \int_{z'}^{L} B(z)^{-1} dz$, which is cancelled in equation 40 since it is the same factor on the numerator and denominator of the LHS of equation 40.

$$\frac{\left(\frac{n_u f_z^{1/2}}{P_{SOL}^{5/7}}\right)_2}{\left(\frac{n_u f_z^{1/2}}{P_{SOL}^{5/7}}\right)_1} = \frac{B_2}{B_1} \frac{\left[\int_{z_2}^{z_\times} B^2(z)dz + \int_{z_\times}^{L} \frac{B^2(z)(L-z)}{L-z_\times} dz\right]^{-2/7}}{\left[\int_{z_1}^{z_\times} B^2(z)dz + \int_{z_\times}^{L} \frac{B^2(z)(L-z)}{L-z_\times} dz\right]^{-2/7}} \tag{40}$$

The sensitivity is shown in equation 41, still contains generalised exponent X_c factorised out, which is also derived in appendix section C.1.

$$C\frac{\partial z}{\partial C} = X_c \left[\frac{1}{B(z)}\frac{\partial B(z)}{\partial z} + \frac{2}{7}B^2(z)\left[\int_{z}^{z_\times} B^2(z)dz + \int_{z_\times}^{L} \frac{B^2(z)(L-z)}{L-z_\times}dz\right]^{-1}\right]^{-1} \tag{41}$$

2.6.5.2 Simplifying the magnetic field dependence

Another derivation of the DLS model is shown for no magnetic field in appendix section C.2, which has a magnetic field approximation as shown in figure 8. The main equations are shown in 42 and 43 for detachment front movement and sensitivity respectively. These show more clearly the movement of z position, including the strength of sensitivity for each control parameter by its exponent.

$$z_2 = \left[\frac{L+z_\times}{2}\right] - \left[\frac{L+z_\times}{2} - z_1\right]\left[\frac{\left(\frac{n_u f_z^{1/2}}{P_{SOL}^{5/7}}\right)_2}{\left(\frac{n_u f_z^{1/2}}{P_{SOL}^{5/7}}\right)_1}\right]^{-7/2} \tag{42}$$

$$\frac{\partial z_h}{\partial C} = \frac{7X_c}{2C}\left[\frac{L+z_\times}{2} - z_h\right] \tag{43}$$

The validity of these equation 42 and 43 only apply to JET and similar aspect ratio devices, but it is easier to see how the z position and sensitivity is affected by control parameter variation and to evaluate a z position from control parameters. Equation 42 shows that changing the control parameters affects the z position by moving it down from an upstream point with a change in control parameters. The equation is still only valid between the X-point and the target. The sensitivity in equation 43 is only dependent on control parameter exponents and the distance from the upstream, for a relative change in control parameter $\frac{\partial C}{C}$.

2.6.5.3 Comparing the DLS model approximations

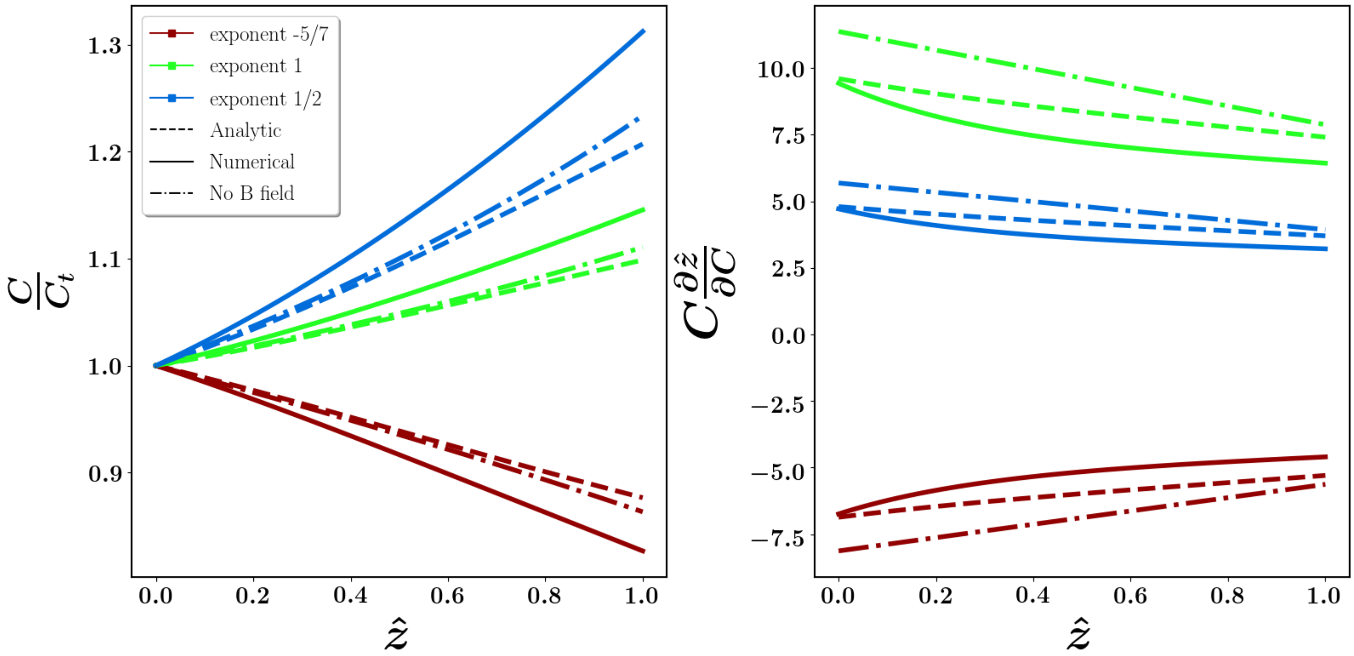

Figure 9: The model predictions for (a) The change in z position to a relative change in control parameter (b) the sensitivity at different z positions. The original model with linear B field assumption (Analytic), altered model with any magnetic field change (Numerical) and altered model with no change in magnetic field (No B field) are shown separately.

To find out how important the magnetic field is in the analysis, the DLS model and the 2 variants are plotted in figure 9. Slight differences in sensitivity between the different model variants are seen. There is a difference between all the models, which experience a larger difference in sensitivity further from the X-point. Overall the variation is not very large, which is to be expected as the magnetic field change is very low on JET so it turns out is not very important for the analysis in this thesis, but this more general model could be applied to cases where these assumptions are no longer valid, such as MAST-U super-X configurations. The data will therefore be compared with the original DLS model, with any arguments based on sensitivity scaling using the variant with no change in magnetic field for simplicity.

3 Camera data processing

In this chapter, the processing and analysis of filtered camera images to facilitate model comparison are described. The key data to measure the detachment state in this thesis are divertor filtered camera images, which require processing before comparing to models. Other diagnostics are used to estimate control parameters or to support and verify either the camera data front position or control parameters. Control parameter definitions are introduced separately in section 4.7. The use of the camera data for tracking the detachment front is introduced in chapter 4.

To track the detachment front, emission must be projected from 3D line-of-sight integrals within the JET camera view to the 2D poloidal plane under the assumption of toroidal symmetry. The field of view that the cameras produce brightness images are processed using the Calcam[94] code to set up for the inversion process before finally inverting the data into the poloidal plane.

3.1 Camera data

The KL11 divertor camera system[95] has a field of view that covers the JET divertor, with lines of sight that have components in the toroidal and poloidal direction. The light passes through an endoscope leaving the vessel to reach CCD detectors after separation through wavelength filters. Neutral density filters protect the CCD amplifiers by reducing the intensity of all wavelengths evenly. Photons are detected by releasing an electron from the photocathode at the detector surface that is accelerated by an electric field towards a microchannel plate (MCP) (for the cameras that are fitted with an MCP). The MCP increases the number of electrons (gain) enough to be detected as a voltage. Factors for the neutral density and MCP gain are taken into account along with a calibration for the absolute brightness from an integrating sphere.

3.1.1 Camera image quality filtering

Apart from the various calibration factors, the brightness images are cleaned up by applying a background subtraction and a median filter. Some pixels have fixed brightness values, possibly due to damage so background subtraction removes this, and speckled noise possibly due to neutrons striking the sensor are removed using a median filter.

Further improvements to the images involve Fourier filtering of periodic oscillations in the image. When looking at an image before a pulse, horizontal oscillations are most clearly visible, and move vertically across the images over time but have the same frequency. Summing all rows of pixels shows a sinusoidal pattern of a fixed frequency. These are now filtered at this detected frequency by

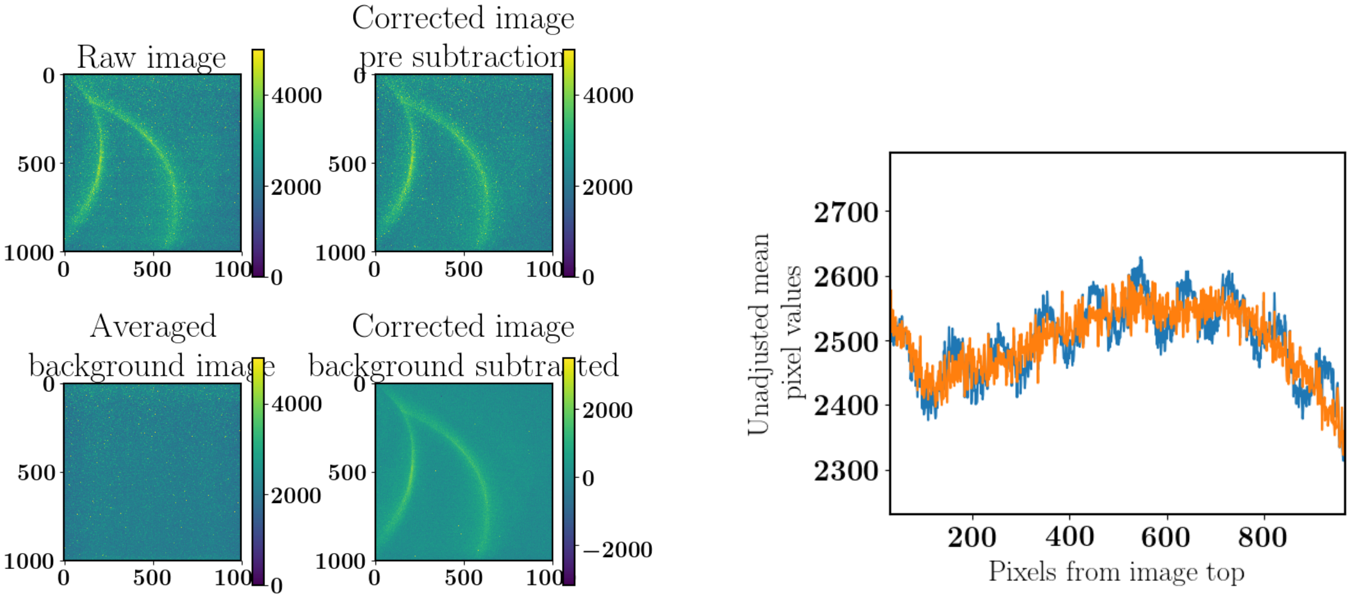

(a) Removing the horizontal oscillations using fourier filtering from a raw image (top left to top right) and background images (bottom left) before subtracting the image from the background to get a clear image (bottom left)

(b) horizontally averaged camera signal before (blue) and after (orange) removing horizontal oscillations plotted against the number of pixels from the top of the images in figure 10a

Figure 10

applying a fourier transformation, filtering out these frequencies, then applying the inverse fourier transform. This process now alters the process for background subtraction too as shown in figure 10, so 10 frames before plasma are filtered with the selected fourier range and then averaged.

To check this method, the 1st background frame is background subtracted using the averaged 10 background frames described above. If binned, the distribution of pixel values should be around 0. Before the fourier change, the peak is off zero in a skewed gaussian, whereas after the change the result is a gaussian centred around 0. Fitting the Fourier filtered images to a gaussian gives the standard deviation of the noise in the image σ_{bk}.

For later images the horizontal oscillations are also seen, but have higher brightness. The Fourier filtering method does not depend on the brightness so these are filtered out. The images are Fourier filtered first, then background subtracted before the median filter is applied.

3.1.2 Line integration

With the camera calibration in section 3.2 rays from each pixel are cast into the vessel and their path until reaching the walls are recorded. For each camera on KL11, there are 1 million pixels (1000 × 1000) to cast rays for and this is done assuming that the emission across a pixel is the same so that the line of sight can be approximated as a line integral.

The contribution from each volume element is used to calculate the signal detected at each pixel. The emissivity for each camera wavelength filter ($photonsm^{-3}sr^{-1}s^{-1}$), is evaluated at the point in space as $\epsilon(r,\theta,\phi)$, so the photons leaving the infinitesimal volume dV are $\epsilon(r,\theta,\phi)dV$. As photons are conserved in an optically thin plasma, this emission spreads out radially over a spherical surface with radius r_s. The photon density ($\rho_{surf}(r_s)$) on the sphere surface shown in equation 44, where r_s is also the radius away from the emission point.

$$\rho_{surf}(r_s) = \frac{\epsilon(r,\theta,\phi)dV}{4\pi r_s^2} \tag{44}$$

When looking at a distance between each dV element and the pixel surface, the size of the sphere has radius $r_s = r$ the only photons incident to the pixel surface is the surface density multiplied by the projected pixel area in this direction. The projected area is the fraction of the pixel seen at the point dV, multiplied by the area of the pixel at angle α between the vector between dV and pixel detector and the pixel aperture to pixel detector vector. The fraction is given as a weight function $W(r,\theta,\phi)$ so that the projected area given as $A_{proj}(r,\theta,\phi) = A_{det}cos(\alpha)W(r,\theta,\phi)$. Therefore for a single volume element the total number of photons incident on the the pixel surface (P_{det}) is shown in equation 45 where α is the angle between the detector normal and the selected point.

$$P_{det} = \frac{\epsilon(r,\theta,\phi)A_{det}cos(\alpha)W(r,\theta,\phi)dV}{4\pi r^2} \tag{45}$$

Over all volume elements the integral gives the contribution of all photons onto the pixel surface (P_{tot}), and can be split up into radial and area components shown in equation 46.

$$\begin{aligned} P_{tot} &= \iiint_V \frac{\epsilon(r,\theta,\phi)A_{det}cos(\alpha)W(r,\theta,\phi)dV}{4\pi r^2} \\ &= \frac{A_{det}}{4\pi}\int_r \frac{1}{r^2}\iint_A \epsilon(r,\theta,\phi)cos(\alpha)W(r,\theta,\phi)dAdr \end{aligned} \tag{46}$$

Equation 46 is a general integral for the photons but simplifications have to be made for the cameras because of the small angles between the camera aperture and pixel detector surface.

Assuming that all points are generated within a small angle between the central cone axis vector and the vector from the origin to the generated points is small, then the projected area is approximately just the pixel detector area projected in the direction of the vector between the detector-aperture centres, which is the z axis used in the problem. Using $A_{proj}(r,\theta,\phi) = A_{det}cos(\delta)W(r,\theta,\phi)$ where

$cos(\delta)$ is constant angle of the z axis to the area, the integral is now shown in equation 47.

$$P_{tot} = \frac{A_{proj}}{4\pi} \int_r \frac{1}{r^2} \iint_A \epsilon(r,\theta,\phi) W(r,\theta,\phi) dA dr \tag{47}$$

Where dA is the surface area of the emission volume perpendicular to the line of sight. This volume integral equation can be reduced to a line integral with additional assumptions to simplify the problem. The line integral assumes that the emissivity does not change over area, only over distance from the pixel surface, therefore $\epsilon(r,\theta,\phi) = \epsilon(r)$ and all of the pixel surface is visible $W(r,\theta,\phi) = 1$. The assumptions lead to equation 48.

$$\begin{aligned} P_{tot} &= \frac{A_{proj}}{4\pi} \int_r \frac{1}{r^2} \iint_A \epsilon(r,\theta,\phi) dA dr \\ &= \frac{A_{proj}}{4\pi} \int_r \frac{\epsilon(r)}{r^2} dr \iint_A dA \\ &= \frac{A_{proj}}{4\pi} \int_r \frac{\epsilon(r)}{r^2} dr \iint_A dA \end{aligned} \tag{48}$$

For a spherical capped cone, the area at each radial distance r is the total area of the sphere multiplied by the ratio of solid angle to total solid angle $4\pi r^2(\Omega_{det}/4\pi) = r^2\Omega_{det}$ where Ω_{det} is the solid angle of each area element. This reduced to equation 49.

$$P_{tot} = \frac{A_{proj}}{4\pi} \int_r \frac{\epsilon(r)}{r^2} r^2 \Omega dr = \frac{A_{proj}}{4\pi} \int_r \epsilon(r) \Omega_{det} dr \tag{49}$$

Equation 49 recovers the standard line integral result with $\Omega_{det} = \frac{A_{det}}{d^2}$ where d is the distance between the pixel aperture and pixel detector. This then links with the etendue of $E_{det} = A_{det}\frac{A_{ap}cos(\alpha)}{d^2}$ returning the standard line integral formula shown in equation 50.[96]

$$P_{tot} = \frac{E_{det}}{4\pi} \int_r \epsilon(r) dr \tag{50}$$

Equation 50 shows that under the assumption of constant emissivity at distance r from the pixel the total brightness is proportional to the line integral of emissivity. The solid angle of each pixel is small enough that this is considered a good approximation. However, the etendue on these cameras are not known so an absolute measurement is not possible, but an brightness calibration from the integrating sphere calibration takes this into account.

3.2 Camera spatial calibration

To invert from the camera view to the poloidal plane the first step involves tracing rays from each camera pixel and finding where they intersect the wall. This requires knowing the exact position of the camera, its field of view and any distortion in the camera system.

3.2.1 Theory of camera spatial calibration

Both the position, field of view and distortion of each camera are fitted in Calcam[94] using a camera lens model including distortion. To fit the camera model to a camera view, 3D points in a CAD model are marked $\begin{bmatrix} X \\ Y \\ Z \end{bmatrix}$ and linked to pixels on an image in 2D $\begin{bmatrix} U \\ V \\ 1 \end{bmatrix}$ as shown in figure 11. Equation 51 shows the relationship between these vectors by first applying the rotation and translation matrix with rotation elements R_{ij} and T_{ij}, followed by alignment with the focal length in each direction f_x, f_y and the optimal centre of the image c_x, c_y.

$$\begin{bmatrix} U \\ V \\ 1 \end{bmatrix} = \begin{bmatrix} f_x & 0 & c_x \\ 0 & f_y & c_y \\ 0 & 0 & 1 \end{bmatrix} \cdot \begin{bmatrix} R_{11} & R_{12} & R_{13} & T_1 \\ R_{21} & R_{22} & R_{23} & T_2 \\ R_{31} & R_{32} & R_{33} & T_3 \end{bmatrix} \cdot \begin{bmatrix} X \\ Y \\ Z \\ 1 \end{bmatrix} \tag{51}$$

Distortion is approximated using a Taylor approximation where the radial distortion is small closer to the optimal centre of the camera (distortion centre) and is symmetric, with radial distortion coefficients k_n for increasing r^2 coefficients. This introduces radial distortion as a polynomial in radial distance from the camera centre (r) squared. With different models to choose from this is not unique but is an approximation that has been regularly used, with distortion shown in equation 52.[97]

$$\begin{aligned} x_{rad} &= x(1 + k_1 r^2 + k_2 r^4) \\ y_{rad} &= y(1 + k_1 r^2 + k_2 r^4) \end{aligned} \tag{52}$$

Tangential distortion is much less important in the camera problem assuming proper camera alignment. It is due to effects such as slight change of angle the lens to the detector. The distortion is shown in equation 53 with coefficients p_1 and p_2.

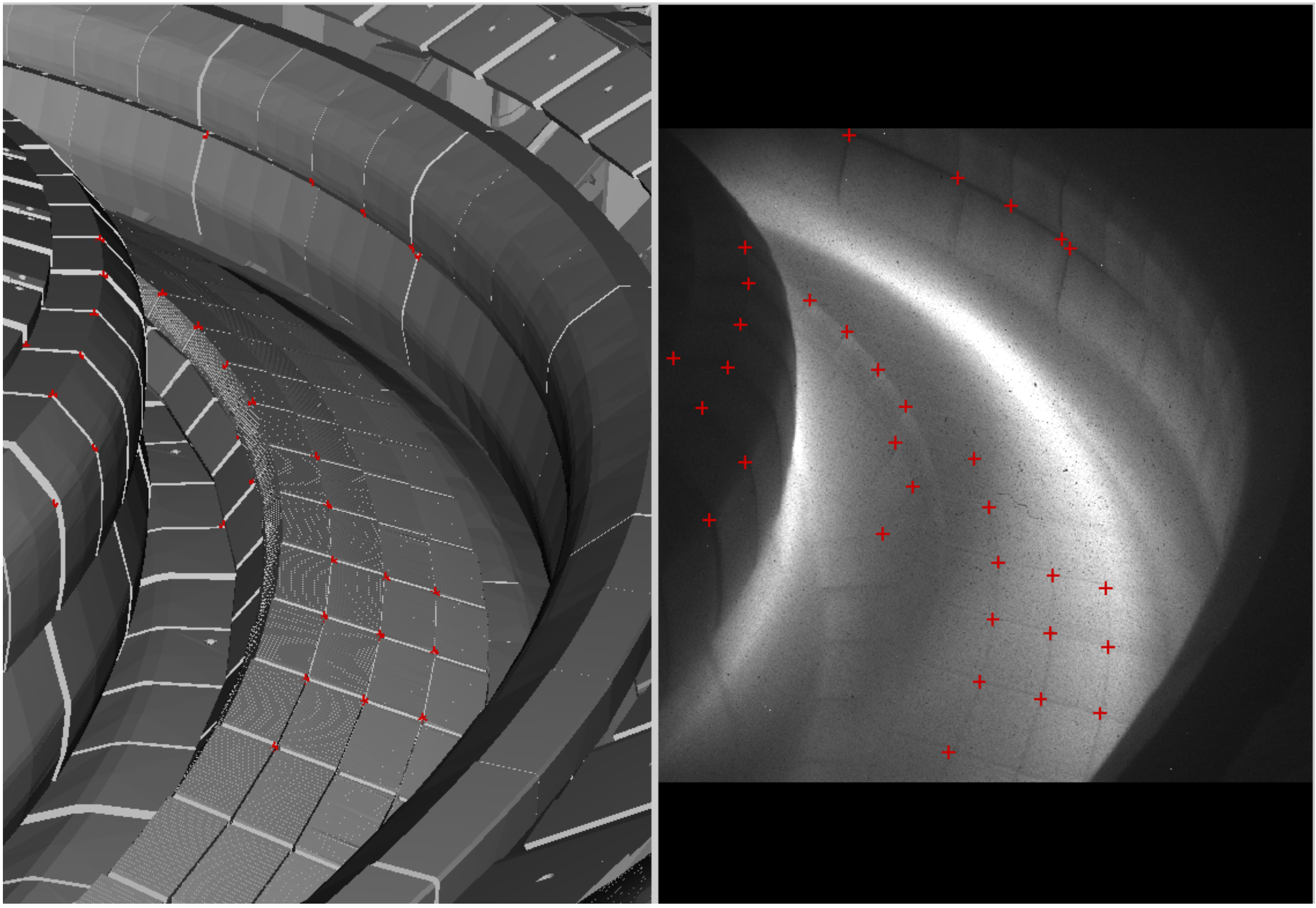

Figure 11: The CAD model (left) and a calibration image showing the divertor viewpoint of KL11 on JET. Red points are marked and matched between the left and right for spatially calibrating the camera view.

$$
\begin{aligned}
x_{tan} &= x + [2p_1xy + p_2(r^2 + 2x^2)] \\
y_{tan} &= y + [2p_2xy + p_1(r^2 + 2y^2)]
\end{aligned}
\tag{53}
$$

After the rotation and translation matrix is applied to X, Y, and Z - the right hand vector in equation 54 is created with a division by Z to allow a match to the left hand side of the z component of 1. After applying the rotation and Z constraint the distortion is calculated as $X' = x(1 + k_1r^2 + k_2r^4) + [2p_1xy + p_2(r^2 + 2x^2)]$ and $Y' = y(1 + k_1r^2 + k_2r^4) + [2p_2xy + p_1(r^2 + 2y^2)]$

$$
\begin{bmatrix} U \\ V \\ 1 \end{bmatrix} = \begin{bmatrix} f_x & 0 & c_x \\ 0 & f_y & c_y \\ 0 & 0 & 1 \end{bmatrix} \cdot \begin{bmatrix} X' \\ Y' \\ 1 \end{bmatrix}
\tag{54}
$$

3.2.2 Fitting and using the camera spatial calibration

The fit of the camera model is originally done in openCV[98] but testing of how well constrained and the error on this fit was done using Bayesian gibbs chain markov chain monte carlo. Assuming $f_x = f_y$ and k_3 and higher terms are ignored, the fit is well constrained, so this form of Bayesian analysis was useful for determining how good a fit is created.

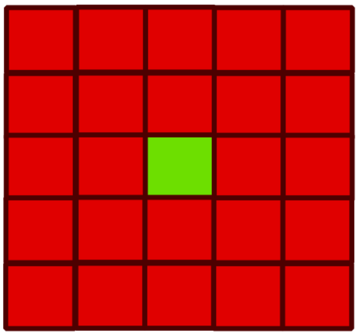

Figure 12: The space around a central pixel (green) with a spatial calibration uncertainty between 1-2 pixels is shown (in red) and used to estimate the maximum uncertainty on the central pixel value.

During the fit, a mean error in number of pixels between the left an right hand side of equation 54 is calculated for all fitted points using the square root of the sum of the squares of differences per fitting point. The mean error per pixel is propagated to an error in brightness σ_{cal} by calculating the maximum difference in brightness between every pixel and every other pixel within the spatial calibration pixel error. For example, with a mean pixel uncertainty between 1 and 2 pixel, a grid of 10×10 (2 pixels away from the centre pixel in all directions), shown in figure 12, would be drawn around every pixel and the largest difference in brightness is an estimate for the uncertainty from the spatial calibration fitting. The uncertainty in the brightness from this source and the background noise are combined in quadrature to get the total estimated uncertainty in the brightness in equation 55.

$$\sigma_y = \sqrt{(\sigma_{bk}^2 + \sigma_{cal}^2)} \tag{55}$$

The features on a calibration image must be clearly seen in both the image and the CAD model to match. If the calibration fitted points are transferred between cameras or between the different pulses then shift can be small but the points must be clearly defined. It is possible to have a low calibration error from placing points on a 3D CAD model, but this is only reliable if these points can be seen in the calibration image. Different spectral filters will have slight deviation due to differences in their refractive indices, in position and fitting parameters, so separate calibrations are performed for each camera. Previously the camera images used for calibration were taken from different pulses that had disrupted before the pulse of interest was ran. Disrupted pulses produce larger amounts of light in the vessel, enough to see all the features clearly at once. However the disruption events can shake the vessel, so displace the camera position we are trying to calibrate, so in this analysis the calibrations are taken over multiple frames in each pulse. In detachment experiments different parts of the divertor are illuminated over the duration of a pulse, allowing the points of the spatial calibration to be identified. Certain filters such as D_γ have much lower intensity and it is tricky to see features clearly, so more camera frames are required to highlight enough points on the CAD model for a reliable spatial calibration.

3.3 Camera inversions

Camera emission profiles in the poloidal plane can be used to calculate emissivities or line ratios of camera emissivities and track for further model comparisons. The most useful view point in the lines of sight is of the poloidal plane, while assuming toroidally symmetric emission. Successfully reproducing emission in the poloidal plane is only possible through either multiple cameras, with more line of sight coverage, or the poloidal and toroidal lines of sight combined with toroidal symmetry to give enough information to constrain emission in this viewpoint. It is not a perfect setup, and after inversions there are still places that the emission can exist in different poloidal positions that would still reproduce the camera image view.[99] The multiple possible solutions available means that there is a need to find a solution that both agree with the camera brightness and is a physically possible solution.

After the rays are traced throughout the vessel, the components of each are converted to the poloidal plane in a “geometry matrix”. This process is where toroidal symmetry is assumed. A meshed grid is constructed in the poloidal plane and each ray has its length in each mesh cell (in $r = \sqrt{x^2 + y^2 + z^2}$) is recorded as an element of the matrix G_{ij}, where ‘i’ is the ith pixel and ‘j’ is the jth cell in the mesh grid. There is no order to the pixels or mesh cells necessary, just aligned with a column vector of pixels y and column vector of emissivity for each mesh cell b. The linear equation is therefore shown in equation 56. In this equation G and y are well defined and known, but to solve exactly for emissivity b the inverse G^{-1} must be well defined. The inverse being required classifies this as an inversion problem.

$$\begin{aligned} y &= Gb \\ b &= G^{-1}y \end{aligned} \tag{56}$$

As G is not a square matrix and so does not have an exact inverse. This means that the problem of determining b is defined as "ill posed" with no uniquely determined solution. Computing a pseudo inverse is a possible solution but the condition of the problem makes this a poor approximation. The matrix G^{-1} is ill conditioned because small changes to the original matrix G mean large changes to G^{-1} and when applied to y, larger changes to emissivity b.

The best solution is not to compute G^{-1}, but instead iterate on the forward problem Gb which is well defined. By iterating through emissivity b, the most likely solution b is when Gb fits the data best. One simple method is to minimise the sum of the squares of the residuals $|y - Gb|^2$. For larger numbers of emissivity grid cells, it takes more resources to iterate, so while algorithms still use this principle they need to iterate fast enough.

The algorithm used in this thesis to solve the inversion problem is is called Simultaneous Algebraic reconstruction technique (SART)[100]. It begins with a uniform emissivity profile and shifts it in a way to reach a closer match to the brightness until the emissivity stops changing (gradient decent type algorithm) or reaches a maximum number of total iterations. The important part of this solution is that before evaluating the solution convergence, the emissivity is enforced to be positive. This will reduce the number of possible solutions available to the solver and confine it to solutions that make physical sense.

To propagate the uncertainty from the brightness in equation 55 to an uncertainty on the emissivity, bounds are estimated for how much the emissivity in one grid cell can change and still reproduce a brightness Gb within the uncertainty in equation 55. The maximum value to satisfy this for each emissivity grid cell is calculated as σ_{bmax}. This shown for an emissivity poloidal grid cell $j = 1, ..., m$ for every pixel in the range $i = 1, ..., n$ in equation 57.

$$(\sigma_{bmax})_j = MAX_{i=0}^{i=n}(G_{i,j}(\sigma_b)_j - (\sigma_y)_i) \tag{57}$$

The uncertainty estimate does not account for uncertainty that the inversion is a non-unique solution but it gives a useful uncertainty estimate. The uncertainty and profile for an example emissivity are shown in figure 13. The uncertainty profile does not vary that much across the poloidal profile but it shows a background level of $20 - 30\%$ of the maximum emissivity in figure 13a.

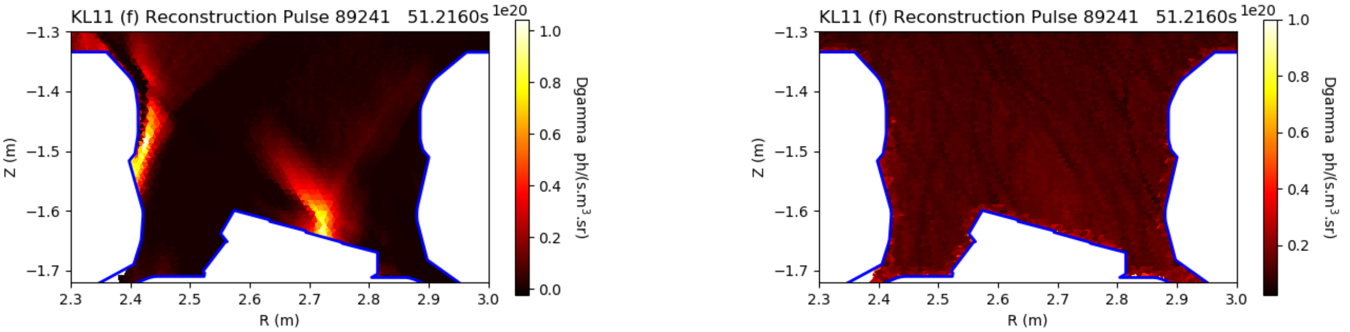

(a) An example KL11 inverted D_γ poloidal profile

(b) An example error for a KL11 inverted D_γ poloidal profile

Figure 13

4 Tracking the detachment front location and determining control parameters

4.1 Assumptions and past techniques

KL11[95] camera data on JET have several options for wavelength filters on up to 4 different cameras called channels (c-f). Filters for D_α (656.1 nm), D_γ (434 nm) and NII (500.4 nm) spectral lines are considered. Ultimately what is needed from these camera data is a position away from the target that represents a level of detachment consistently. During detachment, a low temperature region expands from the target with increasing depth of detachment, so a fixed temperature along the outer leg moves away from the target as the temperature profile moves. Spatial measurements for a fixed temperature have been estimated from looking at impurity emission lines, and on carbon wall machines it is suitable to look at CIII emission as a roughly fixed temperature measurement[58;60]. On JET, the ITER-like wall has tungsten and tungsten coated carbon divertor tiles and Beryllium outer wall, which means that the carbon density won't be as high as carbon wall machines like TCV.

Some pulses of interest use nitrogen seeding and it was investigated if the NII filtered camera images were useful for analysing the pulses in this thesis. This gives a direct measurement of emission which

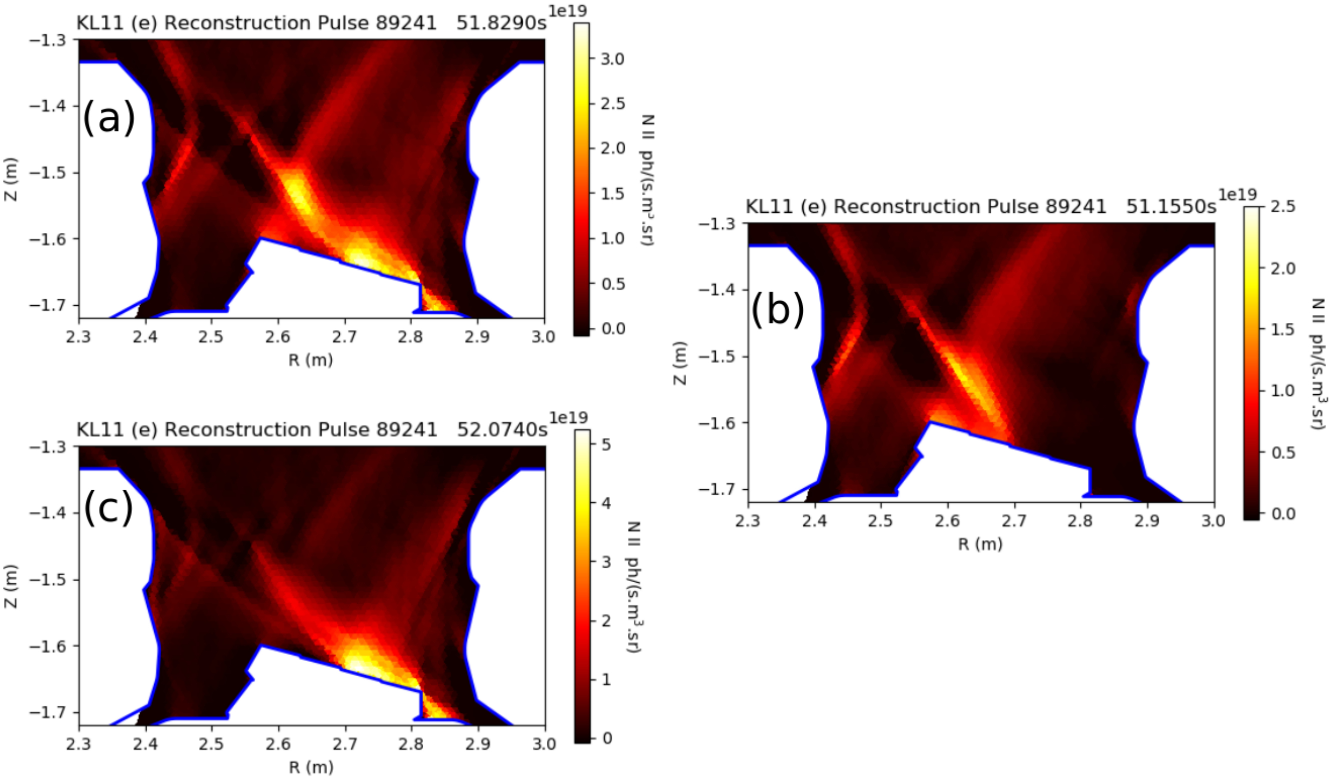

Figure 14: NII inversions with (a) Both ELM and no ELM visible (b) No ELM visible (c) ELM is the most visible part of the inversion

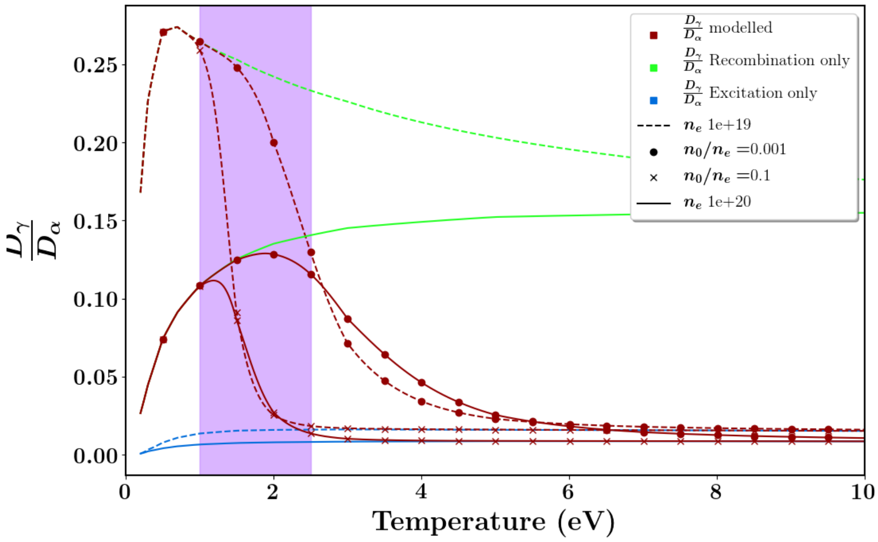

Figure 15: Model of D_γ/D_α emission using ADAS recombination and emission components for D_γ and D_α at different electron densities and neutral fractions. The components if only recombination emission is considered and if only excitation emission is considered are shown to highlight the change in which component is dominant for predicted D_γ/D_α values.

contains a clear peak in the divertor. One problem with some Nitrogen seeded pulses was tracking in H-mode, in which ELMs attach the divertor temporarily and result in a very high increase in the target NII emission over a time shorter than the exposure time of the camera as shown in figure 14(c) compared to inter-ELM emission in figure 14(b) . The camera exposure time of 30ms gives enough time for the ELM to occur and the divertor to recover, which the inter-ELM NII emission is still collected by the camera and partially seen in the divertor as shown in figure 14(a). This can sometimes be seen, as shown figure 14(c), but is more difficult to track. The intra-ELM NII emission is generally peaked on a flux surface in the SOL further from the separatrix and is spread over the divertor target. It is possible to track a front position for some frames, but as the ELM frequency increases, it becomes impossible to distinguish between intra-ELM and inter-ELM emission, as shown in figure 14(c). Since the exposure time of the camera at 30ms is already large compared to intra-ELM period, missing frames or sections of time that are tricky to track peaks in make it unsuitable for tracking a detachment front. If using a camera with higher frame rate (and shorter exposure time), then impurity lines could be considered more useful for H-mode pulses, at least for orientation of what is happening in the pulse. Even for higher frame rates, the NII emission might not be ideal for a detachment front measurement due to changes in nitrogen concentration and that the temperature of the peak would be high (3-5eV range). Impurity lines would therefore be more useful for predicting the onset of detachment or for intra-ELM analysis.[63]

Tracking spectral line emission features that appear at lower temperatures would be more convincing criteria that detachment has been reached, as there would be a larger low temperature region to potentially give a larger distance between the ionisation front and the target, while also allowing an increase in recombination. Tracking a lower temperature range is more desirable, but hydrogen (or one of its isotopes) transitions such as in the Balmer series are dependent on temperature and density, modelled from recombination and excitation components from equation 5. Over a temperature range, at a fixed electron and neutral density there is a transition between the recombination term in equation 5 being stronger at low temperature to becoming weaker at higher temperature depending on the transition. As the recombination and excitation emission is indistinguishable for a single Balmer line, the ratio of 2 spectral lines[89] with slightly different temperature ranges is better for highlighting the change between recombination and excitation dominant emission, which in turn highlights a temperature gradient.

The line ratio D_γ/D_α can be modelled using equation 58 to show the transition between increased ratio of recombination to excitation, shown in figure 15 for a range of electron densities and neutral densities. Figure 15 shows that there is a transition between recombination dominant emission with higher $\frac{D_\gamma}{D_\alpha}$ (at lower temperatures) and excitation dominant $\frac{D_\gamma}{D_\alpha}$ (at higher temperatures) within a temperature range of $T_r = 1 - 2.5eV$. It also shows that T_r is weak function of n_0 and n_e for $0.001 < n_0/n_e < 0.1$ and $1 \times 10^{19} < n_e < 1 \times 10^{20}$ which are used in figure 15. As temperature is increased, the start of the drop in $\frac{D_\gamma}{D_\alpha}$ is found between 1-2.5eV, which is toward the cold end of the detachment front where recombination rates decrease. Molecular emission is known to increase emission in the D_α wavelength range that would decrease the magnitude of $\frac{D_\gamma}{D_\alpha}$ overall[71] but the sharp reduction of $\frac{D_\gamma}{D_\alpha}$ in figure 15 would not be shifted away from the 1-2.5eV temperature range.

$$\frac{D_\gamma}{D_\alpha} = \frac{D_{5\to2}}{D_{3\to2}} = \frac{PEC^{exc}_{5\to2}n_e^2 + PEC^{rec}_{5\to2}n_e n_0}{PEC^{exc}_{3\to2}n_e^2 + PEC^{rec}_{3\to2}n_e n_0} \tag{58}$$

The small range in temperature of this transition temperature means that the transition of $\frac{D_\gamma}{D_\alpha}$ is approximately a function of temperature alone. If the electron temperature must be increasing over a particular region in the vessel and a drop in $\frac{D_\gamma}{D_\alpha}$ is also seen, then the temperature must be in the range 1-2.5eV over a reasonable range of neutral and electron densities. The temperature must decrease from the X-point towards the divertor target along a field line, so looking in the direction of the field line to find a rise in $\frac{D_\gamma}{D_\alpha}$ gives a consistent measure of low temperature location.

$\frac{D_\gamma}{D_\alpha}$ over the full frame time of 30ms in the KL11 cameras appears to be only mildly affected by ELMs. The NII line has very large increases in emission as the higher temperature region is brought closer

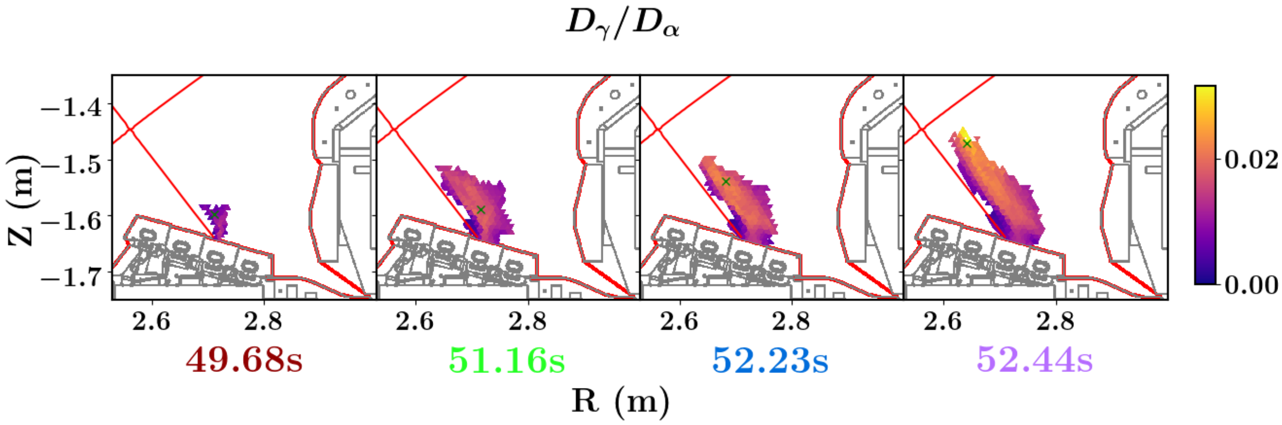

Figure 16: A grid of example inverted image ratios at different stages of detachment in JET pulse number (JPN) 89241. The inverted data is only plotted in the region of the common flux region near to the separatrix. A blue 'x' marks the point where the ratio is at 90% of its peak value.

to the target, however the opposite appears true for $\frac{D_\gamma}{D_\alpha}$[63]. At higher temperature, $\frac{D_\gamma}{D_\alpha}$ is lower, so over the 30ms exposure time of the camera, the $\sim$ 1ms intra-ELM period may reduce the $\frac{D_\gamma}{D_\alpha}$ to much lower values. This would not cause large increases in radiation but cause a small drop in the $\frac{D_\gamma}{D_\alpha}$ over the camera frame. Nothing in this analysis is highly dependent on the value of $\frac{D_\gamma}{D_\alpha}$, so this can still be used as the inter-ELM low temperature location tracker.

4.2 $\frac{\mathbf{D}_\gamma}{\mathbf{D}_\alpha}$ 2D profiles

Taking the ratio of $\frac{D_\gamma}{D_\alpha}$ requires some bounds to the individual D_γ and D_α profiles to stop large spikes arising from noise in the data. For low emissivity values of each Balmer line (below the uncertainty), the magnitude of emissivity can vary by small amounts but may cause large variation in the line ratio. If D_α is varying within its noise level and D_γ is fixed at a significant value, then $\frac{D_\gamma}{D_\alpha}$ can massively change. Similarly if D_γ is varying within the uncertainty but D_α is fixed at a low value $\frac{D_\gamma}{D_\alpha}$ changes are large. This means that large spikes can appear in the poloidal $\frac{D_\gamma}{D_\alpha}$ profiles, or if dividing interpolated D_γ and D_α, when they are actually just artefacts due to noise.

Noisy spikes in $\frac{D_\gamma}{D_\alpha}$ have the most impact when D_γ or D_α emissivity is low and within its uncertainty. Limiting the display and calculation for using D_γ or D_α only when above the their uncertainty previously calculated in equation 57 and shown in figure 13. In Field et al. [2017], $\frac{D_\gamma}{D_\alpha}$ is calculated above fixed values of D_γ and D_α. Figure 16 shows some examples of D_γ and D_α after the processing steps discussed in this section.

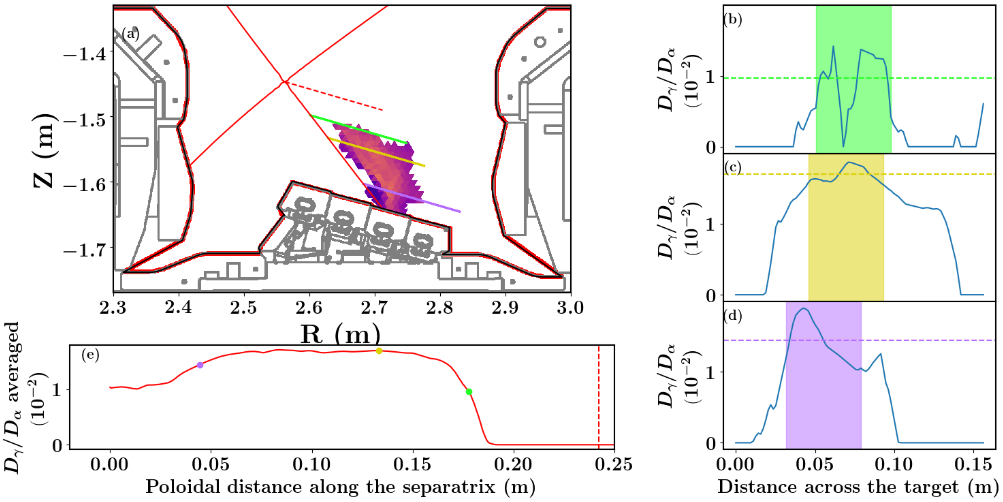

Figure 17: The detachment front edge search process is illustrated: a.) The search region is highlighted in blue along with the separatrix (red) along with the D_γ/D_α ratio 2D profile. b-d) Three smaller plots display the emission ratio obtained in the direction parallel to the target at 3 different distances along the separatrix shown in a.) The average of the highest 0.05m region along these profiles (shaded) is shown as dashed lines. e) the poloidal profile of D_γ/D_α ratio abstracted from this process; colored symbols correspond to the location of the lines, poloidally, in a.)

4.3 Tracking methods

In this section, a method for tracking the detachment front is introduced. Starting from 2D poloidal emission profiles, the emission needs to be reduced to a 1D profile in the direction of a flux surface. The method then reduces each 1D profile to a key position along the flux surface which is finally converted to a position along a field line and a z position along a flux tube as defined in section 2.6.3.

Tracking methods that use flux surface r, z data from the equilibrium were found to be more subject to noise than other methods that do not use flux surfaces to find the $\frac{D_\gamma}{D_\alpha}$ peak location. Highlighting a single flux tube based on large $\frac{D_\gamma}{D_\alpha}$ emissivity grid values introduced uncertainty from the emissivity grid, and linking that to a single flux surface created large spatial differences of where $\frac{D_\gamma}{D_\alpha}$ was tracked. Methods that relied on the gradient between flux surfaces and spatial averaging to interpolate $\frac{D_\gamma}{D_\alpha}$ removed the problems with aligning the equilibrium and emissivity grid, however were very dependent on the exact magnetic equilibrium from EFIT such that small changes will greatly alter the shape and peak of the final 1D profile. To mimimise the effect of the magnetic equilibrium on the estimated front positions, relying only on the position of the separatrix for initial peak detection while using spatial averaging showed an improvement to the stability of detected peaks.

To find the peak $\frac{D_\gamma}{D_\alpha}$ poloidally, a selection grid of [R,Z] points to interpolate and spatially average are selected with only using the equilibrium as a guide. [R,Z] points are evenly spaced along the separatrix and in the direction across the target tile 5 plate in the outboard direction to form a parallelogram of points. This is shown in figure 17 (a) where dashed lines extending from the separatrix are examples of 1 point extended in the direction parallel to the target plate. Each point generated is now the same distance away from the target plate as the corresponding starting point on the separatrix and can be averaged over the direction that follows the target plate to reduce to a 1D averaged profile along the separatrix. Figure 17 (b-d) shows how for each of the dashed coloured lines in figure 17 (a) look before taking an average. To make a more consistent average, a width of 0.05m region that has the highest average D_γ/D_α ratio in each profile is selected as the coloured region in figure 17 (b-d). These "horizontal" profiles are also useful for a later step when finding the [R,Z] position of a feature. The mean of each horizontal profile at every position parallel to the separatrix is shown in figure 17 (e), which show the values of averaged D_γ/D_α from the 3 coloured horizontal profiles in figures 17 (b-d) as the 3 coloured points. The detachment front location can now be found from this 1D profile, but the magnitude of D_γ/D_α has been lowered due to the spatial averaging. However the exact magnitude of D_γ/D_α is not required in any subsequent steps of the analysis, which is another benefit to this method.

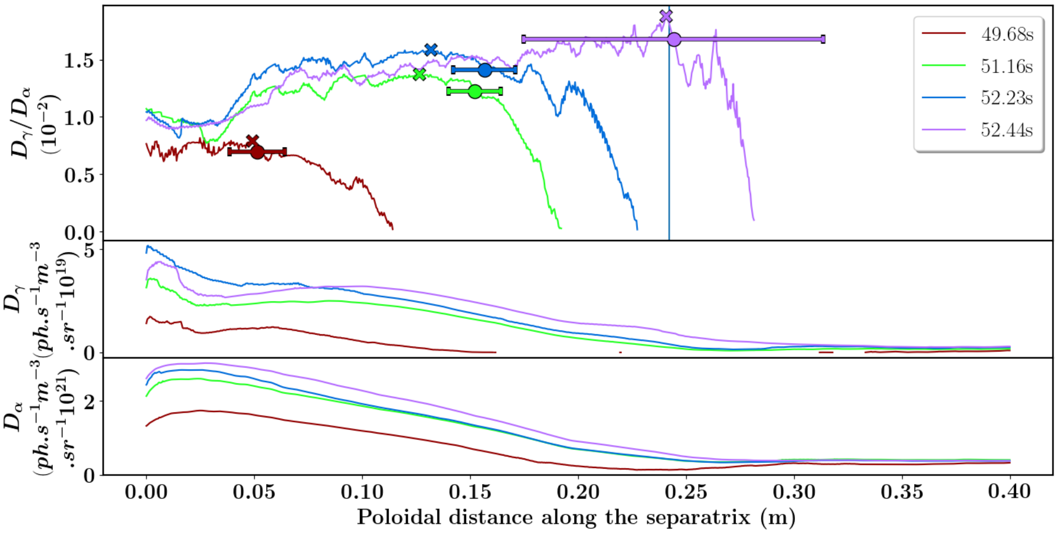

Figure 18: The detachment front edge search process is illustrated: a.) The D_γ/D_α ratio 2D profile over the search region which is limited to the common flux region near the separatrix; b-d) Three smaller plots display the emission ratio obtained in the direction parallel to the target at 3 different distances along the separatrix (highlighted in the corresponding color in a). The average of the highest 0.05m region along these profiles (shaded) is shown as dashed lines. e) the poloidal profile of D_γ/D_α ratio abstracted from the process shown in b)-d); colored symbols correspond to the location of the lines, poloidally, in a).

4.4 Front Position in a 1D profile

Profiles from the target towards the X-point parallel to the separatrix like those in figure 17 (e) are used to find a detachment front location to track over time. Section 4.1 highlights that the peak or large drops in D_γ/D_α as temperature increases could be a good measure for the detachment front. Figure 18, shows profiles over time for pulse 89241 where peak positions are detected (crosses) and drops to 90% of the peak D_γ/D_α. The peak position of the flat-top regions in the profile would make detecting the peak uncertain and is strongly dependent on noise. However, the drop between the peak and upstream occurs over a much shorter poloidal distance so is found to be more consistent to detect. Figure 15 shows that the decrease in D_γ/D_α as temperature increases is within a similarly small temperature range as the D_γ/D_α peak. Instead of using the peak D_γ/D_α, a percentage drop from the peak D_γ/D_α is chosen close enough to the peak but after a large enough D_γ/D_α reduction that a D_γ/D_α decrease is not due to noise. Testing values between a fall of D_γ/D_α from the peak position to be in a range between $90\% - 70\%$ does change the final peak position, but the separation does not expand greatly over this range. By 90% there is a significant enough drop to stabilise the noise in detachment front location but not move the detachment front location significantly far from the peak D_γ/D_α. Compared to the peak D_γ/D_α, the 90% fall off is both more well defined because the changes in D_γ/D_α are larger than close to the peak, and is also able to represent a similar temperature range in the divertor so it is used as the detachment front location measurement in this analysis.

4.5 Uncertainty propagation

The uncertainties have so far been propagated to the 2D poloidal emission profiles, but it is not clear about the assumptions (such as how interpolation effects gaussian distributed uncertainty found on the camera data) to propagate them further to the front position measurement. A more computationally intense method than analytical propagation is by using a monte carlo method of propagation. The 2D poloidal emission profiles have a distribution using the value of the emissivity profile as the peak and the uncertainty as the standard deviation to generate a multivariate normal distribution of values that the emission takes that can be sampled from. The full process described in sections 4.3 and 4.4 is repeated many times using these perturbed emissivities to get a distribution of peak positions that are possible within the range of emissivities that are possible.

4.6 Aligning with a flux surface

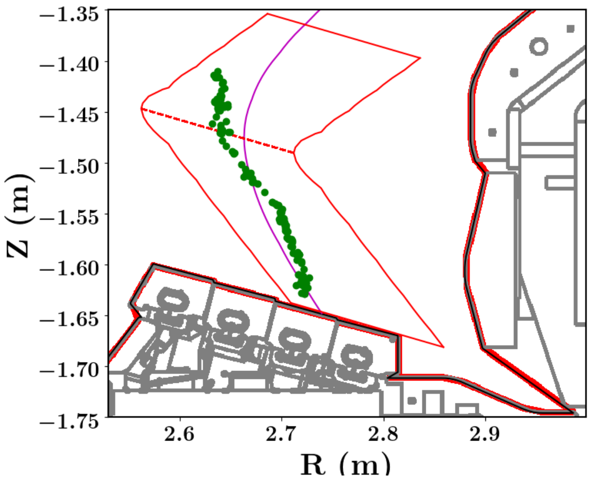

Figure 19: A simplified diagram of the JET divertor region to be analysed: Interpolation points in purple (front location at each time point in the pulse) are evenly spaced inside the red-outlined region that is shaded in figure 17. The purple line is the flux surface that is closest to all the green detected peaks, and the points are projected onto this line to make model comparisons. The blue line is the x-point location.

To compare to the DLS model in section 2.6.4, the data must be tracked along a flux tube over some period of time. To find the closest flux surface that aligns with the detachment front locations for each time point, the radial (R), vertical (Z) position of the front is located. The data is currently given in a poloidal distance in a straight line from the target, but at the 90% upstream fall off value will have a "horizontal" profile similar to figures 17 (b-d). To get an estimate of the detachment front position in [R,Z], the centre of mass of the "horizontal" profile is found, located at $x_{COM} = \frac{\Sigma xy}{\Sigma y}$ along this profile. Over all time frames, the [R,Z] position shifts at different stages of detachment but overall moves up the outer leg assumed along the same field line.

To compare this to a path along a field line, for the purpose of the discharges in this thesis, the equilibrium is taken to be fixed and does not change much over time periods of interest. The average of the equilibrium gives a good representation of the field as the strike point moves by less than 1cm in each pulse analysed. By averaging all the values in the equilibrium over time, the small oscillations are removed. On the resulting equilibrium, the [R,Z] points are interpolated onto a normalised flux value Ψ_n which is on average distributed on a single flux surface. This average flux surface is used for model comparison by projecting the [R,Z] points onto the closest point on the flux surface. The purple flux surface in figure 19 shows the path closest to most of the points in pulse 89241 and how it matches to the [R,Z] front positions detected.

The DLS model requires the calculation of z_h position using the path of the field line from equation 24 where the poloidal distance along the field line l_p is known from the flux surface, and the total magnetic field at the X-point $B_\times$ and local poloidal magnetic field are found by interpolating onto values from EFIT.

From this stage onward all of the information used to calculate the right hand side of equation 36 has been calculated, using additional total local magnetic field values starting at the target and integrating upwards in dz. The left hand side is not dependent on camera data, nor does it require good spatial resolution of the detachment front for P_{SOL} and n_u components.

4.7 Determining control parameters

4.7.1 $\mathbf{P_{SOL}}$ Calculation

Power balance in the core can be used to calculate P_{SOL}, which is predicted to affect the divertor conditions and must be calculated to compare to the DLS model.

Power is injected from external heating systems through either injecting particles, such as neutral beam injectors (NBI); inducing a current in the plasma generating heat from resistance, known as Ohmic heating power (Ohm); or by causing resonance with an electro magnetic wave for example, ion or electron cyclotron resonance heating (ICRH), or lower hybrid current drive (LHCD). The plasma retains some of this input energy, which can be calculated from several different methods[101]. Most commonly used is the plasma response detected through diamagnetic loop coils, using the equilibrium to get the stored energy (W_{dia}) and differentiated over time to get the stored power (Y_{wd}).

$$\begin{aligned} P_{in} &= P_{NBI} + P_{ohm} + P_{ICRH} \\ P_{SOL} &= P_{in} - Y_{wd} - P_{shi} - P_{rad_c} - P_{c_x} \end{aligned} \tag{59}$$

As P_{SOL} can't be directly measured on JET, it is estimated by balancing the heating power with losses as shown in equation 59. This calculated with a standard method for JET, including similar smoothing of the data as described later, with the main difference of separating out the inter-ELM contributions. Taking into account losses from the NBI shine-through (P_{shi}) and the total power radiated in the core (P_{rad_c}), along with energy lost due to charge exchange (P_{c_x}) and the rate of change of stored energy Y_{wd} balances with the total injected power (P_{in}). (P_{rad_c}) is calculated for JET using a weighted sum of bolometer chords to discount the divertor radiation. The P_{shi}, P_{c_x} measurements are taken as the same data signals used in the original JET standard calculation, whereas P_{rad_c} is calculated inter-ELM, special inter-ELM calculation for Y_{wd} and calculating P_{in} from its components.

The Y_{wd} signal would normally be calculated by some numerical method of differentiating stored energy W_{dia} to get the total power, but here it is re-calculated after removal of ELM peaks. The inter-ELM change is calculated by approximating the increase in W_{dia} between 2 ELMs as linear

$\frac{dW_{dia}}{dt}$ in time range dt and finding the gradient. This method ignores the intra-ELM changes to give an inter-ELM measurement. Outside of H-mode, a standard measurement is used for Y_{wd}.

The power is known to be split between the inner and outer divertor, and is likely to be an uneven split. The distribution of quantities behaving differently between the LFS and HFS is called in-out asymmetry, however this has actually been shown to be a function of the magnitude of P_{SOL}[102]. Given that most of the P_{SOL} in total ends up on the LFS and there is not enough information to determine the proportion to the inner and outer divertor, P_{SOL} is left as the total value where only relative change of P_{SOL} is required in the DLS model.

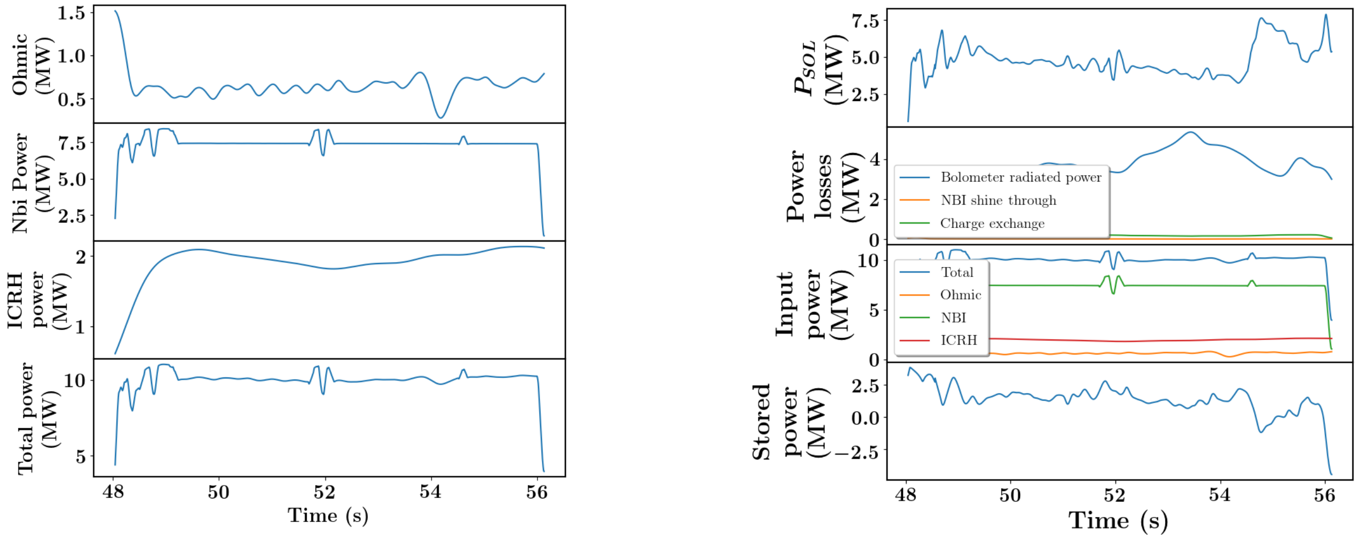

(a) Raw and processed signals which contribute to the calculation of total power

(b) Raw and processed signals which contribute to the calculation of P_{SOL}

Figure 20

To calculate P_{SOL} on JET, several smoothing and filtering factors are used. The NBI power is smoothed with a gaussian kernel with full width half maximum (FWHM) of $0.235s$ because sharp jumps in the NBI power occur after it has been increased that would not all reach the SOL at the same time but over the order of the confinement time ($\sim 100ms$). The time base of the other power input signals are sampled at a much lower frequency, so P_{ohm} and P_{ICRH} are smoothed with a FWHM of $70ms$ before being interpolated onto the NBI time base. The signals Y_{wd}, P_{shi} and P_{c_x} are calculated from other codes to determine their values for equation 59 to calculate P_{SOL}, and are also interpolated onto NBI signal time base since they are already smooth. Core radiation P_{rad_c} is measured from the bolometer data with weightings to only identify core radiation. This signal is already pre-smoothed lightly over ~ 10 data points by previous processing, but because the inter ELM P_{SOL} is required, it is then filtered for ELMs and re-smoothed with the same gaussian smoothing kernel of $70ms$ fwhm before being interpolated onto the NBI time base. The calculation is then made using equation 59 and plotted with all components in figure 20b as an example.

4.7.2 $\mathbf{n_u}$ Determination

The upstream density in the DLS model is a boundary condition introduced through the Lengyel formulation of radiated power and a balance of plasma pressure from the thermal front to the upstream point. Upstream density is defined at the midplane on the separatrix. Unfortunately, the position of the separatrix is difficult to determine accurately. Particularly in H-mode, in the pedestal, there is a large spatial gradient in density[103]; attempting to match this to a very precise and uncertain flux surface is a problem. Comparison of experiments to the DLS model requires a relative change in density for the front position to move. Therefore a noisy signal for the upstream density will be a problem for predicting front position changes, particularly as the upstream density is predicted to be the control parameter with the highest sensitivity. The standard method for determining the separatrix position at the upstream point on JET is at a fixed temperature measurement which is more stable than reconstructed equilibria. The problem is that the fixed temperature value, at 100eV for JET in H-mode, is only an estimate, and there is likely to be a constant offset between this and the true separatrix position. This is overall why methods of refining calculations of n_u are introduced in this thesis.

4.7.2.1 Thomson Scattering

The upstream density can be estimated as the Thomson scattering electron density at the separatrix position r_{sep}, where r_{sep} is estimated from Thomson scattering temperature measurements. For the JET KE11 diagnostic, the elastic scattering of light from a Q-switched Nd:YAG LASER (1064nm) is detected at 63 spatial points and separated into wavelengths. For stationary electrons in the plasma, the elastic scattering means that photons are detected at the exact same wavelength but the high temperature in the plasma causes the moving electrons to doppler shift the light. An electron temperature can be derived from the distribution of scattered photons in wavelength and an electron density from the scattered intensity[104]. The spatial points give a radial resolution of $\sim 1 - 1.6$ cm radially towards the outboard midplane through the pedestal across the separatrix and into the SOL. The detector is located at the top of the machine.

The separatrix location is not determined using the equilibrium, as the width of the pedestal in H-mode is of the same order as spatial uncertainties in EFIT ($\sim 1cm$), so an alternative approach is needed to estimate the separatrix position in the Thomson profiles. To estimate the separatrix location on JET a fixed temperature in the pedestal is determined. Starting from equation 13 with

$T_t^{7/2} << T_u^{7/2}$ and with the assumption that half of the total P_{SOL} reaches the divertor target and flows through an area $A = 2\pi R\lambda_q B_{pol}/B$ similar to equation 35 and approximating $q_{||} = (P_{SOL}/2)/A$. This gives a rough approximation of temperature in equation 60 that when used in the case of pulses described in section 4.11. Using this equation the H-mode pulses studied have $T_{e,sep} \sim 100eV$ which typical for H-mode pulses on JET, while the L-mode pulses reach $T_{e,sep} \sim 60eV$.

$$T_u^{7/2} = \frac{7}{8}\frac{P_{SOL}B}{\pi R\lambda_q B_{pol}}\frac{L}{\kappa_{0e}} \tag{60}$$

To estimate the upstream density at the separatrix, the R position which aligns with where T_u is located in the pedestal temperature profile is required. Methods have started with fitting both the density and temperature profiles with a modified tanh function that matches the pedestal temperature and density profiles.[105] [106] This can fit well to the overall pedestal profile but the fit will depend on how many spatial points into the core are input, and for its use in this thesis the fit has to be in good agreement with the data around the separatrix. In H-mode, there are between 1 and 3 spatial points in the Thomson profiles across the pedestal density profile on JET. The low number of spatial points near the separatrix makes an upstream density measurement much more uncertain when fitted, as a slight error in this region can greatly change the inferred value.

Instead of fitting the pedestal profiles, the analysis is simplified to avoid compounding uncertainty in fitted parameters. For the purpose of this analysis, density is only required at a single radial point, and noise in the temperature and density profile data appear much smaller than the change in the pedestal gradient show in figure 22a, so an interpolation method would have reasonable consistency. The temperature profile is linearly interpolated between spatial points where the temperature first drops below the fixed T_u value from the core to the SOL. This gives a position of the separatrix r_{sep} which is then interpolated on the density profile to get an upstream density estimate. The uncertainty in r_{sep} appears small, however for very steep H-mode pedestal gradients this becomes a very large uncertainty on upstream density. The first method was attempted to combine with the lithium beam to produce a better spatial resolution in the pedestal which will be described in section 4.8.

4.7.2.2 Lithium beam density measurement

To measure the electron density profile, a beam of neutral lithium is injected at energies of 20-70kV[107] into the plasma to measure excited lithium lines at 670.78 nm using a spectrometer. The density profile is found by "unfolding" the emission profile of this line by iterating through possible density profiles to find the one that matches the measured emission profile of the line, including attenuation as the beam passes through the plasma and the lifetime of the atomic transition.[108]

The profiles are measured from a vertical line of sight at R=3.252 m using 26 spectrometer channels, but provide a better spatial resolution than the Thomson scattering. The lithium beam doesn't measure temperature so to get the upstream density the Thomson temperature profiles have to be used to estimate r_{sep} as described in the previous section. The two diagnostics have different spatial measurement points which need to be mapped onto the same flux surfaces. The problem is that this requires good resolution of EFIT reconstructions at the outer midplane. Figure 22a shows that flux mapped densities between the Thomson and lithium beams don't align at the pedestal density gradient. This means that one would possibly need manual alignment which would make this method difficult to calculate over all pulses at all times.

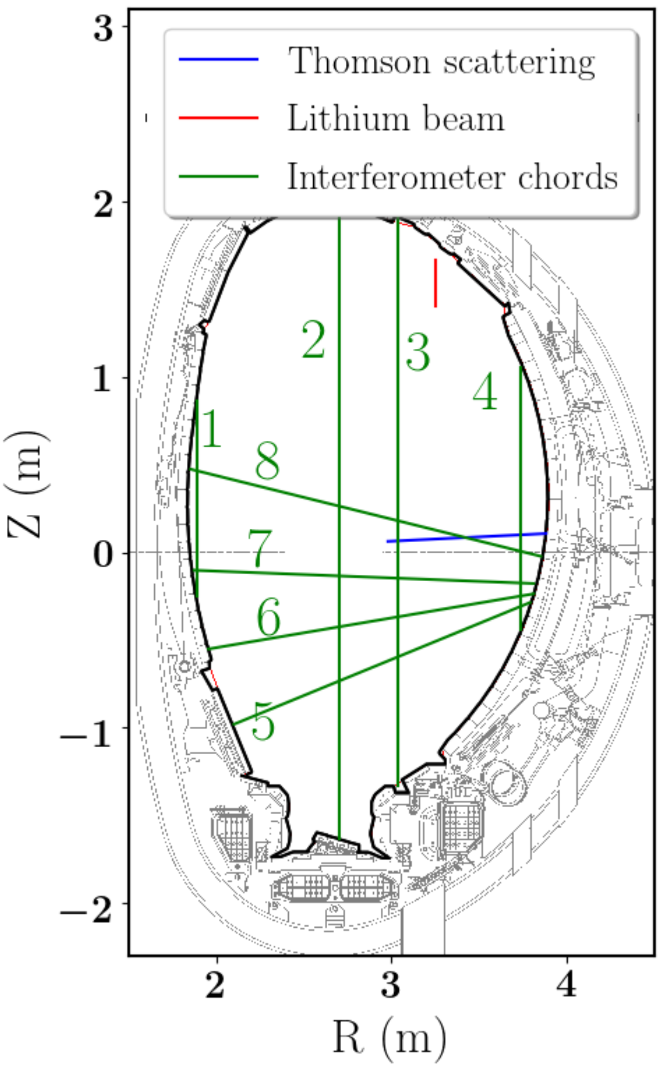

Figure 21: Poloidal cross-section of JET displaying the plasma facing component surfaces as well as the various interferometer chords ('lidX' where 'X' is in the range 1-8). The measurement locations for the Thomson scattering measurements are shown as well by the blue line and the lithium beam measurement locations are shown in red

4.7.2.3 FIR Interferometry

The density variation for an interferometer line-integrated measurement of density, along a line of sight close to the separatrix was examined.

On JET, a 120 mW methanol laser ($118.8\mu m$) passing through the plasma[107] experiences a phase change as a function of optical path length as $\phi = 2\pi\frac{OPL}{\lambda}$. The optical path length (OPL) is a function of the refractive index N over distance s as $OPL = \int_s Nds$. Comparing to a vacuum path of the same length the optical path difference $\Delta\phi = 2\pi\frac{\int_s(1-N)ds}{\lambda}$. From the expression for the plasma frequency $\omega_p = (\frac{n_c e^2}{\epsilon_0 m_e})^{1/2}$ a cutoff density exists where the plasma reflects the incident electromagnetic wave. With a phase velocity $v_p = c/N$

that has frequency $v_p = \omega/k$ can be combined to get $ck = N\omega$. The dispersion equation for an electromagnetic wave with no magnetic field is $\omega^2 = \omega_p^2 + c^2k^2$, so substituting in $ck = N\omega$ gives $N = \sqrt{1 - \frac{\omega_p^2}{\omega^2}}$. This equation can be expanded for low $\frac{\omega_p^2}{\omega^2}$ to $N = 1 - \frac{\omega_p^2}{2\omega^2}$ which substitutes into the phase difference as $\Delta\phi = 2\pi\frac{\int_s(1-(1-\frac{\omega_p^2}{2\omega^2}))ds}{\lambda} = \pi\frac{\int_s(\frac{\omega_p^2}{\omega^2})ds}{\lambda}$ which due to plasma frequency changes leads to equation 61 showing that the line integral density can be calculated from the phase shift in the interferometer.[109]

$$\Delta\phi = \pi\frac{\int_s n(s)ds}{\lambda n_c} \tag{61}$$

This phase difference is observed because fringe changes in the interference pattern are observed at multiples (N_f) of $2\pi N_f = \Delta\phi$. However not detecting a change in the fringe pattern over time and by a factor of 2π can lead to jumps in the line integrated density seen.

There are 8 chords on JET, 4 vertical and 4 horizontal to cover the plasma over core and edge positions. The chords that are potentially useful are closer to the separatrix are lid4 and lid5. In some of the discharges used in this thesis, lid4 appears to have a large fringe jump at a point where density data is needed, so lid5 is taken as the most useful chord.

4.8 Consistency between density measurements

To get a more consistent measure of the upstream temperature, one of interferometer or density measurements should be combined with the Thomson measurements. Thomson profiles are close to the midplane in [R, Z] position as shown in figure 21 and have temperature and density profiles which make it the most useful for estimating the upstream density alone. However, removing some noise that occurs in the profile is possible by combining them with lithium beam or interferometer measurements.

Combining the Thomson with lithium beam density relies very heavily on flux mapping both to the midplane using the EFIT equilibrium reconstruction. The lithium beam density profile has a good spatial resolution compared with the Thomson profile after being mapped to the outer midplane, which would reduce uncertainties for the upstream density. However, the lithium beam is much further from the midplane in [R, Z] as shown in figure 21 combined with uncertainty in the equilibrium means that the Thomson and lithium density profiles don't fully align, as shown in figure 22a. This is a pre-requisite for aligning the r_{sep} from the Thomson data. One possible solution in future work

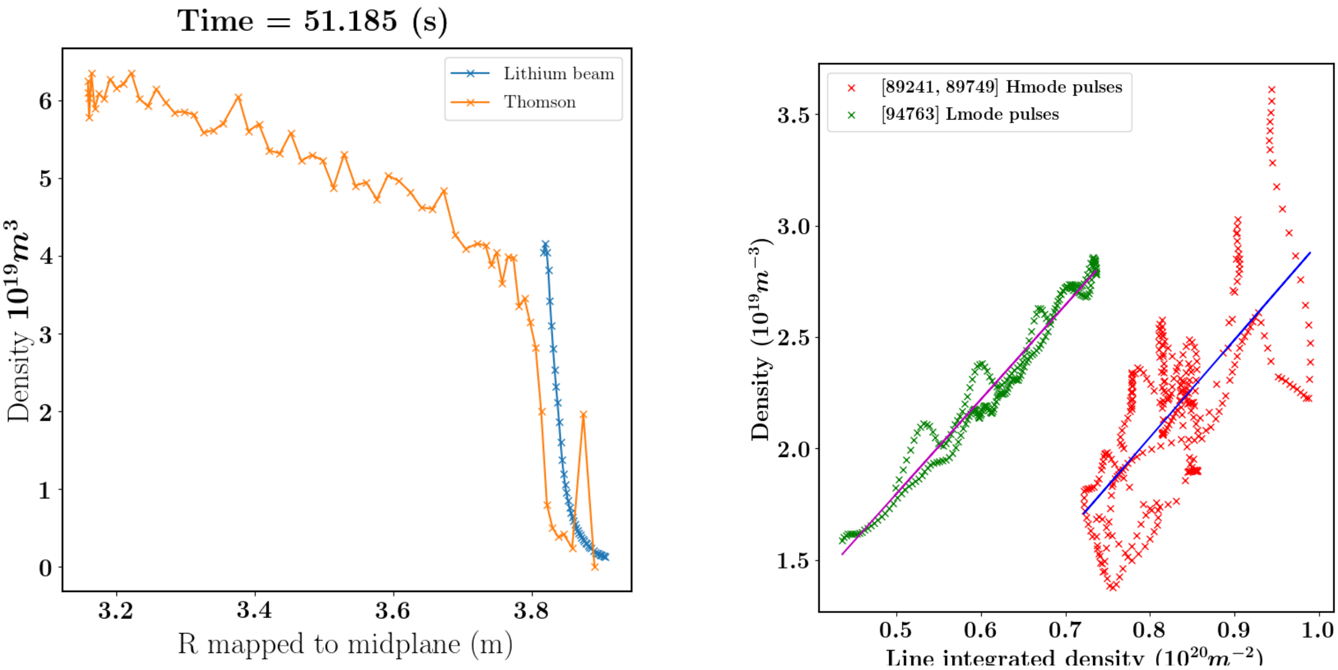

(a) A comparison of the lithium and Thomson profiles mapped to the midplane using and equilibria.

(b) A scaling relation between the line integrated density measurement (lid5) and the localised Thomson scattering density measurement (at $T_{e,sep} = 100eV$ for H-mode and 60eV for L-mode).

Figure 22

could be to try and align the density profiles with an offset, as the gradient in the pedestal appears to match as shown in figure 22a.

We have found that combining the Thomson density measurement with the lid5 line integrated density measurement is the best choice for providing a low noise n_u measurement. To match to line integrated interferometer measurements, the smoothed version of the upstream Thomson data are plotted against the line integrated density from a single chord (lid5) in figure 22b. Figure 22b shows an approximate linear dependence between the Thomson and lid5, which has been fitted so that by inputting lid5 interferometer data, a less noisy upstream density value can be determined. This produces a more stable upstream density measurement that is used in model comparison in this thesis.

4.8.1 f$_z$ Determination

The final control parameter, impurity concentration, is much harder to estimate accurately than the other 2 DLS control parameters. The impurity concentration definition is the ratio of all impurity density to the electron density $f_z = \frac{n_z}{n_e}$. This section outlines possible ways to infer the divertor impurity concentration in compared in section 4.12, as it is important to introduce specifics about the pulses for this comparison.

4.8.1.1 Nitrogen concentration proxy

In many of the discharges in this thesis, the primary impurity is expected to be nitrogen, as it is seeded into the divertor. As this investigation started, a spectroscopic technique did not exist to determine the nitrogen concentration, so an attempt to make a proxy that represents the nitrogen concentration was investigated. Spectrometer chords with a view of the divertor can measure nitrogen emission lines that will be a function of the concentration, and temperature.

A signal for NII (500nm) that has been summed over divertor spectrometer measurement chords was investigated as a proxy for impurity concentration. This seemed to match with initial discharges, but fails to be consistent on different pulses.

4.8.1.2 Nitrogen concentration

Henderson et al. [2018] introduces a technique to estimate the divertor nitrogen concentration that works out an ion density of nitrogen from an atomic transition with negligible recombination as well as the electron density from the ratio of different NII transitions over the line of sight of a spectrometer chord.

There are two problems that limit the availability of this measurement. The first is the settings of the spectrometer must be correctly defined to measure the required nitrogen emission lines. The next is that the inter-ELM signal is required for the analysis, but the method of determining the path length uses the inverted camera NII emissivity data from KL11. The original problems with determining the inter-ELM front position from NII are re-introduced in this measurement. In discharge 89241 where all the spectrometer information is present and nitrogen is seeded, the concentration can be estimated, but for most of the pulse the ELM frequency is high enough that the path length is only determined intra-ELM at the start of detachment. This can still be used for a comparison where good data is available.

4.8.1.3 $\mathbf{Z_{eff}}$ measurement

Fusion plasmas will always have some impurity content, whether high Z from the wall, seeded impurities or just helium from fusion products. To determine how these impurities contribute to radiation loss, a factor representative of the total impurity content, Z_{eff} is defined in equation 62. The denominator will have far lower contribution from impurities as the plasma is almost all Hydrogenic, so $\Sigma_i n_i Z_i \sim n_e$.

$$Z_{eff} = \frac{\Sigma_i n_i Z_i^2}{\Sigma_i n_i Z_i} = \frac{\Sigma_i n_i Z_i^2}{n_e} \tag{62}$$

Z_{eff} can either be determined by looking at the emission from spectral lines or Bremsstrahlung spectrum. At high temperatures within the LCFS, Bremstralung emission is more dominant due to electrons being slowed down by collisions with ions, which can be fitted to an emission model at a given temperature.[111] The spectral line method requires more complete coverage of wavelength ranges. The KS3 JET spectrometer covers many different spectral lines for horizontal and vertical lines of sight to give line averaged Z_{eff} measurements for each channel.

Since the Z_{eff} measurement is of the core plasma and not the divertor and relies on several assumptions on which impurities impact Z_{eff}, there is no clear relationship between Z_{eff} and the impurity concentration used in the DLS model. However as described later, we use Z_{eff} as a consistency check on what impurity relative change to impurity concentration is inferred. Core changes would show how much impurities are affecting the discharge in total but are not necessarily a reliable proxy for divertor changes.

4.8.2 Gas valve flux ratio

As nitrogen seeding has been used to feedback detachment control[112], it has to be related to impurity concentration from the DLS model perspective. Equation 63 is taken from Henderson et al. [2019] where it has been used as an alternative means of calculating the nitrogen concentration[113] [114]. The seeding rate of deuterium in the divertor Γ_D and nitrogen Γ_N are simply the ratio of recorded gas flow rates, which in the same units cancel in equation 63.

$$c_n = \frac{\Gamma_N/7}{\Gamma_D + \Gamma_N/7} \tag{63}$$

With a fixed Γ_D, as is the case among the analysed pulses the impurity concentration would just depend on Γ_N, however the question is if this is a good control parameter?

The basic model in equation 63 doesn't account for impurity build up in the divertor. For example, if the nitrogen gas flow is suddenly turned off then the divertor still contains a certain density of nitrogen. One alternative measure could be to calculate the cumulative seeding rate also using equation 63, however this has the opposite problem of not having any loss terms in this concentration estimate.

4.9 Ion flux Determination

The outer target ion flux is a key measurement of detachment as one of the measurements required to drop significantly. Langmuir probes are used to make measurements of the current over a sweep of the voltage bias applied to each probe. Langmuir probes can vary in shape, angle to field lines and the application of voltages.

For a Maxwell-Boltzmann distribution of velocities, the mean velocity of electrons $< v_e >$ can be found after several standard integration steps before being multiplied by charge and number to get the current j_e. Using quasi-neutrality arguments this gives the mean current shown in equation 64, with the ion saturation current j_{sat}, plasma and probe bias voltage and ion temperature T_i. For bias voltages larger than the plasma potential V_p, ions are not attracted at all so $j_e = j_{sat}$. This is generally shown by plotting the current against the probe voltage on I-V curves[115], then determining where current saturates at high negative bias such that only ions can be collected to find j_{sat}.

$$j_e = j_{sat} exp(\frac{-e(V_p - V_b)}{k_b T_i}) \tag{64}$$

Different assumptions can be added to alter equation 64 and the I-V curve, even the type of probe. The detailed analysis is not discussed here as the basic principle and the output are what are needed to discuss.

As stated on the JET data description, ion flux measurements are not made by fitting the I-V curve. Measurements at large negative bias are used as an approximation. The measurements made at higher electron temperature ($> 50eV$) could underestimate the ion flux, but most detached pulses used here will not exceed this temperature. An array of 36 probes between the inboard and outboard side of the divertor are used to get a full coverage of the outer divertor target from which the total integrated ion current is calculated.

4.10 Data processing to enable the combination and comparison of signals

Data signals are processed by filtering out ELMs before a smoothing function is applied and finally interpolated onto a time basis of one of the signals. The order of these processes are important to not introduce artefacts to the data unnecessarily.

The aim of this filtering is to separate inter-ELM and intra-ELM measurements so that the inter-ELM measurement can be used in the analysis. This filtering process must be done first to separate the signal because otherwise the next steps of smoothing or interpolation will make it harder to filter, with a much larger window required.

ELM filtering methods start by determining when and for what period the ELM occurs. For that we utilise the outer divertor BeII (527nm) signal which is measured on 10 spectrometer chords as part of the KS3 diagnostic. The signal does change inter-ELM but very obvious spikes are seen in H-mode due to ELMs and a peak detector can find the time of each ELM relatively easily.

Inter-ELM measurements of some variables are constant, but others, like upstream density, keep increasing until the next ELM crash. A standard method of ELM filtering is to look at the inter-ELM period between 70% and 90% of the time between two ELMs. This removes a large amount of useful data and effectively shifts the data to values found nearer the next ELM. The density never settles at a constant value in H-mode, but an inter-ELM density increase follows repeated drops in density intra-ELM. For signals that recover earlier after an ELM, lots of data is lost too. The inter-ELM signal will also be dependent on the ELM frequency, even if the inter-ELM signal is not supposed to be.

Filtering time points around the peak of the ELM within a fixed time window can preserve more data and is not dependent on the ELM frequency. Excluded times are marked intra-ELM 3.5ms before an ELM peak until 8.7ms after an ELM peak, which is long enough that all data is correctly filtered and recovered. A much longer time is needed after the ELM peak to recover. Signals such as the total divertor ion flux take longer to recover due to a drop below the inter-ELM value after the peak as the ion flux returns to an equilibrium after the intra-ELM peak. L-mode pulses are not filtered so all the data points are used.

Smoothing the inter-ELM data is required to make a model comparison for a few reasons. Signals aren't expected to be fully consistent as they are measured at different points in time and measurements are taken at very different spatial points which changes to upstream quantities may take some small time to reach a new detached equilibrium to measure instantly depending on the measurement. This and any noise due to the uncertainty will throw off a model comparison. Some signals will actually have a reason for applying more smoothing, such as the power from the NBI. As power is not instantly absorbed into the plasma and the transport from the core is not instantaneous, the data is smoothed over a time scale similar to the confinement time. The method of smoothing in most cases is taken to be a gaussian smoothing kernel with a fall off width σ_t. For every data point y_j up to N data points with time t_j, the smoothed point is calculated in equation 65. The smoothed value y_j^{smooth} is effectively a weighted value of data close in time to each t_j time point. This is adapted to cope with irregularly separated time points and large numbers of data points N.

$$y_j^{smooth} = \Sigma_{i=0}^{i=N} y_i exp(\frac{t_j - t_i}{\sigma_t})^2 \tag{65}$$

The smoothed time points are then interpolated onto a single time basis to make a model comparison. If unsmoothed and erratic data was used then this would introduce an interpolation error at this stage. The final stage is to split the data into relevant time groups but this will be explained individually in the next section, since there are different reasons to in each pulse.

The bolometer signal that is used for the calculation of P_{SOL} needed a larger than previously described ELM filtering window. The signal supplied is already pre-processed as smoothed over by 10 data points, which is very small on the time scale but not sufficiently well filtered to remove ELM emission. To counteract this, a larger region of filtering is applied to the data.

4.11 Discharge introduction

Different discharges were selected in this thesis work to narrow down the dependence of control parameter changes that influence the detachment front position in the DLS model. No discharges were explicitly run for the thesis objectives, instead various experiments that have control parameter variation were used in this analysis. Equation 37 shows that the total change in all 3 control parameters is important for the change in detachment front location, so pulses are selected on the basis that information is gained about at least one control parameter per pulse. This is a problem when not enough information is provided for a pulse such as where impurity concentration is not known, it would be impossible to perform a model comparison unless the data and model were a near perfect match. For most discharges used, the impurity concentration is not known and even for discharges with concentration measurements it not available for the entire pulse. The result is that simplified discharges were sought after, with regions that only 1 or 2 control parameters are seen to change at a time.

Another constraint on this analysis is that relevant data must also be available, primarily the camera must be set up with filters of D_γ and D_α to get the measurements. Faults can occur in certain diagnostics, for example interferometer channels are occasionally offline. These constraints limit the choice of pulses that can be selected.

The next sections go into detail about each individual pulse that was analysed, explaining how they can specifically be made use of and qualitatively why. Quantitative analysis is done in the next chapter.

4.11.1 JET pulse number 89241

This pulse is useful because it has measurements of the nitrogen concentration which are valid for a short period of time. The pulse has been previously analysed intra-ELM and inter-ELM with different method for tracking the detachment front by Field et al. [2017]. While the changes in control variables are small, control parameters in the model are raised to exponents, so large changes in detachment front position still need to be considered in this analysis.

The general pulse overview shown in figure 25 shows the discharge information including rollover of the total ion flux at $\sim 50s$ (figure 25 (b)). The pulse enters H-mode at $\sim$ 48.5s at the same time nitrogen is started to be seeded in the divertor with a linearly increasing ramp. Another benefit of this pulse is that there is a slow ramp up in the level of detachment, as the detachment front moves from the target to the X-point over the course of 2-3 seconds. This is a slower movement of the detachment front position than other pulses analysed.

4.11.2 JET pulse number 94763

The L-mode pulse 94763 is particularly interesting as it is not seeded with nitrogen, has a time section with constant P_{SOL} and has a upstream density increase followed by decrease. As will be discussed later, we can assume little to no variation in divertor impurity concentration. The ion flux mirrors the density variation, but it rolls over earlier at 49s before a measurable movement of the detachment front off of the target. Ion flux starts to increase again at $\sim 51.7s$ when the density starts to decrease. Here it appears obvious that the main control parameter is the density changes with a very small P_{SOL} change after $\sim 51.7s$.

4.11.3 JET pulse number 89749

Pulse 89749 has significant P_{SOL} variation compared to other pulses. The detachment front movement appears at first to be dominated by changes in P_{SOL}, particularly towards the end of the pulse. Large increases and decreases in P_{SOL} appear to correspond to detachment front movement, which makes this pulse ideal for understanding the response of detachment front movement to changes in P_{SOL}.

This pulse enters H-mode at 48.6s and is seeded with nitrogen at a constant rate, starting at 48.5s. The information in figure 24 shows that the detachment front position is moves towards and away from the X-point, mostly located closer to the X-point. The movement of the detachment front is mirrored by the total ion flux which first rolls over at 49.2s then after 2 more periods of re-attachment it rolls over at 50.5s and again between $51.2-52$s. P_{SOL} changes seem to align with the detachment front movement after 50s but not before.

4.11.4 JET pulse number 89751

This pulse is used to compare different potential measures of nitrogen concentration. Unfortunately direct nitrogen concentration measurements are not available for this pulse but other proxies are tested. The detachment front movement appears to change in response to nitrogen seeding rate changes throughout this pulse.

The pulse enters H-mode at 48.5s at the same time as increases to the nitrogen seeding rate. The ion flux rolls over for the first time at $\sim$ 49.7s then again at $\sim$ 50.5s and $\sim$ 51.5s due to periods of re-attachment.

4.11.5 Overview Plots

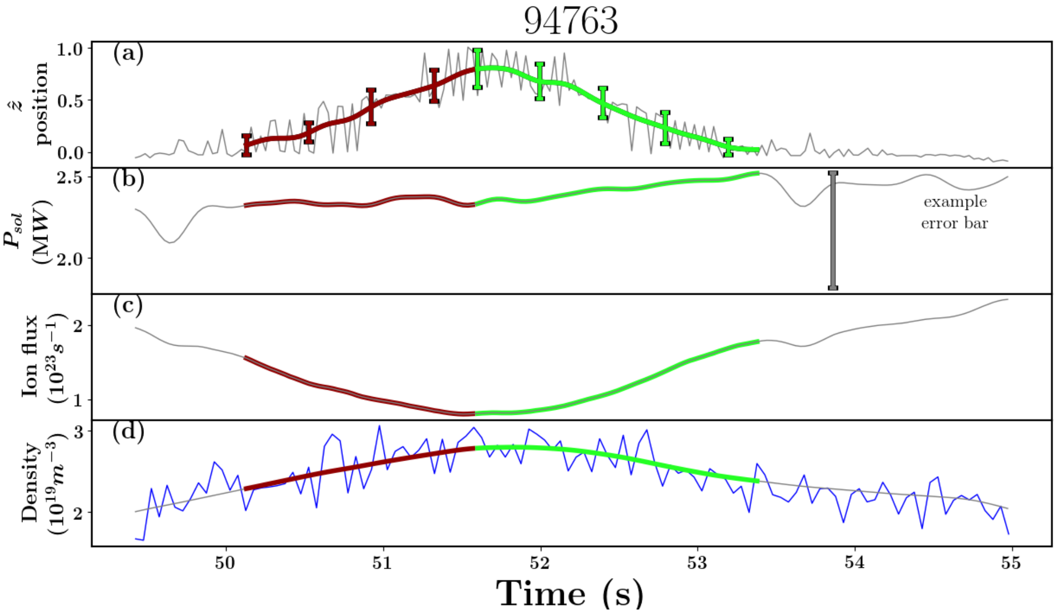

Figure 23: General plots for the pulse 94763

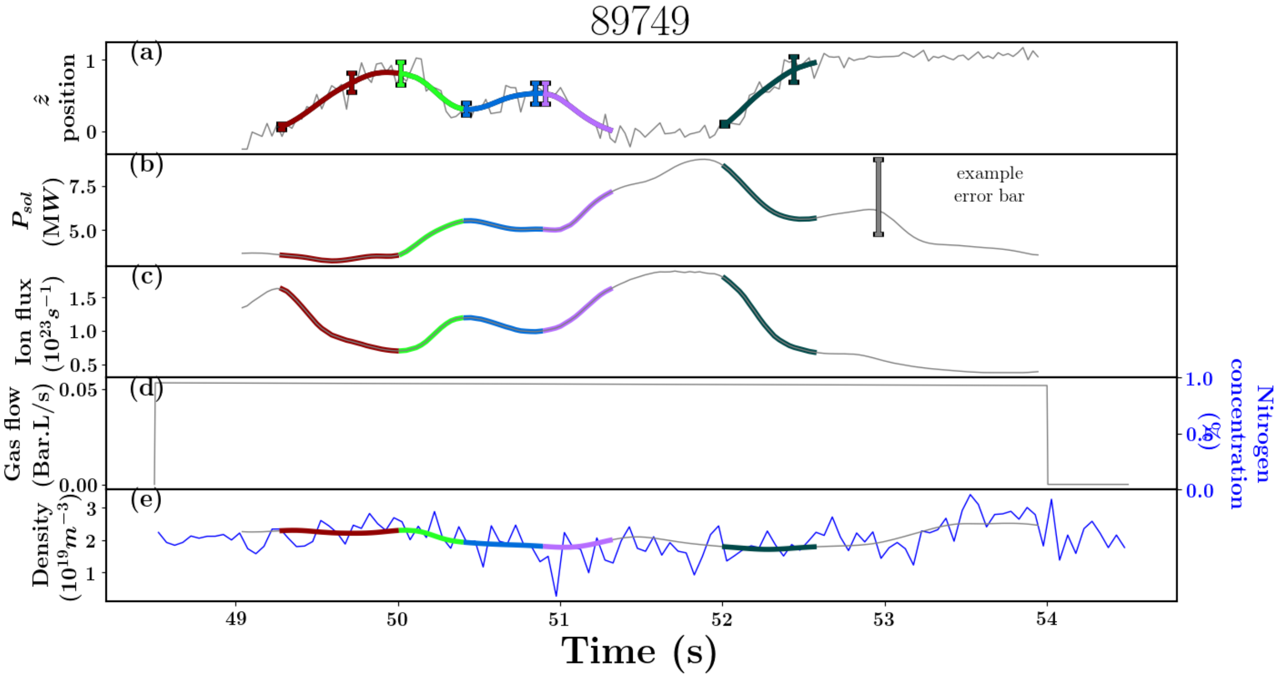

Figure 24: General plots for the pulse 89749

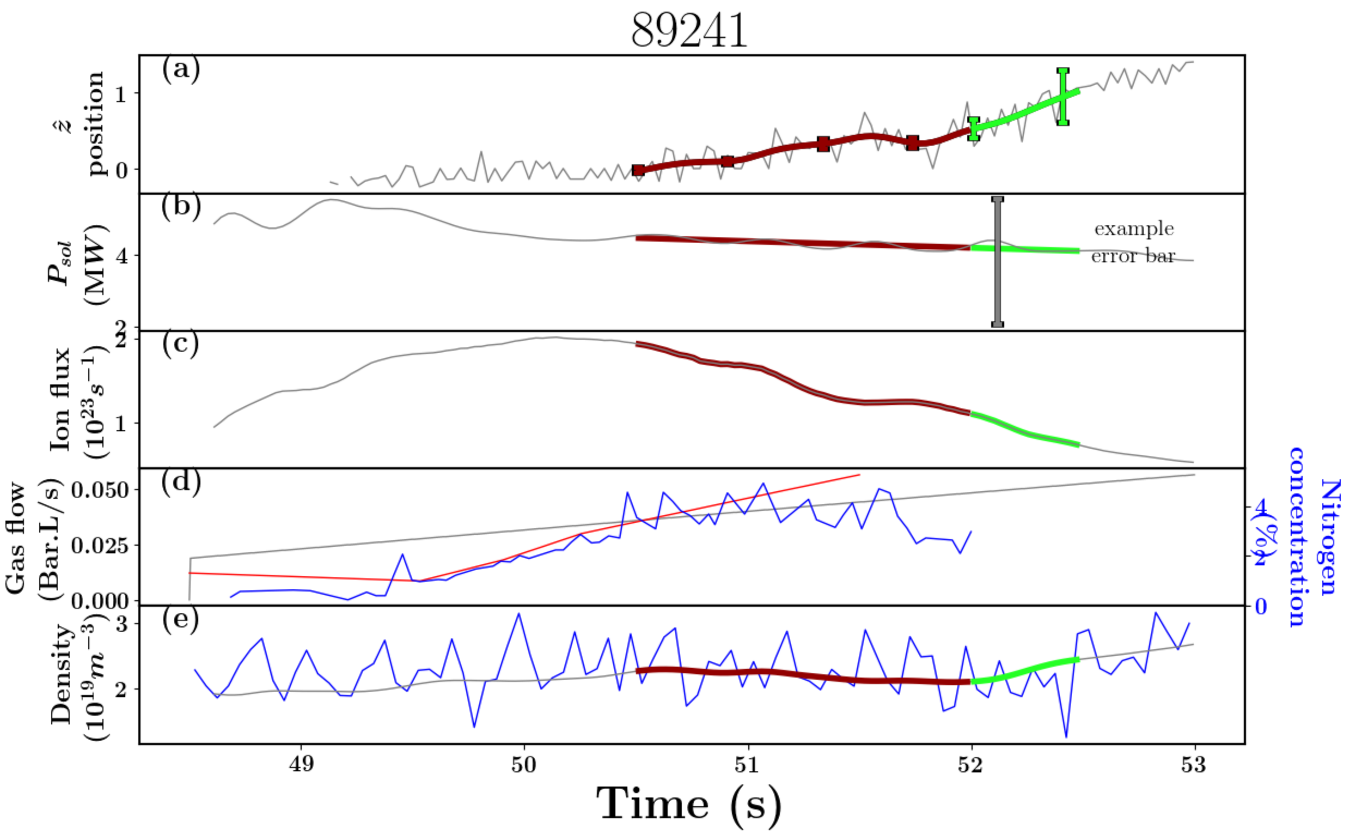

Figure 25: General plots for the pulse 89241

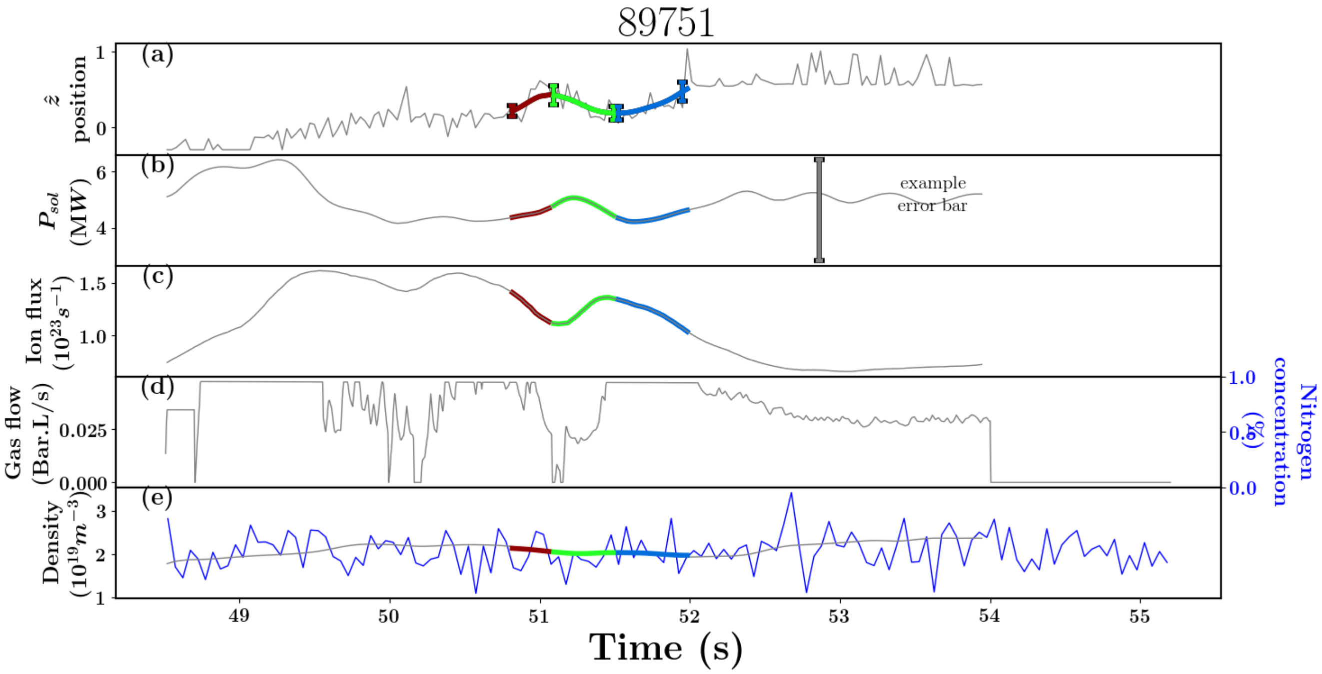

Figure 26: General plots for the pulse 89751

4.12 Investigating the detachment front location dependence on impurity concentration

As impurity concentration changes are difficult to measure, some different approximations are discussed in this section based on the assumption that pulse 89751 is controlled by the impurity concentration. As stated in section 4.11.4 and shown in figure 26, the P_{SOL} and n_u dependence are small over the pulse and on their own would not explain the measured detachment front location changes. The pulse is nitrogen seeded, so impurity concentration changes are likely to be dominated by nitrogen concentration changes. The aim of this section is to compare the detachment front position qualitatively to some of the control parameter changes.

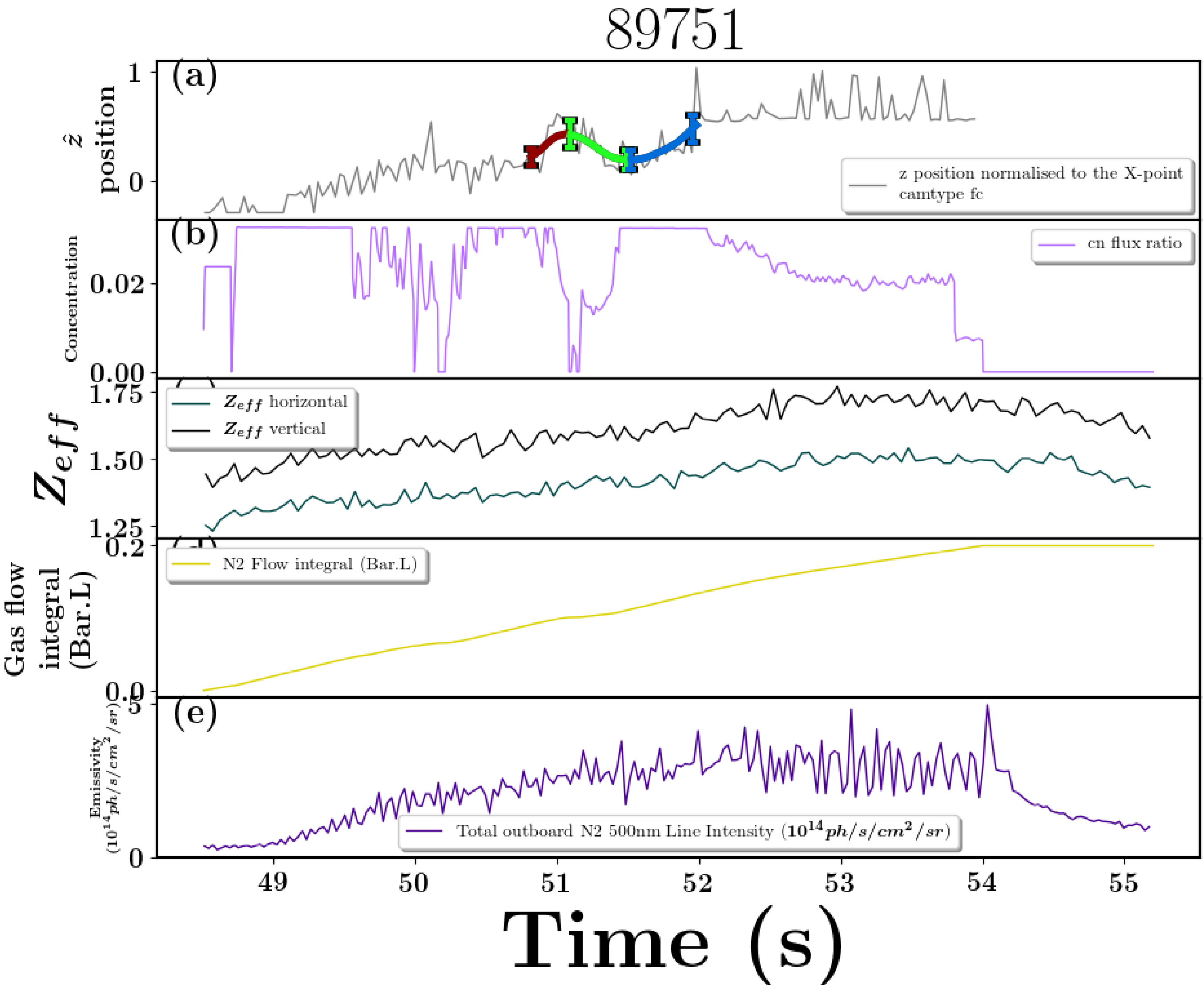

Figure 27: Impurity relevant plots for the pulse 89751

The technique for estimating the impurity concentration from the ratio of seeding rates described in section 4.8.2 appears unsuitable for measuring the concentration. This is because changing the seeding does appear to induce a response in the detachment front position. Even though the Nitrogen seeding seems to introduce changes when it is turned on and off, the total impurity concentration would have to be a signal that at the same concentration value, the same detachment front position is reproduced with no hysteresis. This is clearly not the case comparing figure 27(a) and 27(b). There is no account for the total build-up of nitrogen ions in the divertor, but an alternative is shown in figure 27 (d), where the cumulative nitrogen seeding rate is found from the start of the pulse. This signal has the opposite problem that there is no inclusion of a decrease in nitrogen density in the divertor, which is not realistic since impurities would be expected to not stay in the divertor volume permanently. An ideal signal would have to model the loss of impurities, which is not simple to include. The fact that the flux ratio does not respond like a control parameter does not mean it is useless. Since there is a response of the detachment front, it can, of course, be used for feedback control for this reason. More advanced models would be needed to find something closer to the impurity concentration, for example, modelling impurity transport[46].

Z_{eff} measurements from the horizontal and vertical chords appear to not respond to changes in the seeding rate. Figure 27 (c) shows that changes in Z_{eff} are consistent in shape and close in magnitude for the horizontal and vertical chord measurements but they are not appropriate for using as a divertor concentration proxy in the analysis in this thesis. If the penetration of impurities into the core was fast enough and there was no impurity compression in the divertor then core impurity concentration would likely change and Z_{eff} would change. The Z_{eff} is steadily increasing throughout the pulse as does the detachment front location, but changes in Z_{eff} are not appropriate to determine the finer details of the detachment front position movement.

The other signal used as a nitrogen concentration proxy in Field et al. [2017] is the total NII emission in the divertor. The assumption requires that the upstream density be constant, and this was justified for pulse 89241. The variation in upstream density seems to be constant for this pulse as shown in figure 26, and has a lower variation than in 89241 as shown in figure 25. However the signal in figure 27 (e) also does not respond to changes in the nitrogen seeding rate either.

The lack of concentration information from the above techniques means that the only possible signal to use is the spectroscopy derived nitrogen concentration from Henderson et al. [2019]. The availability of this information is intermittent depending on the ELM frequency and spectrometer settings, so the alternative is to base this analysis on portions of data that we can assume constant nitrogen concentration and using this to infer impurity concentration based on the model and seeing if the concentration change predicted is reasonable or expected. For the sections where impurity concentration can be considered constant, the other two parameters can be analysed quantitatively.

5 Detachment front Location control and sensitivity

In this chapter, the detachment front location measurements are confirmed to accurately measure the state of detachment before comparing to the DLS model. To increase confidence in the normalised position $\hat{z}$ of the inferred $\frac{D_\gamma}{D_\alpha}$ front edge, which is taken to be the detachment front position in this study, a comparison is made to the total outer target ion current in section 5.1.

The effect of changes in n_u and P_{SOL} on the detachment front are evaluated individually in section 5.2.2. By assuming f_z to be constant in 94763 where there is no impurity seeding, a measured detachment location sensitivity to changes in n_u and P_{SOL} is found in section 5.3 in the form of control parameter's exponent. Both this adjusted and DLS model sensitivity can be applied to other pulses to infer the changes in f_z that would have to occur to match the measured sensitivity to the control parameters, which is shown in section 5.4. The possibility that f_z changes this way are discussed considering nitrogen seeding rates used in the experiments and changes in Z_{eff}.

5.1 The relationship between detachment front position and target ion flux

To rely on the measured detachment front position for model comparison, testing against other measures of detachment is an important check. The comparison of $\hat{z}$ position based on the inferred $\frac{D_\gamma}{D_\alpha}$ front edge to the total outer target ion flux is made in this section. Ion flux measurements have been used to determine the detachment onset and the drop in target current during detachment[52] [53]. We make a comparison of the target ion current to the $\frac{D_\gamma}{D_\alpha}$ measurements to check where there is agreement that drops in ion target current are correlated with moving the detachment front position towards the X-point, and if rollover is consistent with moving the detachment front location off the target. After an initial rise in target ion current during the attached, high-recycling phase, the detachment threshold is passed and target ion current reaches a peak value and then decreases as a 'roll-over' in the transition to a detached regime, so the range of ion target current measurements are only a valid measure of detachment after rollover. The detachment front position is only a valid measurement when positioned away from the target but before reaching the X-point in the DLS model.

The relationship between $\frac{D_\gamma}{D_\alpha}$ front edge position and the total ion flux to the outer divertor shown in figure 28 gives confidence that the $\frac{D_\gamma}{D_\alpha}$ front edge position is following detachment progress. The relationship shown in figure 28 appears to be approximately linear between $\frac{D_\gamma}{D_\alpha}$ front edge position and the total ion flux to the outer divertor while the $\frac{D_\gamma}{D_\alpha}$ front edge position is between the target and X-point. All pulses appear to share both the approximately linear relationship with similar correlation and have similar absolute value of the total outer divertor ion flux that the $\frac{D_\gamma}{D_\alpha}$ front edge position starts to move off the target. There is no clear reason why the loss of total ion current from the outer divertor should be approximately linearly dependent on $\hat{z}$.

The DLS model assumes that changes to the detachment front position are controlled by 3 control parameters, with target ion flux considered negligible in the DLS model at and after detachment. However figure 28 implies that target ion flux would also respond to the 3 control parameters. The pulses used in figure 28 include H-mode pulses (89241, 89749 and 89751) with significant differences in nitrogen seeding rate, P_{SOL} and n_u; and an L-mode case (94763) with much lower P_{SOL} and no N_2-seeding. The $\frac{D_\gamma}{D_\alpha}$ front edge position is predicted to be controlled by various combinations of all 3 DLS control parameters in the pulses shown in figure 28, which implies that target ion flux also has a similar relationship. Detachment most likely driven by: nitrogen concentration changes in 89751, by P_{SOL} changes in 89749 and by n_u changes in 94763, yet all show a similar relationship in figure 28. To include and explain the target ion flux in the context of the DLS model, the balance between heat fluxes from upstream of the detachment front to radiation throughout the thermal front with assumption of no heat flux left over at the target would have to be revised.

One potential connection between target ion flux and detachment front location can be made by considering the changes in volume of the low-temperature detached region while assuming a constant ionisation source. Thus as the detached region expands the volume of a recombining region could be expanding and increasing loss of current at the target. We assume that the ionisation source in the thermal front is, at most constant during the detachment movement. But that ion source could be dropping due to fewer neutrals reaching there and/or reduced volume of ionisation.

The reader may have noticed that some of the measurements of $\hat{z}$ shown in figure 28 are ‘below’ where the target is defined. The ‘target’ location is defined as when z is above the actual divertor surface, which results in $\hat{z}$ at the actual surface being below 0. Alignment of the camera inversion data used to obtain the D_γ & D_α data are very noisy at the edge of the grid at the surface and toroidal assumptions breakdown due to angled divertor tiles. The regions of negative $\hat{z}$ occur during the attached phases of the JET pulses and the time when rollover of total target ion current occurs is prior to when there is measurable movement of the detachment front edge off of the target. The DLS model has been modified in this thesis to not rely heavily on the front position and magnetic field at the target z_t and B_t but $\hat{z}$ uses z_t to compare detachment front positions in the DLS model

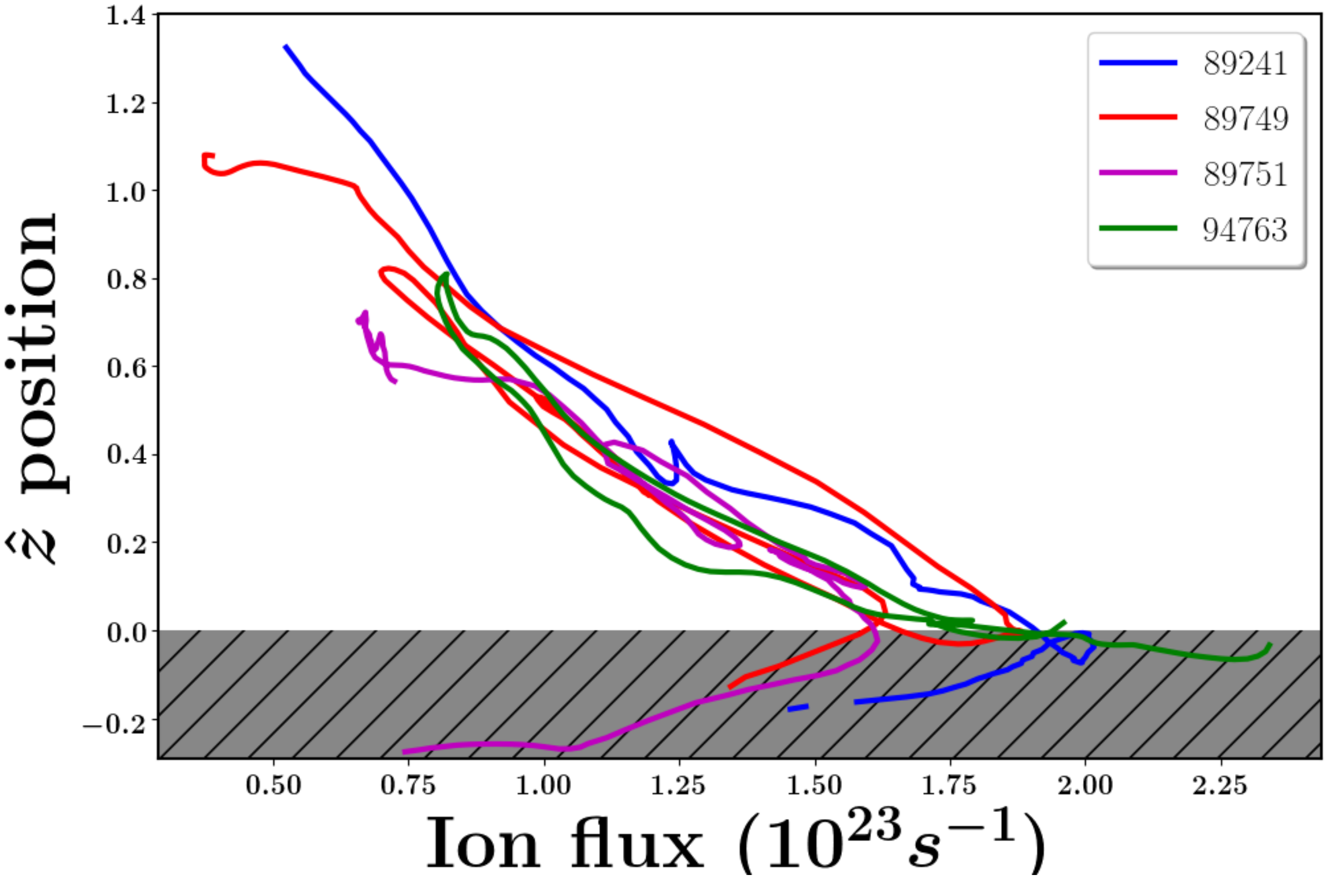

Figure 28: Total ion flux correlation to the detachment front position

between different pulses.

5.2 Relationship between control parameters and detachment front location

This section compares experimental measurements to the predictions of the DLS model. Comparisons of the DLS prediction of $\hat{z}$ with experiment are first made assuming that the impurity concentration is constant throughout the time section analysed as n_u and/or P_{SOL} are varied for each section of each pulse (section 5.2.1 and 5.2.2). The second step (section 5.3) is using parts of pulse 94763 where we are fairly confident that f_z is not varying substantially to compare changes of n_u to the measured and DLS model detachment front location. Similarly a comparison can be made in pulse 89749 to compare changes of P_{SOL} to the measured and DLS model predictions of the detachment front location. The comparisons are made to highlight quantitative differences between the measured and DLS detachment front location sensitivity.

5.2.1 Choosing normalisation points for model comparisons

To make a prediction of the $\hat{z}$ position from changes in n_u and/or P_{SOL} with the DLS model, at least one time point for each pulse needs to be used to normalise all values to in the rest of the pulse. Equation 36 has point (1) to be normalised at, but because $\frac{\left(\frac{n_u f_z^{1/2}}{P_{SOL}^{5/7}}\right)_2}{\left(\frac{n_u f_z^{1/2}}{P_{SOL}^{5/7}}\right)_1}$ can have up to 3 control variables changing over a pulse, a set of P_{SOL}, n_u, f_z and the detachment front position must be defined at a chosen time (1) during the pulse. This is essential because any combinations of P_{SOL}, n_u, f_z leading to the same 'combined' control variable predicts the same detachment front position.

By leaving equation 36 generalised and choosing any particular time point as (1), predictions can be made in a per-time region manner. The advantage of this is that if the model does not match the data in any particular region then it is easier to pin down which control parameter caused the discrepancy. Time regions are separated where the rate of change in control parameters or the measured detachment front location change significantly. This allows detachment front movement to be attributed to individual control parameters separately. The normalisation time point (1) is taken at the start of each time section so that the difference between the DLS model and the data can be seen as each time section progresses.

5.2.2 The DLS model sensitivity comparison

This section steps through some simple comparisons of the measured data to the DLS model predictions, identifying that some of the measurements of the variations of $\hat{z}$ with n_u and P_{SOL} seem to be at odds with the DLS model predictions. The flux tube dependent parameters for making DLS predictions are assumed constant over the sections of the pulse of interest are shown in table 1. $\hat{z}$ can be found by solving equation 36 based on changes in control parameters n_u and P_{SOL} assuming no changes in f_z. Time sections that are more likely to have negligible f_z changes are highlighted below. Based on the above assumptions for the flux tube characteristics for the various pulses (table 1) the DLS model predictions of $\hat{z}$ are made and plotted (red lines) in figures 29 and 30. Note that $\hat{z}$ predictions are made based on only varying 1 single control parameter, either n_u or P_{SOL}, so the time ranges that are shown to compare sensitivity changes must have low changes in the other control parameter (P_{SOL} or n_u).

A general observation of these DLS predictions shown in figures 29 and 30 is the approximately linear relationship between $\hat{z}$ and either P_{SOL} or n_u. The reason for this is explained with equation 42 which for changes in P_{SOL}, $\hat{z}$ position changes are proportional to $C - \hat{z} \propto (P_{SOL})^{5/2}$ (where C

Pulse	Bx	Bt	zx	zt	L
89749	2.42	2.36	6.84	1.37	31.1
89241	2.41	2.36	5.79	1.37	29.11
94763	2.75	2.69	4.81	1.37	26.47

Table 1: The key magnetic configuration parameters for model comparisons.

is a large value) or for changes in density $C - \hat{z} \propto \frac{1}{n_u^{7/2}}$. The shape of the P_{SOL} dependent parts are linear under these assumptions, while $\hat{z} << C = \frac{L+z_\times}{2z_\times}$ the n_u dependence is still curved, but over the range $0 < \hat{z} < 1$ the slope $\frac{d\hat{z}}{dn_u}$ does not change significantly.

The evidence for reducing detachment front location sensitivity for changes in n_u (exponent for n_u in equation 36) is strongest when P_{SOL} is kept constant during the first time section of 94763 (brown trace). Figure 29 shows that over the entire pulse 94763 the n_u dependence on the detachment front location is close to a reversible process (no hysteresis) during the rise then fall of n_u. The reversibility of the detachment front movement is also evidence that the impurity concentration does not have a large effect on the detachment front location in this pulse; one would not expect the concentration to rise and fall in just the right way to return the detachment front to its starting position. In other words neither the impurity concentration nor P_{SOL} vary much during the period highlighted.

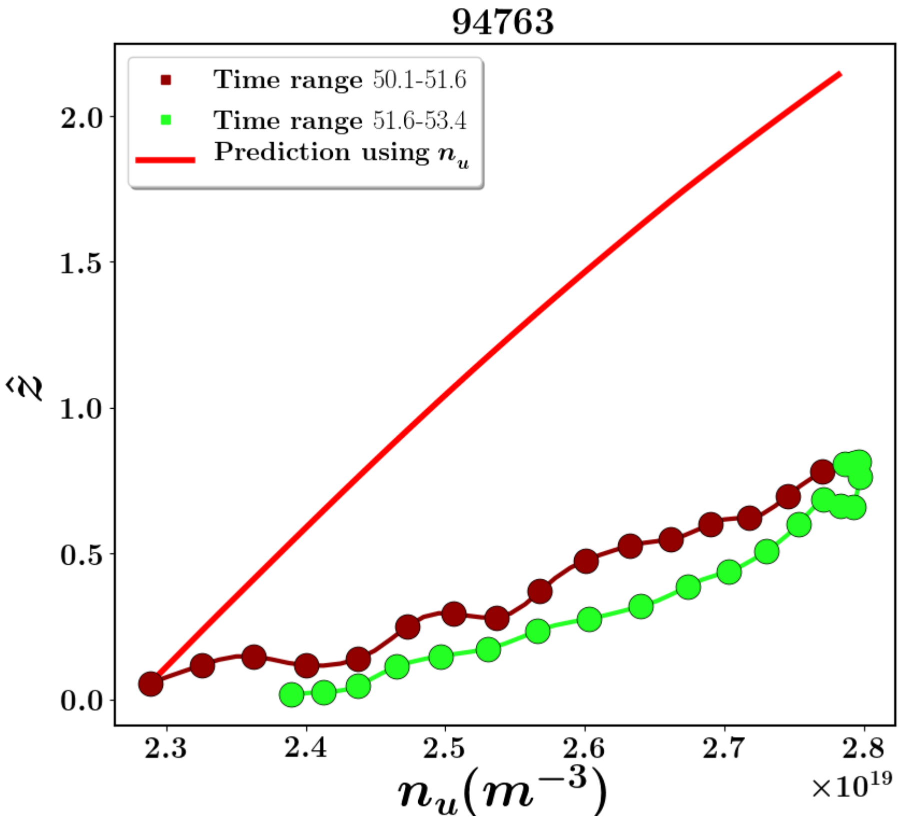

Figure 29: n_u vs $\hat{z}$ position of pulse 94763 for 2 time ranges highlighted in figure 23. The DLS model prediction of $\hat{z}$ from changes in n_u (P_{SOL}, f_z constant) is plotted in red.

The detachment front position is less sensitive to changes in n_u than the DLS model predicts, as shown in figure 29 because the DLS predictions slope ($d\hat{z}/dn_u$) of $\hat{z}$ vs n_u is much sharper in the DLS model predictions than the measured detachment front position on n_u. The small P_{SOL} in the second section (green section) is predicted to have a contribution to the $\hat{z}$ changes, however a strong effect on the measured $\hat{z}$ is not seen in the small difference in the slope of figure 29 between the first and second sections. The reduced detachment front location movement from changes in P_{SOL} suggests that the measured detachment sensitivity to P_{SOL} may also be reduced compared to the DLS model prediction.

Further evidence for reducing the sensitivity of the detachment front location to P_{SOL} changes is shown in figure 30 for pulse 89749 where there are large variations in P_{SOL}. Other than the first time period of the pulse, there is a correlation between P_{SOL} and detachment front position. For most time sections in the pulse, the value of $d\hat{z}/dP_{SOL}$ is the same and lower than predicted by the DLS model. As 89749 is seeded with nitrogen at a constant rate, it is possible that concentration that the divertor nitrogen concentration, f_z, rises fast during the first time period of 89749. As will be shown in Section 5.3, lowering the exponents for both n_u and P_{SOL} (lowering the sensitivity of $\hat{z}$ to those variables) seems warranted from figures 29 and 30.

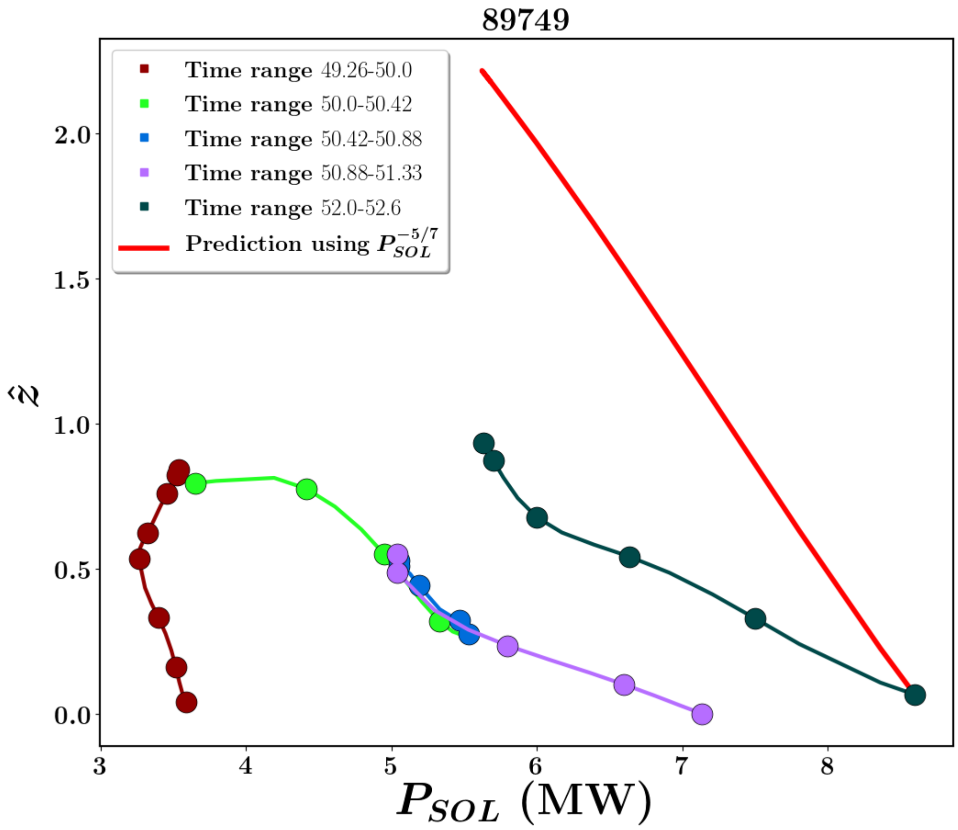

Figure 30: P_{SOL} vs z position of pulse 89749 for 5 time ranges (colours corresponding to figure 24). The DLS model prediction of $\hat{z}$ from changes in P_{SOL} (n_u, f_z constant) is plotted in red.

5.3 Adjustments to the DLS model sensitivity to n_u and P_{SOL}

The evidence in section 5.2 shows in a qualitative way that for multiple pulses there are regions in time which show that the DLS model sensitivity might need an adjustment. In the following, adjustments are made to the sensitivity for different control variables and then model predictions are re-compared to data. Note that as said before and discussed in section 6, there are good reasons to suggest that the DLS model predictions are 'off'.

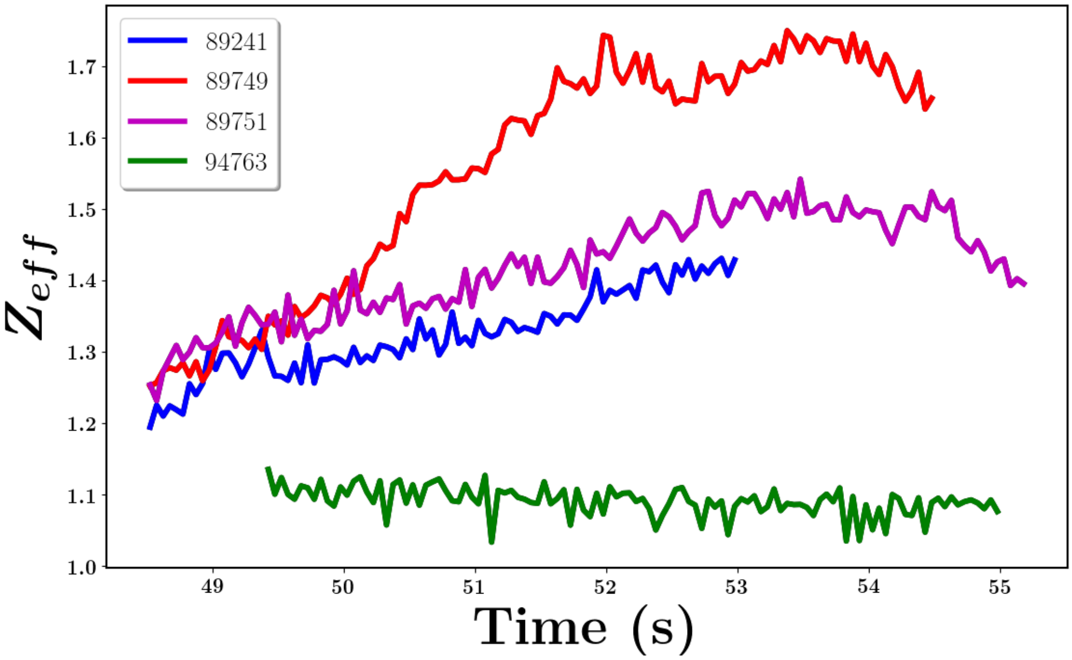

Figure 31: Z_{eff} over time for 4 pulses.

Allowing the model exponents to vary is a clear way to change the sensitivity. The exponents in equation 38 or 43 show the generalised partial derivative for either P_{SOL}, n_u or f_z. The only way to change this sensitivity throughout the entire X-point to target region is to change the exponent from $P_{SOL}^{-5/7}$ and n_u to $P_{SOL}^{X_P}$ and $n_u^{X_n}$.

To make an estimate of adjusted exponents for n_u and P_{SOL}, assumptions about the impurity concentration must be made. There is not enough data from the measured nitrogen concentration available for 89241 to get a good fit for all 3 exponents together. The nitrogen concentration measurement in 89241 appears constant in the time region it overlaps the detachment front position data, but after normalisation, $\frac{(f_z)_2}{(f_z)_1}$ noise is significant, so this pulse cannot be used as a starting point.

Finding the DLS model exponents from the measured detachment front location in 94763 was thus considered the best for determining the modified sensitivity, since it is likely to have a constant impurity concentration. Following that are comparisons of the modified DLS sensitivity predictions of f_z for other pulses and reason whether that f_z prediction is reasonable.

Another indication of the impurity concentration during 94763 is approximately constant is that the core plasma Z_{eff} in L-mode is approximately constant, varying by of order 5% (see Figure 31). Z_{eff} is not a sufficient indicator of impurity concentration in the divertor since the two indicators of impurity levels are not always related. However Z_{eff} does increase more for the higher seeded pulses, with barely any change for 94763.

94763 has been split into 2 sections to deal with the increasing and decreasing detachment front position separately as well as the different role of control parameters in the two time periods; both having significant (dominant) variations in n_u. The first section has no change in P_{SOL} and the second section has a small P_{SOL} change. We will treat the two time periods separately for an analytical comparison and treat them together with a numerical comparison.

For only density changes in section 1 of 94763, it is enough to solve for the exponent analytically. By rearranging equation 36 assuming P_{SOL} and f_z do not vary $\frac{\left(\frac{f_z^{1/2}}{P_{SOL}^{5/7}}\right)_2}{\left(\frac{f_z^{1/2}}{P_{SOL}^{5/7}}\right)_1} = 1$ results in equation 66 with exponent for n_u (X_n), having taken the logs of the equation. The exponent found is $X_n = 0.35 \pm 0.03$.

$$X_n = Ln\left(\frac{B_2}{B_1}\frac{\left[\frac{1-\hat{z_2}}{3}\left(1+\left|\frac{B_2}{B_\times}\right|+\left|\frac{B_2}{B_\times}\right|^2\right)+\frac{L-z_\times}{2z_\times}\right]^{-2/7}}{\left[\frac{1-\hat{z_1}}{3}\left(1+\left|\frac{B_1}{B_\times}\right|+\left|\frac{B_1}{B_\times}\right|^2\right)+\frac{L-z_\times}{2z_\times}\right]^{-2/7}}\right)\frac{1}{Ln\left[\frac{(n_u)_2}{(n_u)_1}\right]} \tag{66}$$

In order to fit the data for both time periods, the exponent for P_{SOL} (X_p) must also be changed. The exponent can be fit using section 2 of 94763, since there is a small P_{SOL} change not seen in the first section. With X_n known from the first fit, X_p can be calculated from equation 67. The alternative to fit both exponents simultaneously can't be done in an analytic way, but solving for both exponents can be done numerically using this equation. The exponent found is $X_p = -0.27 \pm 0.06$. The result is plotted in figure 32 for both time periods. The value of f_z does not significantly change during the two time periods as expected given the assumption that f_z is constant.

The estimated uncertainty of our prediction for the exponents in each time section in 94763 can be found analytically, however to capture more components of the uncertainty (such as variations to the normalisation point (1)), the exponents were calculated for both the combined 94763 time periods using a Bayesian Markov chain Monte Carlo method. The uncertainty of the exponents is propagated through later to $\frac{(f_z)_2}{(f_z)_1}$ from equation 68 where it is plotted in figures 32, 33, 34, 35, 36

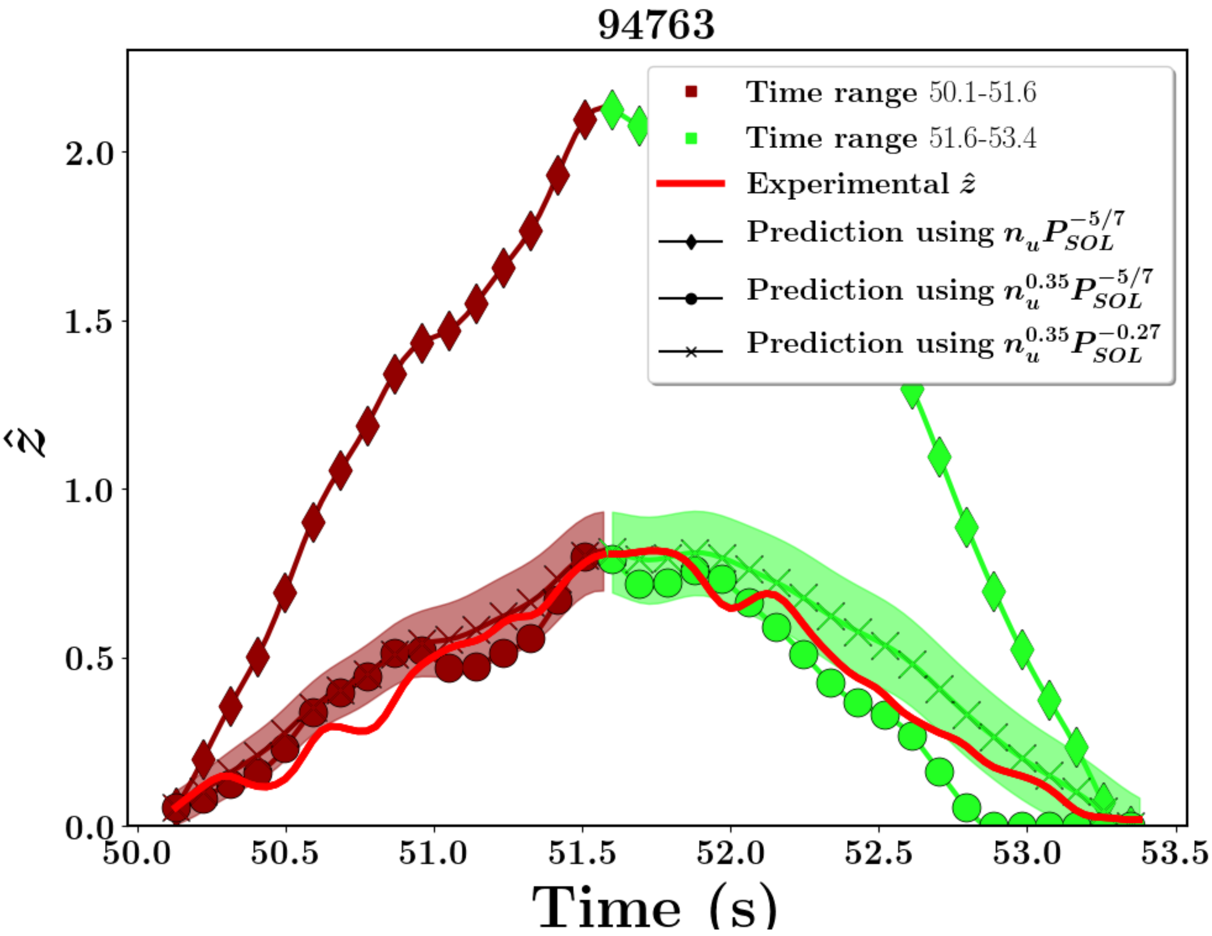

Figure 32: A comparison of predicted $\hat{z}$ position calculated using different combinations of exponents for the control parameters $n_u \& P_{SOL}$ to make predictions of $\hat{z}$. The prediction is made based on the starting position and control parameter at the start of each coloured section to predict every position in that section. The experimental $\hat{z}$ position is also plotted for comparison. Note that f_i is held constant in the $\hat{z}$ prediction.

and 37.

$$X_p = Ln\left(\left[\frac{(n_u)_1}{(n_u)_2}\right]^{X_n}\frac{B_2}{B_1}\frac{\left[\frac{1-\hat{z}_2}{3}\left(1+\left|\frac{B_2}{B_\times}\right|+\left|\frac{B_2}{B_\times}\right|^2\right)+\frac{L-z_\times}{2z_\times}\right]^{-2/7}}{\left[\frac{1-\hat{z}_1}{3}\left(1+\left|\frac{B_1}{B_\times}\right|+\left|\frac{B_1}{B_\times}\right|^2\right)+\frac{L-z_\times}{2z_\times}\right]^{-2/7}}\right)\frac{1}{Ln\left[\frac{(P_{SOL})_2}{(P_{SOL})_1}\right]} \tag{67}$$

Using equation 68, the relative impurity concentration change can be inferred to compare cases of the original DLS model control parameter exponents and the case where model exponents are derived from the JET experimental data. Figure 33 shows how the impurity concentration change in 94763 is enforced to not change throughout the pulse with the measured exponents. Without changing the exponents, there would need to be a significant (20%) drop in the first section and then, in the second section, an increase in f_z similar to the drop in the 1st section. In terms of magnitude,

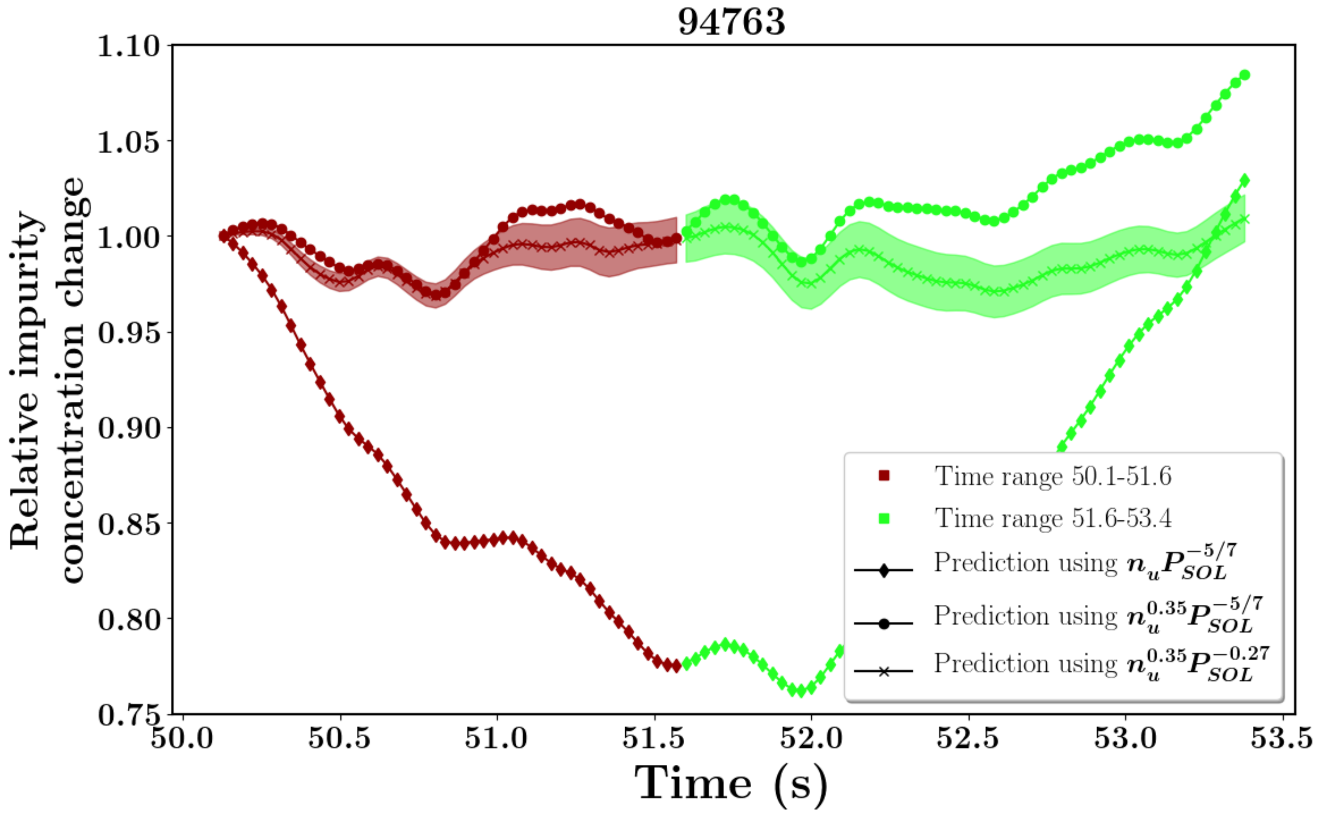

Figure 33: The predicted impurity concentration calculated using equation 68. The prediction is made based on the starting position and control parameter at a single time at 50.0s

this could be believable, since the impurity concentration would be low in this pulse, a relative change of 80% is not unreasonable. However the change in shape is what seems less likely, as it would have to be a reversible change to impurity concentration for the original exponents to match. Figure 33 shows that decreasing the exponent X_n has the effect of flattening the change in impurity concentration for section 1. To keep the impurity concentration constant in section 2 an increase in impurity concentration to match the model with the original P_{SOL} exponent $X_p = -5/7$ is required. There was no suitable pulse found to isolate the effect of X_p without also changing the impurity concentration or density. However, the evidence when applying this new exponent to 89749 where P_{SOL} appears dominant for at least a few parts of the pulse will be considered later. After making the change to X_p the constant impurity concentration has been enforced over the entire pulse 94763.

$$\frac{\left(f_z^{1/2}\right)_2}{\left(f_z^{1/2}\right)_1} = \frac{\left(\frac{n_u^{X_n}}{P_{SOL}^{X_p}}\right)_1}{\left(\frac{n_u^{X_n}}{P_{SOL}^{X_p}}\right)_2} \frac{B_2}{B_1} \frac{\left[\frac{1-\hat{z}_2}{3}\left(1+\left|\frac{B_2}{B_\times}\right|+\left|\frac{B_2}{B_\times}\right|^2\right)+\frac{L-z_\times}{2z_\times}\right]^{-2/7}}{\left[\frac{1-\hat{z}_1}{3}\left(1+\left|\frac{B_1}{B_\times}\right|+\left|\frac{B_1}{B_\times}\right|^2\right)+\frac{L-z_\times}{2z_\times}\right]^{-2/7}} \tag{68}$$

Another way of looking at the effect of exponent changes it to calculate the model prediction of the $\hat{z}$ position under different cases of exponent choices, assuming again that the impurity concentration is constant. Figure 32 shows that the original exponents for n_u would have predicted a much larger change in z position but simply X_n fits the data much better. The case in figure 32 changing the n_u exponent but without changing the P_{SOL} exponent predicts a much more attached divertor than observed.

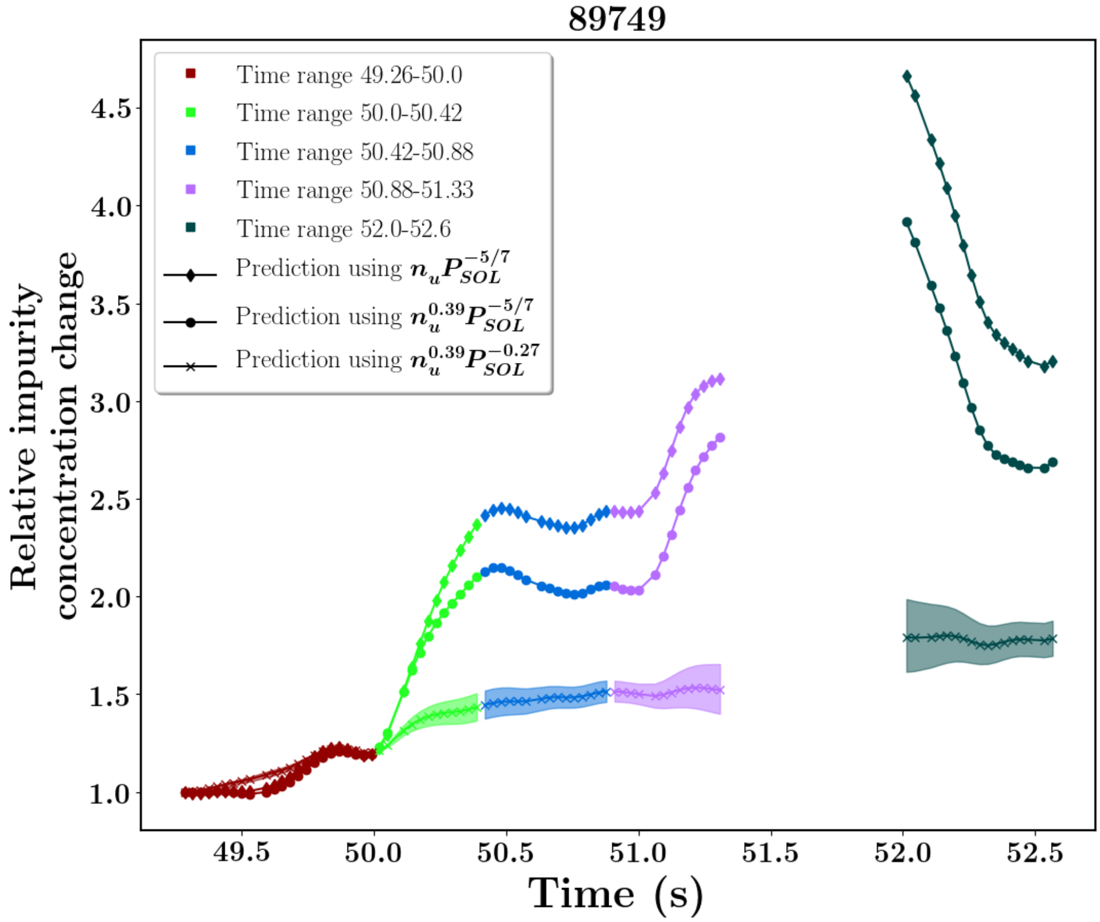

Figure 34: The predicted impurity concentration calculated using equation 68. The prediction is made based on the starting position and control parameter at a single time at 50.0s

5.4 Comparing the impact of adjusted sensitivities on inferred impurity concentration changes for H-mode pulses

Comparing the original and newly calculated exponents on other pulses than 94763 allows impurity concentration changes to be calculated to see if the new exponents make sense. Assuming the exponents derived from 94763 (L-mode), they are applied to the two H-mode cases. In pulses 89241 and 89749, the impurity concentration should not be considered constant throughout, so repeating the exact analysis utilised in pulse 94763 (constant f_z), is not possible.

The data from pulse 89749 is consistent with the value of the exponent for P_{SOL} derived from 94763 data based on the predicted changes in f_z during the pulse. The experimentally determined X_n and X_p are applied to 89749 as shown in figure 34 and 35 to compare the original and new predictions of f_z.

During the first 2 highlighted sections of figure 35 (brown and green), any combination of exponent values imply that the assumption of a constant f_z is incorrect; it needs to increase in those two time periods. The prediction of $\hat{z}$ is closer to experiment in the blue section. In the last two sections (purple and black) it appears that under the assumption of constant f_z during those time periods, assuming the exponents inferred from pulse 94763, leads to a good match to the measured $\hat{z}$. The response of detachment front location movement is clearly dominated by changes in P_{SOL}, since changes to the density exponent barely changes the prediction.

The assessment of exponent changes in figure 35 is more clear in figure 34 where the inferred f_z variation in time for the entire pulse is plotted. Figure 24 shows that the seeding rate is constant for this pulse and begins at 48.5s. It is likely that at the start of the pulse, larger changes in impurity concentration are made before levelling out at around 50.5s. Once an equilibrium is found between the seeding rate and losses of impurities to either the core or walls, then a flattening of impurity concentration should be seen in the pulse. This is seen with the newly derived exponents in figure 34, which supports the case for the alterations to X_n and X_p (mostly X_p). By using the X_P for section 5 of 89749, the impurity concentration inferred is low, which was expected. Finding constant impurity concentration later in the pulse is supported by low Z_{eff} changes shown in figure 31 and the constant nitrogen seeding rate could mean an equilibrium of nitrogen in the divertor was reached.

Another argument for the validity of the exponents derived from pulse 94763 is that with the original DLS model exponents, f_z increases sharply in the green section, drops in the blue section and then sharply increases again during the purple-marked periods of the pulse. This seems unlikely given the steady impurity seeding. In contrast, for the case of applying the exponents derived from pulse 94769 to 89749, the impurity concentration increases smoothly.

Consistency between the X_P in 94763 and 89749 link together L-mode and H-mode cases. When considered inter-ELM, changes in the DLS model have no significant assumptions that would separate the L-mode and H-mode cases. Values that are different between L-mode and H-mode cases such as λ_q are cancelled in the derivation of the DLS model so only relative changes in control parameters are important.

In pulse 89749 between $\sim 51.3-52.0s$ the divertor re-attaches in the middle of the pulse and a change in impurity concentration is inferred during the re-attached period. There is no z position prediction

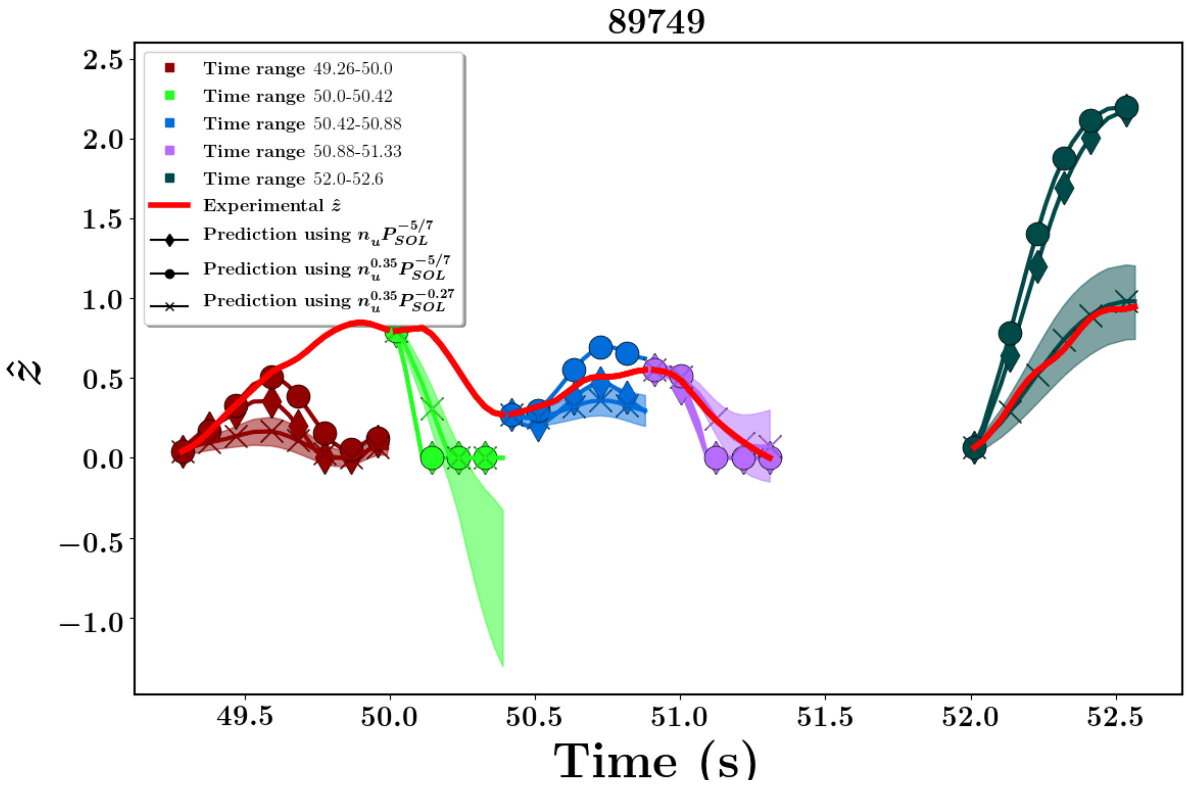

Figure 35: A comparison of predicted $\hat{z}$ position calculated using different combinations of exponents for the control parameters $n_u \& P_{SOL}$ to make predictions of $\hat{z}$. The prediction is made based on the starting position and control parameter at the start of each coloured section to predict every position in that section. The experimental $\hat{z}$ position is also plotted for comparison. Note that f_i is held constant in the $\hat{z}$ prediction.

while attached, since $\hat{z}$ would be 0, but figure 34 shows that the model predicts there would have to be an increase in f_z between the beginning and end of the attached period given that P_{SOL} increases and the ratio $f_z^{0.5}/P_{SOL}^{0.27}$ should be the same for the detachment threshold. It is also possible that nitrogen has stuck to the divertor tiles and is released in this section when target particle flux is increased, or that the nitrogen is better confined in the divertor while attached.

Applying the above analysis process to 89241 also implies that the impurity concentration rises during the earlier part of the pulse; see figure 25 to see that the f_z measurement supports that. This is particularly expected as pulse 89241 includes a linear increase in impurity seeding throughout the pulse.

The first detached section (after 50.5s) of 89241 has measurements of impurity concentration[113], which within the large error produced by the normalisation, and for all variations of exponents, matches the shallow increase in impurity concentration predicted as shown in figure 36. The drop in measured nitrogen concentration at $\sim 51.75s$ may be due to intra-ELM effects or the effect of detachment where the signal decreases, but if it is not a signal reduction then the exponent for the impurity concentration may also be too small. Unfortunately there is not enough f_z data overlap

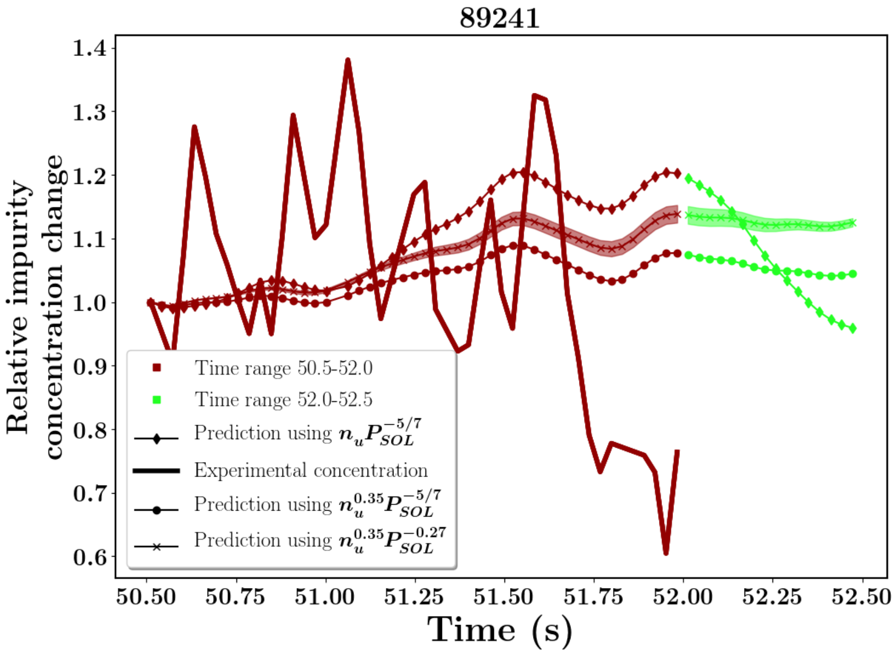

Figure 36: The predicted impurity concentration calculated using equation 68. The prediction is made based on the starting position and control parameter at a single time at 50.0s

with the detached portion of this pulse to confirm the dependence of the change in measured nitrogen concentration for the detachment front location movement in this pulse and thus the exponent for f_z. In addition, given the noise on the f_z experiment it cannot commented on whether the derived X_p and X_n lead to more believable f_z changes as found for pulse 89749.

In pulse 89751, the z position doesn't appear to correlate well to P_{SOL} or n_u although these control parameters do change in the pulse. One explanation is that the inferred impurity concentration changes are dominant, as supported by nitrogen seeding rate changes and the Kallenbach model[114] prediction of the f_z change (see figure 27(b)). The inferred impurity concentration aligns with the drops in the nitrogen seeding rate, although there may be a time delay between the gas valve seeding and nitrogen reaching the detachment front.

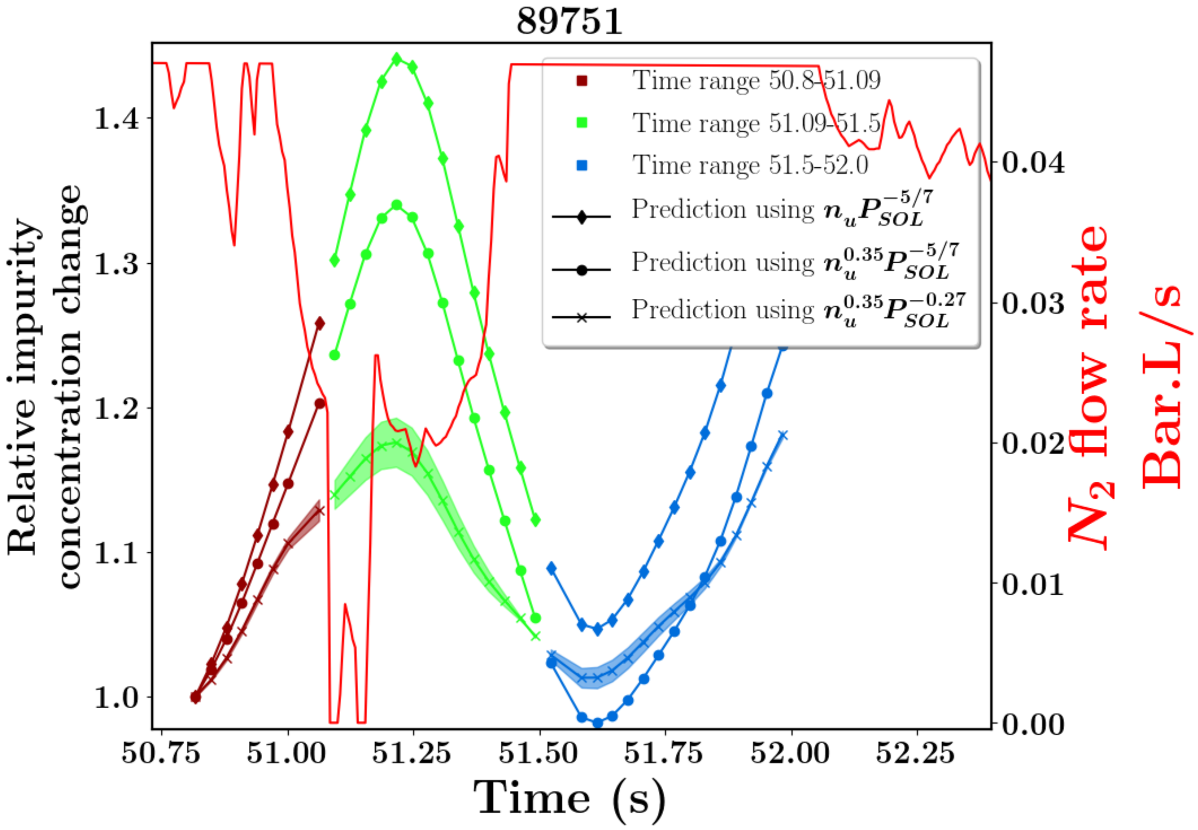

Figure 37: The predicted impurity concentration calculated using equation 68. The prediction is made based on the starting position and control parameter at a single time at 50.75s

6 Discussion

In this section, the impact of the changes in sensitivity strength (control variable exponents) in the DLS model and possible reasons for a reduction in sensitivity strength are discussed. The effect of lowering the detachment front sensitivity to P_{SOL} and n_u on scaling to an ITER-like scenario to predict the onset of detachment and detachment sensitivity are discussed. Possible reasons for the observed changes in sensitivity relative to the DLS model are discussed.

6.1 Impact of adjusted DLS sensitivity on scaling of detachment onset in ITER

The required impurity concentration for detachment is important to estimate, since it would be hard to detach the divertor if it is such a high percentage that affects core radiation and confinement. It is possible to use the DLS model to investigate the impact of scaling the required impurity concentration for detachment onset in ITER-like scenarios and what the impact of altering the sensitivity of detachment to changes in P_{SOL} and n_u. The application of the original exponents and proposed adjusted exponents to basic scenarios that could be used on ITER can be used to estimate how difficult it might be to move the detachment front to reach a desired detachment front location. Since the analysis in this thesis has not been able to analyse whether the f_z exponent might be changed it is left as the DLS model value.

In the DLS model, detachment onset can't be predicted from equations after normalisation, but before normalisation there exists a mixture of constants and variables in $U_1 = [2\pi R \lambda_q B_{pol}/B_\times]^{5/7} \left[\frac{7}{2\kappa_1}\right]^{2/7} \sqrt{2\kappa_1} \sqrt{\int_{T_c}^{T_h} Q(T) T^{1/2} dT}$ used in equation 35. Some parameters may be considered constant between the JET pulses investigated in this thesis and potential ITER scenarios, such as $B_{pol}/B_\times$, κ_1, $\int_{T_c}^{T_h} Q(T) T^{1/2} dT$ assuming nitrogen is a seeded impurity, $z_\times/L$ and the fraction of P_{SOL} to the outer divertor. Appendix section D derives the impurity concentration required for detachment onset in ITER which is shown here in equation 69.

$$f_{z,ITER} = f_{z,JET} \left(\frac{\frac{n_{u,JET}}{P_{SOL,JET}^{5/7}} [R_{JET} \lambda_{q,JET}]^{5/7} \frac{B_{t,ITER}}{B_{\times,ITER}} L_{JET}^{2/7}}{\frac{n_{u,ITER}}{P_{SOL,ITER}^{5/7}} [R_{ITER} \lambda_{q,ITER}]^{5/7} \frac{B_{t,JET}}{B_{\times,JET}} L_{ITER}^{2/7}} \right)^2 \tag{69}$$

Using the values in table 2 and equation 105 and assuming that $\frac{B_t}{B_\times} \sim 1$, the impurity concentration required for detachment in ITER is predicted to be $\sim 45\%$ without changing the DLS sensitivity exponents. Changing the upstream density between $3 - 5 \times 10^{19} m^{-3}$ can change this value to $\sim 80\% - 30\%$ respectively because of the high DLS exponent. Lowering P_{SOL} from $100MW$ to $70MW$ would decrease the onset required impurity concentration to $\sim 27\%$. Overall the original model exponents predict high impurity concentrations that are strongly dependent on how ITER operates. Using the adjusted model exponents and the values in table 2, the impurity concentration required for detachment in ITER is predicted to be $\sim 6\%$. Lowering P_{SOL} from $100MW$ to $70MW$ only changes the $f_{z,ITER}$ estimate to $\sim 5\%$ and changing the upstream density between between $3 - 5 \times 10^{19} m^{-3}$ only changes the $f_{z,ITER}$ estimate to $\sim 7\% - 5\%$ respectively because the reduced exponents lead to lowered sensitivity of $\hat{z}$ on control variable changes. In all cases the predicted impurity concentrations in ITER are predicted to be significant.

Device	R (m)	λ_q (mm)	L_{para} (m)	L (m)	P_{SOL} (MW)	n_u $(\times 10^{19} m^{-3})$	f_z
JET (89241)	3.84	1.8	26	29.11	4.56	2.4	0.035
ITER	8.2[65;26]	1[26]	70[116]	78*	100[65]	5[24]	-

Table 2: The values used to find the impurity concentration required for the onset of detachment using the DLS model. * L on ITER has been estimated by scaling the parallel connection length L_{para} on ITER as $\sim 70m$[116] using the ratio of parallel connection length on JET (26m) to the connection length L for JET in this table.

6.2 Scaling of detachment location sensitivity and windows to ITER scenarios including adjustments to control sensitivity

The DLS model predicts detachment is easier to control on ITER than JET (at $P_{SOL} = 5$MW), and even easier to control with reduced sensitivity from adjusted parameters.

The window of detachment can be estimated using equation 70 (derived from equation 99 in the appendix), the relative change in control parameters scales the same on JET and ITER assuming $B_\times / B_t \sim 1$ and $z_\times / L \sim 0.2$ are similar on JET and ITER. The total relative change to all 3 control parameter contributions with their respective exponents ("lumped" control parameter) is predicted to increase by $\sim 12\%$ to move the detachment front from the target to the X-point.

Control parameter detachment windows are broken down in table 3 to show the relative and estimated absolute change in one control variable while the others are considered constant. Lowering the model exponents for P_{SOL} and n_u increases the window of detachment for P_{SOL} and n_u, which predicts that P_{SOL} and n_u can be varied more without excessively moving the detachment front location. A H-L transition might not change the separatrix density as much as core densities[117], but P_{SOL} will change because changes in the stored energy in the core plasma. Even in the case of lowered exponents and the initial detachment front location at the X-point it is likely that the divertor will reattach. The ITER detachment window for f_z is uncertain because the detachment onset has a large range that onset f_z values could be, as predicted in section 6.1.

$$\frac{\left(\frac{n_u f_z^{1/2}}{P_{SOL}^{5/7}}\right)_\times}{\left(\frac{n_u f_z^{1/2}}{P_{SOL}^{5/7}}\right)_t} = \frac{\left[\frac{1-z_\times/L}{2}\right]^{-2/7}}{\left[\frac{1+z_\times/L}{2}\right]^{-2/7}} \tag{70}$$

Set of exponents used	$\frac{(P_{SOL})_t}{(P_{SOL})_\times}$	$\frac{(n_u)_\times}{(n_u)_t}$	$\frac{(f_z)_\times}{(f_z)_t}$	$(P_{SOL})_t - (P_{SOL})_\times$ (MW)		$(n_u)_\times - (n_u)_t$ ($\times 10^{19} m^{-3}$)		$(f_z)_\times - (f_z)_t$	
				JET	ITER	JET	ITER	JET	ITER
DLS model	1.18	1.12	1.25	0.34	7.4	0.29	0.61	0.01	0.077
Adjusted	1.53	1.39	-	0.79	17.3	0.93	1.95	-	0.012

Table 3: The predicted relative detachment window for changing each of the three DLS control variables P_{SOL}, n_u and f_z using the original DLS model exponents (-5/7, 1. and 1./2. respectively) compared to the adjusted model exponents (-0.27, 0.35 for P_{SOL}, n_u respectively). The relative values are converted to a range given a target. To show the absolute windows for JET and ITER the estimated starting P_{SOL} and n_u values used are: $(n_u)_{t,JET} = 2.4 \times 10^{19}$, $(n_u)_{t,ITER} = 4 \times 10^{19}$, $(P_{SOL})_{\times,JET} = 4.56MW$ and $(P_{SOL})_{\times,ITER} = 100MW$ (2.28MW and 50MW to the outer target for JET and ITER respectively). Note that P_{SOL} absolute windows are multiplied by a factor of 1/2 to the outer target. In pulse 89241 $(f_z)_{t,JET} = 0.035$, which scaled the detachment onset to $(f_z)_{t,ITER} = 0.18 - 0.29$ and $(f_z)_{t,ITER} = 0.041 - 0.049$ for DLS model exponents and adjusted exponents respectively.

Overall, the DLS model predictions show that a higher absolute control parameter value of at the onset of detachment, which requires larger absolute changes to a control parameter to move the detachment front position a fixed distance. This also means that a larger change to impurity concentration will also be needed to move the detachment front after detachment onset; thus it is both harder to reach detachment and move the detachment front on ITER. This does predict it will be easier to control the detachment front position once the ideal position of the detachment front has been reached, since small movements in the control parameters will have less of an effect on the detachment front position. The changes to the exponents explored in this thesis would suggest that the sensitivity to control parameters are reduced, which introducing these to the sensitivity scaling to ITER means that moving the detachment front position would become even harder than if scaled using the DLS model exponents. The reduction in sensitivity would mean that for the same relative change in control parameter, the detachment front position would move a shorter distance. This would mean the detachment front location would be easier to control but again much harder to move.

6.3 Possible reasons for higher detachment sensitivity in the DLS model

The DLS model is a simplified model that includes a number of assumptions that may cause the detachment front location sensitivity to changes in n_u and P_{SOL} to be higher than measured. This section will discuss which features of the DLS model and the data could introduce a disagreement that measures lower sensitivity. Missing particle or energy sources and sinks, missing control parameters, control parameter scaling assumptions or a mismatch between measured and predicted front positions are some topics discussed in the context of detachment front location sensitivity the following sections.

6.3.1 Physics not included in the DLS model

In the DLS model there are no inclusions of any energy sinks apart from impurity radiation and no inclusions of any energy sources apart from across the separatrix into the SOL (from P_{SOL}), but adding these terms would have an unknown effect on the DLS sensitivity. The energy balance between the sources and sinks included in the DLS model requires an assumption that the impurity concentration is constant over the thermal front and no energy changes exist between the thermal front and the target. The constant impurity concentration (and magnetic field strength) is assumed given that the thermal front is small compared to the total length of the divertor, which for JET could be a problem because of the short length of the outer leg. These possibilities are difficult to be evaluated experimentally, but by including terms in full models of the SOL, e.g. through use of SOLPS, the reason for sensitivity difference could be unravelled.

One other DLS model requirement is that the $q_{||}$ profile would need to satisfy the approximation that $T_u^{7/2} >> T_h^{7/2}$ where T_h is at the entrance to the thermal front. It is not known whether this is satisfied in JET. The result is that T_u is likely overestimated as a function of the detachment front location in the DLS model. This overestimation of T_u in the model could be one factor as to why control parameters are not moving the detachment front as much as predicted.

The effects of cross-field transport have not been considered in the DLS model. Relative changes to the detachment front location may be affected by this additional loss along flux tubes and produce a different power balance.

6.3.2 The role of assumptions of Control parameters on detachment front sensitivity

To use P_{SOL} measurements in DLS model calculations, the fraction flowing to inner and outer divertors is assumed constant. This assumption allows the total estimated P_{SOL} to be used because a fixed fraction of total P_{SOL} to the outer divertor would cancel out when considering the relative change $\left(P_{SOL}^{-5/7}\right)_2 / \left(P_{SOL}^{-5/7}\right)_1$. Without a fixed fraction of P_{SOL} to the outer divertor, the sensitivity of the DLS model could be affected. However, this might not be consistent with reduced DLS model sensitivity. Kirnev et al. [2005] show that the P_{SOL} to the outer target is a function of the magnitude of P_{SOL}, which, if P_{SOL} dropped in the DLS model, then a larger movement of the detachment front would be predicted. In a scenario in which P_{SOL} drops, the detachment front moves towards the X-point, but if the fraction of power to the outer divertor also drops, then the drop would move the detachment front more than DLS model predictions show for P_{SOL} in this thesis and not less. This would correspond to a higher sensitivity rather than the measured lower sensitivity for P_{SOL}.

In the DLS model, the parallel electron thermal conductivity κ, excluding the $T^{5/2}$ dependence, is considered a constant over the thermal front but could change throughout pulses as it is predicted to have a relationship with f_z. If κ_1 was considered a control parameter in the DLS model it would be included in equation 36 as $\frac{n_u \kappa_1^{3/14} \sqrt{f_z}}{P_{SOL}^{5/7}}$. Goldston et al. [2017] uses a correction to factor to account for a relationship between κ_1 and f_z. The scaling in Goldston et al. [2017] for κ_1 and f_z with nitrogen as a dominant impurity would reduce the control parameter contributions from changing $\kappa_1^{3/14}\sqrt{f_z}$ together and reduce the overall detachment location sensitivity to $\kappa_1^{3/14}\sqrt{f_z}$. From the investigation in this thesis, the relationship of sensitivity of the detachment front to changes in f_z could not be evaluated. If future investigations find the detachment front is too sensitive to impurity concentration, then a relationship should be investigated for the DLS model.

6.3.3 The role of detachment front position assumptions

The $\frac{D_\gamma}{D_\alpha}$ front edge position is not explicitly linked to the position of the hot end of the detachment front in the DLS model. This raises some uncertainty as to whether the DLS model, for a thermal front that is long [$(z_h - z_c)$ not $<<$ $z_\times$], is the DLS model a better predictor of $z_\times$, z_h or somewhere in between? This could lead to problems when the sensitivity strength. The DLS model detachment front position is found by balancing the energy crossing the SOL P_{SOL}, with impurity radiation below the detachment front position in the thermal front. This would not be balanced at the position of $\frac{D_\gamma}{D_\alpha}$ front edge on the outer leg (1-2.5eV), as impurity radiation would be higher up the outer leg towards the X-point. However, the effect of a lowering the amount of impurity radiation below the detachment front position can be considered by altering the energy balance to have only a fixed fraction A_q of the upstream heat flux dissipated below the detachment front position rather than all of it ($A_q = 1$). The constant fraction A_q would cancel through normalisation, and therefore DLS model sensitivity would not change as shown in equation 71 and therefore same exponents of sensitivity would be recovered (as in equation 36) regardless of the fraction A_q.

$$
\begin{aligned}
&A_q S_0(L - z_\times) = \\
&U n_u \sqrt{f_z} \frac{B_\times}{B_h} \left[S_0(L - z_\times) \left[\frac{(z_\times - z_h)}{3} [1 + \frac{B_h}{B_\times} + \frac{B_h^2}{B_\times^2}] + \frac{(L - z_\times)}{2} \right] \right]^{2/7}
\end{aligned} \tag{71}
$$

6.4 Future DLS model studies

There is not a large enough ratio of the total magnetic field at the X-point to that at the target ($\frac{B_\times}{B_{tar}}$)[1;91] on JET to significantly test whether the role of total flux expansion is properly predicted. Large total flux expansion is predicted to lower the detachment threshold in $n_{u,detach} \propto \frac{B_\times}{B_{tar}}$ and similarly increase the detachment window. However, the total flux expansion for the JET outer divertor is quite small ($\frac{B_\times}{B_{tar}} \sim 1.08$). Comparison to experimental cases with large total flux expansion (e.g. MAST-U) is a key next step.

In this thesis, assumptions about f_z being constant are used, but only for the L-mode pulse studied, which is not enough to confirm the sensitivity of the detachment front to f_z changes is consistent with the DLS model. A study measuring f_z increasing and decreasing while holding P_{SOL} and n_u constant (or using the adjusted P_{SOL} and n_u sensitivities), would need to move the detachment front towards the X-point and back to the target and would thus be a suitable test for the DLS model.

7 Conclusion

In this thesis a comparison has been carried out of the predictions by the DLS model of detachment front location movement to JET detached plasmas in three discharges. In general the model and experiment qualitatively agree; the DLS model predicts that detachment front location is more sensitive to control variables than experimental measurements indicate. Thus, the DLS model is a conservative estimate of detachment location sensitivity to the control variables n_u, P_{SOL}. Quantitative differences could certainly be due to the simplicity of the model.

Under the ansatz that the shortcomings in the model lead to exponents that are too large, a selected portion of a discharge where it is believed only the upstream density (n_u) control variable is significantly changing and found that if the n_u model exponent was reduced by a factor of ~ 2.5, the match between DLS model and experiment was much better. A similarly reduced model exponent for P_{SOL} was obtained for a period of the same L-mode discharge where both n_u & P_{SOL} were varied. When the same 'empirical' exponents were applied to H-mode discharges where it is expected that the impurity fraction control variable, f_z, was changing due to N_2-seeding, the predicted f_z variation was consistent with variations in P_{SOL} and core Z_{eff}.

Scaling the JET DLS model to parameter space to ITER shows that ITER higher impurity concentrations may be required to onset detachment. Detached sensitivity is predicted to be lower in ITER, as larger changes in impurity concentration are required to move the detachment front. Without 'empirical' exponents, the DLS model predicts 18-29% onset impurity concentrations, but with 'empirical' exponents, this is reduced to 4.1-4.9%. Without 'empirical' exponents, the DLS model predicts a 12% impurity concentration change for the detachment window, but with 'empirical' exponents, this is reduced to a 1.5% change. The detachment window is predicted to be larger than JET with either of these scalings.

This research required the development of a measure of the detachment front location using toroidal camera images filtered for D_γ and D_α along with image inversion techniques. We argue that the leading edge (towards the x-point) of the ratio, $\frac{D_\gamma}{D_\alpha}$, is indicative of the transition from the Balmer lines dominated by recombination to excitation; that location in the 2D divertor poloidal plane is thus a measure of the detachment front location distance from the outer target along a field line length which, for comparison to the DLS model, is normalised to create the variable $\hat{z}$. $\hat{z}$ was found to be inversely proportional to the total outer divertor target ion current, displaying a relationship that was not predicted and may provide further information on detachment. For example, the target ion current could be related to the same control variables as the detachment location. The strength of this relationship was not expected given the many nonlinear divertor processes that could have affected it.

The JET flux surfaces of the outer divertor have small variations in major radius over their length, leading to essentially no total flux expansion between x-point and target, $\frac{B_\times}{B_{tar}}$. Unfortunately, no tests could be made of the potentially strong effect of total flux expansion predicted by the DLS model; such a comparison is a key next step. Further studies should also ideally include measurements of the divertor impurity fraction as well as additional measures of detachment location.

Appendices

A The Derivation of $\mathbf{T_u}$ in the DLS model

This section contains the maths to simplify the upstream temperature in the DLS model from an integral form in equation 31 to analytical form in equation 32. Starting from equation 31 and inputting $B = B_t + (B_\times - B_t)\frac{z'}{z_\times}$ with gradient $\frac{dB_h}{dz} = \frac{(B_\times - B_t)}{z_\times}$ where

$$\begin{aligned} T_u &\sim \left[\frac{7S_0}{2\kappa_1}\left[(L - z_\times)\int_{z_h}^{z_\times} \frac{B^2}{B_\times^2}dz' + \int_{z_\times}^{L} \frac{B^2}{B_\times^2}(L - z')dz'\right]\right]^{2/7} \\ &= \left[\frac{7S_0}{2\kappa_1}\left[(L - z_\times)\int_{z_h}^{z_\times} \frac{B^2}{B_\times^2}dz' + \int_{z_\times}^{L} (L - z')dz'\right]\right]^{2/7} \end{aligned} \tag{72}$$

The total magnetic field squared is used throughout this derivation. The dependence on z position is highlighted in equation 73, where $X = B_t^2$, $Y = 2B_tB_\times - 2B_tB_t$ and $Z = -(B_\times^2 - 2B_\times B_t + B_t^2)$ are substituted to simplify other steps.

$$\begin{aligned} B^2 &= \left(B_t + (B_\times - B_t)\frac{z'}{z_\times}\right) \\ &= B_t^2 + 2B_t(B_\times - B_t)\frac{z'}{z_\times} - (B_\times - B_t)^2\left(\frac{z'}{z_\times}\right)^2 \\ &= B_t^2 + (2B_tB_\times - 2B_tB_t)\frac{z'}{z_\times} - (B_\times^2 - 2B_\times B_t + B_t^2)\left(\frac{z'}{z_\times}\right)^2 \\ &= X + Y\frac{z'}{z_\times} + Z\left(\frac{z'}{z_\times}\right)^2 \end{aligned} \tag{73}$$

The integral of B^2 is used in both parts of the integral in equation 72, so is written as V in equation 74.

$$
\begin{aligned}
V = \int B^2 dz' &= \int (X + Y\frac{z'}{z_\times} + Z\left(\frac{z'}{z_\times}\right)^2)dz' \\
&= (Xz' + \frac{Y}{2}\frac{z'^2}{z_\times} + Z\frac{z'^3}{3}\left(\frac{1}{z_\times}\right)^2) + C \\
&= z'(X + \frac{Y}{2}\frac{z'}{z_\times} + \frac{1}{3}Z\left(\frac{z'}{z_\times}\right)^2) + C \\
&= z'(X + \frac{Y}{2}\frac{z'}{z_\times} + \frac{1}{3}\left(B^2 - X - Y\frac{z'}{z_\times}\right)) + C \\
&= z'(\frac{2X}{3} + \frac{Y}{6}\frac{z'}{z_\times} + \frac{B^2}{3}) + C \\
&= \frac{z'}{3}(2X + \frac{Y}{2}\frac{z'}{z_\times} + B^2) + C \\
&= z'(\frac{2X}{3} + \frac{Y}{6}\frac{z'}{z_\times} + \frac{B^2}{3}) + C \\
&= \frac{z'}{3}(2X + \frac{Y}{2}\frac{(B - B_t)}{(B_\times - B_t)} + B^2) + C
\end{aligned}
\tag{74}
$$

The integral V is substituted where appropriate in equation 72 to get equation 75.

$$
\begin{aligned}
T_u &\sim \left[\frac{7S_0}{2\kappa_1}\left[\frac{(L - z_\times)}{B_\times^2}[V]_{z_h}^{z_\times} + L[z']_{z_\times}^{L} - [\frac{z'^2}{2}]_{z_\times}^{L}\right]\right]^{2/7} \\
T_u &\sim \left[\frac{7S_0}{2\kappa_1}\left[\frac{(L - z_\times)}{B_\times^2}[V]_{z_h}^{z_\times} + L(L - z_\times) - \frac{(L^2 - z_\times^2)}{2}\right]\right]^{2/7} \\
T_u &\sim \left[\frac{7S_0}{2\kappa_1}\left[\frac{(L - z_\times)}{B_\times^2}[V]_{z_h}^{z_\times} + L(L - z_\times) - \frac{(L - z_\times)(L + z_\times)}{2}\right]\right]^{2/7} \\
T_u &\sim \left[\frac{7S_0(L - z_\times)}{2\kappa_1}\left[\frac{1}{B_\times^2}[V]_{z_h}^{z_\times} + L - \frac{(L + z_\times)}{2}\right]\right]^{2/7} \\
T_u &\sim \left[\frac{7S_0(L - z_\times)}{2\kappa_1}\left[\frac{1}{B_\times^2}[V]_{z_h}^{z_\times} + \frac{(L - z_\times)}{2}\right]\right]^{2/7}
\end{aligned}
\tag{75}
$$

There are many steps which rearrange the equation in V. The $z'/3$ is first factored out to begin this process defining $V = z'W/3$ in equation 76.

$$\begin{aligned}
[V]_{z_h}^{z_\times} &= \frac{1}{3}[z_\times W|_{z_\times} - z_h W|_{z_h}] \\
&= \frac{(z_\times - z_h)}{3}\frac{1}{(z_\times - z_h)}[z_\times W|_{z_\times} - z_h W|_{z_h}] \\
&= \frac{(z_\times - z_h)}{3}\frac{1}{z_\times}\frac{1}{(1-\frac{z_h}{z_\times})}[z_\times W|_{z_\times} - z_h W|_{z_h}] \\
&= \frac{(z_\times - z_h)}{3}\frac{1}{(1-\frac{z_h}{z_\times})}[W|_{z_\times} - \frac{z_h}{z_\times} W|_{z_h}]
\end{aligned} \tag{76}$$

To further rearrange V, lots of z dependent terms are moved to become B dependent using the analytic definitions of B. One relationship that is used often in the many steps in equation 77 is $\frac{z_h}{z_\times} = \frac{(B_h - B_t)}{(B_\times - B_t)}$ and $\frac{1}{(1-\frac{z_h}{z_\times})} = \frac{(B_\times - B_t)}{(B_\times - B_h)}$. Overall the steps in equation 77 are a rearrangement to follow the DLS model derivation in Lipschultz et al. [2016].

$$
\begin{gathered}
V = \frac{(z_\times - z_h)}{3}\frac{(B_\times - B_t)}{(B_\times - B_h)}[W|_{z_\times} - \frac{(B_h - B_t)}{(B_\times - B_t)}W|_{z_h}] \\
= \frac{(z_\times - z_h)}{3}\frac{(B_\times - B_t)}{(B_\times - B_h)}[(2X + \frac{Y}{2}\frac{(B_\times - B_t)}{(B_\times - B_t)} + B_\times^2) - \frac{(B_h - B_t)}{(B_\times - B_t)}(2X + \frac{Y}{2}\frac{(B_h - B_t)}{(B_\times - B_t)} + B_h^2)] \\
= \frac{(z_\times - z_h)}{3}\frac{1}{(B_\times - B_h)}[(2X(B_\times - B_t) + \frac{Y}{2}(B_\times - B_t) + B_\times^2(B_\times - B_t)) - (B_h - B_t)(2X + \frac{Y}{2}\frac{(B_h - B_t)}{(B_\times - B_t)} + B \\
= \frac{(z_\times - z_h)}{3}\frac{1}{(B_\times - B_h)}[(2B_t^2(B_\times - B_t) + \frac{(2B_tB_\times - 2B_tB_t)}{2}(B_\times - B_t) + \\
B_\times^2(B_\times - B_t)) - (B_h - B_t)(2B_t^2 + \frac{(2B_tB_\times - 2B_tB_t)}{2}\frac{(B_h - B_t)}{(B_\times - B_t)} + B_h^2)] \\
= \frac{(z_\times - z_h)}{3}\frac{1}{(B_\times - B_h)}[2B_t^2B_\times - 2B_t^3 + B_tB_\times^2 - B_t^2B_\times - B_t^2B_\times + B_t^3 \\
B_\times^3 - B_\times^2B_t - 2B_t^2(B_h - B_t) - (B_tB_\times - B_t^2)\frac{(B_h - B_t)^2}{(B_\times - B_t)} - (B_h - B_t)B_h^2] \\
= \frac{(z_\times - z_h)}{3}\frac{1}{(B_\times - B_h)}[-B_t^3 + \\
B_\times^3 - 2B_t^2B_h + 2B_t^3 - (B_tB_\times - B_t^2)\frac{(B_h - B_t)^2}{(B_\times - B_t)} - (B_h - B_t)B_h^2] \\
= \frac{(z_\times - z_h)}{3}\frac{1}{(B_\times - B_h)}[B_\times^3 - 2B_t^2B_h + B_t^3 - B_t(B_\times - B_t)\frac{(B_h - B_t)^2}{(B_\times - B_t)} - (B_h - B_t)B_h^2] \\
= \frac{(z_\times - z_h)}{3}\frac{1}{(B_\times - B_h)}[B_\times^3 - 2B_t^2B_h + B_t^3 - B_t(B_h - B_t)^2 - (B_h - B_t)B_h^2] \\
= \frac{(z_\times - z_h)}{3}\frac{1}{(B_\times - B_h)}[B_\times^3 - 2B_t^2B_h + B_t^3 - B_tB_h^2 + 2B_t^2B_h - B_t^3 - B_h^3 + B_tB_h^2] \\
= \frac{(z_\times - z_h)}{3}\frac{1}{(B_\times - B_h)}[B_\times^3 - B_h^3] \\
= \frac{(z_\times - z_h)}{3}\frac{1}{(B_\times - B_h)}[(B_\times - B_h)(B_\times^2 + B_\times B_h + B_h^2)] \\
= \frac{(z_\times - z_h)}{3}[B_\times^2 + B_\times B_h + B_h^2]
\end{gathered}
\tag{77}
$$

The final form of equation 77 is substituted back into equation 75 to match the formula in Lipschultz et al. [2016] which is shown in equation 78.

$$
\begin{gathered}
T_u \sim \left[\frac{7S_0(L - z_\times)}{2\kappa_1}\left[\frac{1}{B_\times^2}\frac{(z_\times - z_h)}{3}[B_\times^2 + B_\times B_h + B_h^2] + \frac{(L - z_\times)}{2}\right]\right]^{2/7} \\
T_u \sim \left[\frac{7S_0(L - z_\times)}{2\kappa_1}\left[\frac{(z_\times - z_h)}{3}[1 + \frac{B_h}{B_\times} + \frac{B_h^2}{B_\times^2}] + \frac{(L - z_\times)}{2}\right]\right]^{2/7}
\end{gathered}
\tag{78}
$$

B Derive the partial derivative of the front position to a single control parameter

Starting from the generalised form of equation 35 for 1 control variable, where A includes the constant U and other constants introduced when P_{SOL} is substituted in. The log part of the fraction is also simplified to I.

$$\begin{aligned} C^{X_c} &= A\left\{\frac{B_h}{B_\times}\left[\frac{(z_\times - z_h)}{3}\left(1+\left|\frac{B_h}{B_\times}\right|+\left|\frac{B_h}{B_\times}\right|^2\right)+\frac{(L-z_\times)}{2}\right]^{-2/7}\right\} \\ &= A\frac{B_h}{B_\times}I^{-2/7} \end{aligned} \tag{79}$$

Differentiate both sides wrt z.using $\frac{\partial I^{-2/7}}{\partial z_h} = \frac{2}{7}\frac{I^{2/7}}{I}\frac{\partial I}{\partial z_h}$

$$\begin{aligned} X_c\frac{C^{X_c}}{C}\frac{\partial C}{\partial z_h} &= A\frac{B_h}{B_\times}I^{-2/7} \\ X_c\frac{A}{B_\times}\frac{B_hI^{-2/7}}{C}\frac{\partial C}{\partial z_h} &= \frac{A}{B_\times}\frac{\partial(B_hI^{-2/7})}{\partial z_h} \\ X_c\frac{B_hI^{-2/7}}{C}\frac{\partial C}{\partial z_h} &= \frac{\partial(B_hI^{-2/7})}{\partial z_h} \\ X_c\frac{B_hI^{-2/7}}{C}\frac{\partial C}{\partial z_h} &= B_h\frac{\partial I^{-2/7}}{\partial z_h}+I^{-2/7}\frac{\partial B_h}{\partial z_h} \\ X_c\frac{B_hI^{-2/7}}{C}\frac{\partial C}{\partial z_h} &= B_h\frac{2}{7}\frac{I^{-2/7}}{I}\frac{\partial I}{\partial z_h}+I^{-2/7}\frac{\partial B_h}{\partial z_h} \\ X_c\frac{B_h}{C}\frac{\partial C}{\partial z_h} &= \frac{2}{7}\frac{B_h}{I}\frac{\partial I}{\partial z_h}+\frac{\partial B_h}{\partial z_h} \end{aligned} \tag{80}$$

Using the approximation for magnetic field as

$$B_h = B_t + (B_\times - B_t)\frac{z}{z_\times} \tag{81}$$

The derivative is:

$$\frac{\partial B_h}{\partial z_h} = \frac{(B_\times - B_t)}{z_\times} \tag{82}$$

It will also be helpful to rearrange equation 81 rearranged for z_h

$$z_h = z_\times\frac{(B_h - B_t)}{(B_\times - B_t)} \tag{83}$$

First finding $\frac{\partial I}{\partial z_h}$

$$\frac{\partial I}{\partial z_h} = -\frac{1}{3}\left(1 + \left|\frac{B_h}{B_\times}\right| + \left|\frac{B_h}{B_\times}\right|^2\right) + \frac{(z_\times - z_h)}{3}\frac{\partial B_h}{\partial z_h}\left(\frac{1}{B_\times} + \frac{2B_h}{B_\times^2}\right) \tag{84}$$

Next substituting 83 and 82 into 84

$$\begin{aligned}
\frac{\partial I}{\partial z_h} &= -\frac{1}{3}\left(1 + \left|\frac{B_h}{B_\times}\right| + \left|\frac{B_h}{B_\times}\right|^2\right) + \frac{\left(z_\times - z_\times \frac{(B_h - B_t)}{(B_\times - B_t)}\right)}{3}\frac{(B_\times - B_t)}{z_\times}\left(\frac{1}{B_\times} + \frac{2B_h}{B_\times^2}\right)\\
\frac{\partial I}{\partial z_h} &= -\frac{1}{3}\left(1 + \left|\frac{B_h}{B_\times}\right| + \left|\frac{B_h}{B_\times}\right|^2\right) + \frac{\Big((B_\times - B_t) - (B_h - B_t)\Big)}{3}\left(\frac{1}{B_\times} + \frac{2B_h}{B_\times^2}\right)\\
\frac{\partial I}{\partial z_h} &= -\frac{1}{3}\left(1 + \left|\frac{B_h}{B_\times}\right| + \left|\frac{B_h}{B_\times}\right|^2\right) + \frac{1}{3}\left(1 + \frac{2B_h}{B_\times} - \frac{B_h}{B_\times} - \frac{2B_h^2}{B_\times^2}\right)\\
\frac{\partial I}{\partial z_h} &= -\frac{1}{3}\left(\left|\frac{B_h}{B_\times}\right|^2\right) + \frac{1}{3}\left(-\frac{2B_h^2}{B_\times^2}\right)\\
\frac{\partial I}{\partial z_h} &= -\frac{B_h^2}{B_\times^2}
\end{aligned} \tag{85}$$

Substitute equation 85 and equation 82 into equation 80

$$\begin{aligned}
X_c\frac{B_h}{C}\frac{\partial C}{\partial z_h} &= \frac{2}{7}\frac{B_h}{I}\frac{B_h^2}{B_\times^2} + \frac{(B_\times - B_t)}{z_\times}\\
X_c\frac{1}{C}\frac{\partial C}{\partial z_h} &= \frac{2}{7}\frac{B_h^2}{IB_\times^2} + \frac{(B_\times - B_t)}{z_\times B_h}\\
X_c\frac{1}{C}\frac{\partial C}{\partial z_h} &= \frac{2}{7}\frac{B_h^2}{IB_\times^2} + \left(1 - \frac{B_t}{B_\times}\right)\frac{B_\times}{B_h}\frac{1}{z_\times}
\end{aligned} \tag{86}$$

Taking the reciprocal of this then rearranging gives

$$\begin{aligned}
\frac{1}{X_c}C\frac{\partial z_h}{\partial C} &= \left\{\frac{2}{7}\frac{B_h^2}{IB_\times^2} + \left(1 - \frac{B_t}{B_\times}\right)\frac{B_\times}{B_h}\frac{1}{z_\times}\right\}^{-1}\\
C\frac{\partial z_h}{\partial C} &= X_c\left\{\frac{2}{7}\frac{B_h^2}{B_\times^2}\left[\frac{(z_\times - z_h)}{3}\left(1 + \left|\frac{B_h}{B_\times}\right| + \left|\frac{B_h}{B_\times}\right|^2\right) + \frac{(L - z_\times)}{2}\right]^{-1} + \left(1 - \frac{B_t}{B_\times}\right)\frac{B_\times}{B_h}\frac{1}{z_\times}\right\}^{-1}
\end{aligned} \tag{87}$$

Which may be multiplied by $\frac{1}{L}$ to make the equation dimensionless. Additionally rearranging equation 81 for B_t gives $B_t = \frac{B_h - \frac{B_\times z_h}{z_\times}}{1-\frac{z_h}{z_\times}}$ that can be substituted into equation 87 to get equation 88.

$$C\frac{\partial z_h}{\partial C} = X_c\left\{\frac{2}{7}\frac{B_h^2}{B_\times^2}\left[\frac{(z_\times - z_h)}{3}\left(1 + \left|\frac{B_h}{B_\times}\right| + \left|\frac{B_h}{B_\times}\right|^2\right) + \frac{(L - z_\times)}{2}\right]^{-1} + \left(1 - \frac{\frac{B_h}{B_\times} - \frac{z_h}{z_\times}}{1 - \frac{z_h}{z_\times}}\right)\frac{B_\times}{B_h}\frac{1}{z_\times}\right\}^{-1} \tag{88}$$

C Magnetic Field assumptions

The DLS model is derived again without an analytical form of the magnetic field. Starting from the energy source terms that are determined differently above and below the X-point, and which was used in equation 31 (equation 17 in Lipschultz et al. [2016]). All of the step in this section are made with the same assumptions as in section 2.6.3.

$$\frac{2\kappa_1 B_\times^2}{7B^2}\frac{dT^{7/2}}{dz} = \begin{cases} S_0(L - z_\times), & \text{for } z < z_\times \\ S_0(L - z), & \text{for } z \geq z_\times \end{cases} \tag{89}$$

C.1 General Magnetic field

Integrate both sides wrt z to get equation 90. $q_i = -S_0(L - z_\times)$

$$T_u = \left[\frac{7S_0}{2\kappa_1 B_\times^2}\left[\int_z^{z_\times} B^2(z)(L - z_\times)dz + \int_{z_\times}^{L} B^2(z)(L - z)dz\right]\right]^{2/7} \tag{90}$$

==

Substituting equation 90 into equation 28, repeated below in equation 91 gives equation 92, where U is consistent with the same constant used in equation 28.

$$q_f = -\sqrt{2\kappa_1 f_I}n_u T_u \frac{B_\times}{B(z)}\sqrt{\int_{T_c}^{T_h} T^{1/2}Q(T)dT} \tag{91}$$

$$q_f = -U\sqrt{f_I}n_u\frac{B_\times}{B(z)}\left(\frac{S_0}{B_\times^2}\right)^{2/7}\left[\int_z^{z_\times} B^2(z)(L-z_\times)dz + \int_{z_\times}^{L} B^2(z)(L-z)dz\right]^{2/7} \tag{92}$$

===

By balancing heat fluxes $q_f = q_i = -S_0(L-z_\times)$, rearrangements are made in equations 93 and 94.

$$\left[S_0(L-z_\times)\right]^{5/7} = U\sqrt{f_I}n_u\frac{B_\times^{3/7}}{B(z)}\left[\int_z^{z_\times} B^2(z)dz + \int_{z_\times}^{L}\frac{B^2(z)(L-z)}{L-z_\times}dz\right]^{2/7} \tag{93}$$

$$n_u = \frac{\left[S_0(L-z_\times)\right]^{5/7}}{U\sqrt{f_I}B_\times^{3/7}}B(z)\left[\int_z^{z_\times} B^2(z)dz + \int_{z_\times}^{L}\frac{B^2(z)(L-z)}{L-z_\times}dz\right]^{-2/7} \tag{94}$$

===

Equation 94 is generalised with a single constant A in equation 95, before the partial derivative is taken to find equation 97. Equation 95 is then normalised to equation 97 to remove the constant A.

$$C^{X_c} = AB(z)\left[\int_z^{z_\times} B^2(z)dz + \int_{z_\times}^{L}\frac{B^2(z)(L-z)}{L-z_\times}dz\right]^{-2/7} \tag{95}$$

$$C\frac{\partial z}{\partial C} = X_c\left[\frac{1}{B(z)}\frac{\partial B(z)}{\partial z} + \frac{2}{7}B^2(z)\left[\int_z^{z_\times} B^2(z)dz + \int_{z_\times}^{L}\frac{B^2(z)(L-z)}{L-z_\times}dz\right]^{-1}\right]^{-1} \tag{96}$$

$$\frac{\left(\frac{n_u f_z^{1/2}}{P_{SOL}^{5/7}}\right)_2}{\left(\frac{n_u f_z^{1/2}}{P_{SOL}^{5/7}}\right)_1} = \frac{B_2}{B_1}\frac{\left[\int_{z_2}^{z_\times} B^2(z)dz + \int_{z_\times}^{L}\frac{B^2(z)(L-z)}{L-z_\times}dz\right]^{-2/7}}{\left[\int_{z_1}^{z_\times} B^2(z)dz + \int_{z_\times}^{L}\frac{B^2(z)(L-z)}{L-z_\times}dz\right]^{-2/7}} \tag{97}$$

C.2 Constant Magnetic field

Starting from equation 35 the and by assuming a small change in magnetic field between the x-point and target $B_h \sim B_\times$. The constant is re-written as $U_{mod} = U_1^{-1}$ and simplification shown in equation 98

$$\begin{aligned}\frac{n_u\sqrt{f_z}}{P_{SOL}^{5/7}} &= U_1^{-1}\frac{B_h}{B_\times}\left[\left[\frac{(z_\times - z_h)}{3}[1+\frac{B_h}{B_\times}+\frac{B_h^2}{B_\times^2}] + \frac{(L-z_\times)}{2}\right]\right]^{-2/7} \\ \frac{n_u\sqrt{f_z}}{P_{SOL}^{5/7}} &= U_{mod}\left[z_\times - z_h + \frac{L-z_\times}{2}\right]^{-2/7} \\ \frac{n_u\sqrt{f_z}}{P_{SOL}^{5/7}} &= U_{mod}\left[\frac{L+z_\times}{2} - z_h\right]^{-2/7}\end{aligned} \tag{98}$$

By evaluating at an fixed arbitrary point (1) and substituting into work out at a second point (2), equation 99 is found.

$$\frac{\left(\frac{n_u f_z^{1/2}}{P_{SOL}^{5/7}}\right)_2}{\left(\frac{n_u f_z^{1/2}}{P_{SOL}^{5/7}}\right)_1} = \frac{\left[\frac{L+z_\times}{2} - z_2\right]^{-2/7}}{\left[\frac{L+z_\times}{2} - z_1\right]^{-2/7}} \tag{99}$$

Rearranging equation 99 for z_2 is then shown below in equation 100.

$$\begin{aligned}\left[\frac{L+z_\times}{2} - z_1\right]\left[\frac{\left(\frac{n_u f_z^{1/2}}{P_{SOL}^{5/7}}\right)_2}{\left(\frac{n_u f_z^{1/2}}{P_{SOL}^{5/7}}\right)_1}\right]^{-7/2} &= \left[\frac{L+z_\times}{2} - z_2\right] \\ z_2 &= \left[\frac{L+z_\times}{2}\right] - \left[\frac{L+z_\times}{2} - z_1\right]\left[\frac{\left(\frac{n_u f_z^{1/2}}{P_{SOL}^{5/7}}\right)_2}{\left(\frac{n_u f_z^{1/2}}{P_{SOL}^{5/7}}\right)_1}\right]^{-7/2}\end{aligned} \tag{100}$$

For sensitivity, start at equation 98 written as a function of only 1 parameter where C^{X_c} is either $P_{SOL}^{-5/7}$, n_u^1 or $f_z^{1/2}$. This is then rearranged for z_h.

$$\begin{aligned} C^{X_c} &= U_{mod}\left[\frac{L+z_{\times}}{2} - z_h\right]^{-2/7} \\ z_h &= \frac{L+z_{\times}}{2} - \frac{C^{-7X_c/2}}{U_{mod}^{-7/2}} \end{aligned} \tag{101}$$

Differentiating z_h wrt C, where C can be 3 variables so is represented as a partial derivative.

$$\begin{aligned} \frac{\partial z_h}{\partial C} &= \frac{7X_c}{2}\frac{C^{-7X_c/2-1}}{U_{mod}^{-7/2}} \\ \frac{\partial z_h}{\partial C} &= \frac{7X_c}{2C}\frac{C^{-7X_c/2}}{U_{mod}^{-7/2}} \end{aligned} \tag{102}$$

From equation 101, rearranged $\frac{C^{-7X_c/2}}{U_{mod}^{-7/2}} = \left[\frac{L+z_{\times}}{2} - z_h\right]$, so replacing this in equation 102 gives equation 103.

$$\frac{\partial z_h}{\partial C} = \frac{7X_c}{2C}\left[\frac{L+z_{\times}}{2} - z_h\right] \tag{103}$$

D Detachment onset scaling

The goal of the following is to develop a simple method for scaling the detachment threshold in divertor impurity concentration, f_z, from JET to ITER. We start from equation 35 and make the following assumptions: a) JET and ITER have the same ratio of $B_{pol}/B_\times$; b) κ_1 is same for both; c) detachment in both tokamaks is achieved through nitrogen seeding such that the Lengyel formulation of the radiated power along a flux tube is the same for both tokamaks - $\int_{T_c}^{T_h} Q(T)T^{1/2}dT$; and d) we assume for both JET and ITER that $B_t/B_\times \sim 1$ is a good enough approximation (actual value ~ 1.1); The term $[1 + \frac{B_t}{B_\times} + \frac{B_t^2}{B_\times^2}] \sim 3$. Thus the value of U_1 is only different between the two tokamaks through differences in $R\lambda_q$. Further assuming that $z_\times/L$ is the same for the two experiments given fairly similar equlibria (core and divertor flux surfaces) we collect all constant terms into the new constant, C:

$$C = [2\pi B_{pol}/B_\times]^{5/7} \left[\frac{7}{2\kappa_1}\right]^{2/7} \sqrt{2\kappa_1} \sqrt{\int_{T_c}^{T_h} Q(T)T^{1/2}dT} \left(\frac{(1+\frac{z_\times}{L})}{2}\right)^{2/7}.$$

Then, the scaling from JET to ITER is simplified to:

$$\frac{n_u\sqrt{f_z}}{P_{SOL}^{5/7}} = \left(C[R\lambda_q]^{5/7}\right)^{-1} \frac{B_t}{B_\times} L^{-2/7} \tag{104}$$

Equation 104 can now be used to solve for the required impurity concentration for the onset of detachment in ITER ($f_{z,ITER}$) by dividing equation 104 in the ITER case by equation 104 in the JET case.

$$f_{z,ITER} = f_{z,JET} \left(\frac{\frac{n_{u,JET}}{P_{SOL,JET}^{5/7}} [R_{JET}\lambda_{q,JET}]^{5/7} \frac{B_{t,ITER}}{B_{\times,ITER}} L_{JET}^{2/7}}{\frac{n_{u,ITER}}{P_{SOL,ITER}^{5/7}} [R_{ITER}\lambda_{q,ITER}]^{5/7} \frac{B_{t,JET}}{B_{\times,JET}} L_{ITER}^{2/7}} \right)^2 \tag{105}$$

References

[1] Bruce Lipschultz, Felix I. Parra, and Ian H. Hutchinson. Sensitivity of detachment extent to magnetic configuration and external parameters. *Nuclear Fusion*, 2016. ISSN 17414326. doi: 10.1088/0029-5515/56/5/056007.

[2] David Gann and Ian Chapman. UKAEA Annual Report and Accounts. Technical report, 2018.

[3] A. Sykes, A. E. Costley, C. G. Windsor, O. Asunta, G. Brittles, P. Buxton, V. Chuyanov, J. W. Connor, M. P. Gryaznevich, B. Huang, J. Hugill, A. Kukushkin, D. Kingham, A. V. Langtry, S. McNamara, J. G. Morgan, P. Noonan, J. S.H. Ross, V. Shevchenko, R. Slade, and G. Smith. Compact fusion energy based on the spherical tokamak. *Nuclear Fusion*, 58(1), 2018. ISSN 17414326. doi: 10.1088/1741-4326/aa8c8d.

[4] A. J. Creely, M. J. Greenwald, S. B. Ballinger, D. Brunner, J. Canik, J. Doody, T. Fülöp, D. T. Garnier, R. Granetz, T. K. Gray, C. Holland, N. T. Howard, J. W. Hughes, J. H. Irby, V. A. Izzo, G. J. Kramer, A. Q. Kuang, B. Labombard, Y. Lin, B. Lipschultz, N. C. Logan, J. D. Lore, E. S. Marmar, K. Montes, R. T. Mumgaard, C. Paz-Soldan, C. Rea, M. L. Reinke, P. Rodriguez-Fernandez, K. Särkimäki, F. Sciortino, S. D. Scott, A. Snicker, P. B. Snyder, B. N. Sorbom, R. Sweeney, R. A. Tinguely, E. A. Tolman, M. Umansky, O. Vallhagen, J. Varje, D. G. Whyte, J. C. Wright, S. J. Wukitch, and J. Zhu. Overview of the SPARC tokamak. *Journal of Plasma Physics*, (2020):1–25, 2020. ISSN 14697807. doi: 10.1017/S0022377820001257.

[5] I. T. Chapman and A. W. Morris. UKAEA capabilities to address the challenges on the path to delivering fusion power. *Philosophical Transactions of the Royal Society A: Mathematical, Physical and Engineering Sciences*, 377(2141), 2019. ISSN 1364503X. doi: 10.1098/rsta.2017.0436.

[6] K. Ikeda. Progress in the ITER Physics Basis. *Nuclear Fusion*, 47(6), 2007. ISSN 00295515. doi: 10.1088/0029-5515/47/6/E01.

[7] Mitsuru Kikuchi, Karl Lackner, and Minh Quang. Fusion Physics. *Iaea*, pages 24–26, 2012.

[8] Victor Udintsev. Measurements of temperature and density in magnetic confinement fusion devices. *Nuclear Instruments and Methods*, pages 649–652, 2012. ISSN 0168-9002. doi: https://doi.org/10.1016/j.nima.2010.01.044.

[9] Daniel Clery. Alternatives to tokamaks: A faster-better-cheaper route to fusion energy? *Philo-*

sophical Transactions of the Royal Society A: Mathematical, Physical and Engineering Sciences*, 377(2141), 2019. ISSN 1364503X. doi: 10.1098/rsta.2017.0431.

[10] Yuhong Xu. A general comparison between tokamak and stellarator plasmas. *Matter and Radiation at Extremes*, 1(4):192–200, 2016. ISSN 2468080X. doi: 10.1016/j.mre.2016.07.001. URL `http://dx.doi.org/10.1016/j.mre.2016.07.001`.

[11] J. Wesson. *Tokamaks*. 2004.

[12] A. E. Costley, J. Hugill, and P. F. Buxton. On the power and size of tokamak fusion pilot plants and reactors. *Nuclear Fusion*, 55(3), 2015. ISSN 17414326. doi: 10.1088/0029-5515/55/3/033001.

[13] George Miley. Fusion Cross Sections and Reactivities. 1974. doi: 10.2172/4014032. URL `http://www.osti.gov/scitech/servlets/purl/4014032`.

[14] S. Zheng, D. B. King, L. Garzotti, E. Surrey, and T. N. Todd. Fusion reactor start-up without an external tritium source. *Fusion Engineering and Design*, 103:13–20, 2016. ISSN 09203796. doi: 10.1016/j.fusengdes.2015.11.034.

[15] A. M. Bradshaw, T. Hamacher, and U. Fischer. Is nuclear fusion a sustainable energy form? *Fusion Engineering and Design*, 86(9-11):2770–2773, 2011. ISSN 09203796. doi: 10.1016/j.fusengdes.2010.11.040. URL `http://dx.doi.org/10.1016/j.fusengdes.2010.11.040`.

[16] K.C. Jordan, B.C. Blanke, and W.A. Dudley. Half-life of tritium. *Journal of Inorganic and Nuclear Chemistry*, 29(9):2129–2131, 1967. doi: https://doi.org/10.1016/0022-1902(67)80265-3. URL `https://www.sciencedirect.com/science/article/pii/0022190267802653`.

[17] T. Sunn Pedersen, M. Otte, S. Lazerson, P. Helander, S. Bozhenkov, C. Biedermann, T. Klinger, R. C. Wolf, H. S. Bosch, Ivana Abramovic, Simppa Äkäslompolo, Pavel Aleynikov, Ksenia Aleynikova, Adnan Ali, Arturo Alonso, Gabor Anda, Tamara Andreeva, Enrique Ascasibar, Jürgen Baldzuhn, Martin Banduch, Tullio Barbui, Craig Beidler, Andree Benndorf, Marc Beurskens, Wolfgang Biel, Dietrich Birus, Boyd Blackwell, Emilio Blanco, Marko Blatzheim, Torsten Bluhm, Daniel Böckenhoff, Peter Bolgert, Matthias Borchardt, Lukas Georg Böttger, Rudolf Brakel, Christian Brandt, Torsten Bräuer, Harald Braune, Rainer Burhenn, Birger Buttenschön, Victor Bykov, Ivan Calvo, Alvaro Cappa, Andre Carls, Bernardo Brotas De Carvalho, Francisco Castejon, Mark Cianciosa, Michael Cole, Stefan Costea, Gabor Cseh, Agata Czarnecka, Andrea Da Molin, Eduardo De La Cal, Angel De La Pena, Sven Degenkolbe, Chandra Prakash Dhard, Andreas Dinklage, Marion Dostal, Michael Drevlak, Pe-

ter Drewelow, Philipp Drews, Andrzej Dudek, Frederic Durodie, Anna Dzikowicka, Paul Von Eeten, Florian Effenberg, Michael Endler, Volker Erckmann, Teresa Estrada, Nils Fahrenkamp, Joris Fellinger, Yühe Feng, Waldemar Figacz, Oliver Ford, Tomasz Fornal, Heinke Frerichs, Golo Fuchert, Manuel Garcia-Munoz, Benedikt Geiger, Joachim Geiger, Niels Gierse, Alena Gogoleva, Bruno Goncalves, Dorothea Gradic, Michael Grahl, Silvia Groß, Heinz Grote, Olaf Grulke, Carlos Guerard, Matthias Haas, Jeffrey Harris, Hans Jürgen Hartfuß, Dirk Hartmann, Dag Hathiramani, Bernd Hein, Stefan Heirnich, Sophia Henneberg, Christine Hennig, Julio Hernandez, Carlos Hidalgo, Ulises Hidalgo, Matthias Hirsch, Udo Höfel, Hauke Hölbe, Alf Hölting, Michael Houry, Valentina Huber, Codrina Ionita, Ben Israeli, Slowomir Jablonski, Marcin Jakubowski, Anton Jansen Van Vuuren, Hartmut Jenzsch, Jacek Kaczmarczyk, Johann Peter Kallmeyer, Ute Kamionka, Hiroshi Kasahara, Naoki Kenmochi, Winfried Kernbichler, Carsten Killer, David Kinna, Ralf Kleiber, Jens Knauer, Florian Köchl, Gabor Kocsis, Yaroslav Kolesnichenko, Axel Könies, Ralf König, Petra Kornejew, Felix Köster, Andreas Krämer-Flecken, Rüdiger Krampitz, Natalia Krawzyk, Thierry Kremeyer, Maciej Krychowiak, Ireneusz Ksiazek, Monika Kubkowska, Georg Kühner, Taina Kurki-Suonio, Peter Kurz, Katja Küttler, Sehyun Kwak, Matt Landreman, Andreas Langenberg, Fernando Lapayese, Heike Laqua, Heinrich Peter Laqua, Ralph Laube, Michael Laux, Holger Lentz, Marc Lewerentz, Yunfeng Liang, Shaocheng Liu, Jim Felix Lobsien, Joaquin Loizu Cisquella, Daniel Lopez-Bruna, Jeremy Lore, Axel Lorenz, Shoacheng Lui, Vadym Lutsenko, Henning Maassberg, Jeanette Maisano-Brown, Oleksandr Marchuk, Lionello Marrelli, Stefan Marsen, Nikolai Marushchenko, Suguru Masuzaki, Kieran McCarthy, Paul McNeely, Francisco Medina, Dusan Milojevic, Alexey Mishchenko, Bernd Missal, Joseph Mittelstaedt, Albert Mollen, Victor Moncada, Thomas Mönnich, Dmitry Moseev, Michael Nagel, Dirk Naujoks, G. Hutch Neilson, Olaf Neubauer, Ulrich Neuner, Tran Tranh Ngo, Holger Niemann, Carolin Nührenberg, Jürgen Nührenberg, Marian Ochando, Kunihiro Ogawa, Jef Ongena, Hans Oosterbeek, Novimir Pablant, Danilo Pacella, Luis Pacios, Nerea Panadero, Ekkehard Pasch, Ignacio Pastor, Andrea Pavone, Ewa Pawelec, Angeles Pedrosa, Valeria Perseo, Byron Peterson, Dirk Pilopp, Fabio Pisano, Maria Ester Piulatti, Gabriel Plunk, Melanie Preynas, Josefine Proll, Aleix Puig Sitjes, Frank Purps, Michael Rack, Kian Rahbarnia, Jörg Riemann, Konrad Risse, Peter Rong, Joachim Rosenberger, Lukas Rudischhauser, Kerstin Rummel, Thomas Rummel, Alexey Runov, Norbert Rust, Leszek Ryc, Haruhiko Saitoh, Shinsuke Satake, Jörg Schacht, Oliver Schmitz, Stefan Schmuck, Bernd Schneider, Matthias Schneider, Wolfgang Schneider, Roman Schrittwieser, Michael Schröder, Timo Schröder, Ralf Schröder, Hans Werner Schu-

macher, Bernd Schweer, Ryoshuke Seki, Priyanjana Sinha, Seppo Sipilae, Christoph Slaby, Håkan Smith, Jorge Sousa, Anett Spring, Brian Standley, Torsten Stange, Adrian Von Stechow, Laurie Stephey, Matthew Stoneking, Uwe Stridde, Yasuhiro Suzuki, Jakob Svensson, Tamas Szabolics, Tamas Szepesi, Henning Thomsen, Jean Marcel Travere, Peter Traverso, Humberto Trimino Mora, Hayato Tsuchiya, Tohru Tsuijmura, Yuriy Turkin, Swetlana Valet, Boudewijn Van Milligen, Luis Vela, Jose Luis Velasco, Maarten Vergote, Michel Vervier, Holger Viebke, Reinhard Vilbrandt, Christian Perez Von Thun, Friedrich Wagner, Erhui Wang, Nengchao Wang, Felix Warmer, Tom Wauters, Lutz Wegener, Thomas Wegner, Gavin Weir, Jörg Wendorf, Uwe Wenzel, Andreas Werner, Yanling Wie, Burkhard Wiegel, Fabian Wilde, Thomas Windisch, Mario Winkler, Victoria Winters, Adelle Wright, Glen Wurden, Pavlos Xanthopoulos, Ichihiro Yamada, Ryo Yasuhara, Masayuki Yokoyama, Daihong Zhang, Manfred Zilker, Andreas Zimbal, Alessandro Zocco, and Sandor Zoletnik. Confirmation of the topology of the Wendelstein 7-X magnetic field to better than 1:100,000. *Nature Communications*, 7, 2016. ISSN 20411723. doi: 10.1038/ncomms13493.

[18] Justin E. Barton, William P. Wehner, Eugenio Schuster, Federico Felici, and Olivier Sauter. Simultaneous closed-loop control of the current profile and the electron temperature profile in the TCV tokamak. *Proceedings of the American Control Conference*, 2015-July(January 2016): 3316–3321, 2015. ISSN 07431619. doi: 10.1109/ACC.2015.7171844.

[19] H. J. De Blank. Plasma equilibrium in tokamaks. *Fusion Science and Technology*, 61(2 T): 89–95, 2012. ISSN 15361055. doi: 10.13182/FST12-A13495.

[20] J. D. Callen, C. C. Hegna, and A. J. Cole. Transport equations in tokamak plasmas. *Physics of Plasmas*, 17(5):056113, May 2010. ISSN 1070-664X, 1089-7674. doi: 10.1063/1.3335486. URL `http://aip.scitation.org/doi/10.1063/1.3335486`.

[21] H. Reimerdes, S. Alberti, P. Blanchard, P. Bruzzone, R. Chavan, S. Coda, B. P. Duval, A. Fasoli, B. Labit, B. Lipschultz, T. Lunt, Y. Martin, J. M. Moret, U. Sheikh, B. Sudki, D. Testa, C. Theiler, M. Toussaint, D. Uglietti, N. Vianello, and M. Wischmeier. TCV divertor upgrade for alternative magnetic configurations. *Nuclear Materials and Energy*, 12:1106–1111, 2017. ISSN 23521791. doi: 10.1016/j.nme.2017.02.013. URL `https://doi.org/10.1016/j.nme.2017.02.013`.

[22] A. Loarte. Effects of divertor geometry on tokamak plasmas. *Plasma Physics and Controlled Fusion*, 43(6), 2001. ISSN 07413335. doi: 10.1088/0741-3335/43/6/201.

[23] L D Horton, G C Vlases, P Andrew, V Bhatnagar, and A Chankin. Studies in JET Divertors of Varied Geometry I : Non Seeded Plasma Operation. (July 1998).

[24] R. A. Pitts, X. Bonnin, F. Escourbiac, H. Frerichs, J. P. Gunn, T. Hirai, A. S. Kukushkin, E. Kaveeva, M. A. Miller, D. Moulton, V. Rozhansky, I. Senichenkov, E. Sytova, O. Schmitz, P. C. Stangeby, G. De Temmerman, I. Veselova, and S. Wiesen. Physics basis for the first ITER tungsten divertor. *Nuclear Materials and Energy*, 20(June):100696, 2019. ISSN 23521791. doi: 10.1016/j.nme.2019.100696. URL `https://doi.org/10.1016/j.nme.2019.100696`.

[25] M. A. Makowski, D. Elder, T. K. Gray, B. Labombard, C. J. Lasnier, A. W. Leonard, R. Maingi, T. H. Osborne, P. C. Stangeby, J. L. Terry, and J. Watkins. Analysis of a multi-machine database on divertor heat fluxes. *Physics of Plasmas*, 19(5), 2012. ISSN 1070664X. doi: 10.1063/1.4710517.

[26] T. Eich, A. W. Leonard, R. A. Pitts, W. Fundamenski, R. J. Goldston, T. K. Gray, A. Herrmann, A. Kirk, A. Kallenbach, O. Kardaun, A. S. Kukushkin, B. Labombard, R. Maingi, M. A. Makowski, A. Scarabosio, B. Sieglin, J. Terry, and A. Thornton. Scaling of the tokamak near the scrape-off layer H-mode power width and implications for ITER. *Nuclear Fusion*, 53 (9), sep 2013. ISSN 00295515. doi: 10.1088/0029-5515/53/9/093031.

[27] D. Silvagni, T. Eich, M. Faitsch, T. Happel, B. Sieglin, P. David, D. Nille, L. Gil, and U. Stroth. Scrape-off layer (SOL) power width scaling and correlation between SOL and pedestal gradients across L, i and H-mode plasmas at ASDEX Upgrade. *Plasma Physics and Controlled Fusion*, 62(4), 2020. ISSN 13616587. doi: 10.1088/1361-6587/ab74e8.

[28] E Havlickova. SOLPS analysis of the MAST-U divertor with the effect of heating power and pumping on the access to detachment in the Super-x configuration. *Plasma Phys. Control. Fusion*, 57, 2015. doi: 10.1088/0741-3335/57/11/115001.

[29] Jan Horacek, Geoffrey Cunningham, Slavomir Entler, Petr Dobias, Richard Duban, Martin Imrisek, Tomas Markovic, Josef Havlicek, and Rustam Enikeev. Feasibility study of fast swept divertor strike point suppressing transient heat fluxes in big tokamaks. *Fusion Engineering and Design*, 123:646–649, 2017. ISSN 09203796. doi: 10.1016/j.fusengdes.2017.01.027. URL `https://doi.org/10.1016/j.fusengdes.2017.01.027`.

[30] Martin J Greenwald, J L Terry, S M Wolfe, S Ejima, M G Bell, S M Kaye, and G H Neilson. A new look at density limits in tokamaks. *Nuclear Fusion*, 28(12):2199, 1988. ISSN 0029-5515. doi: 10.1088/0029-5515/28/12/009. URL `http://stacks.iop.org/0029-5515/28/i=12/a=009`.

[31] A. Loarte, B. Lipschultz, A. S. Kukushkin, G. F. Matthews, P. C. Stangeby, N. Asakura, G. F. Counsell, G. Federici, A. Kallenbach, K. Krieger, A. Mahdavi, V. Philipps, D. Reiter, J. Roth, J. Strachan, D. Whyte, R. Doerner, T. Eich, W. Fundamenski, A. Herrmann, M. Fenstermacher, P. Ghendrih, M. Groth, A. Kirschner, S. Konoshima, B. Labombard, P. Lang, A. W. Leonard, P. Monier-Garbet, R. Neu, H. Pacher, B. Pegourie, R. A. Pitts, S. Takamura, J. Terry, and E. Tsitrone. Chapter 4: Power and particle control. *Nuclear Fusion*, 47(6), 2007. ISSN 00295515. doi: 10.1088/0029-5515/47/6/S04.

[32] B. Lipschultz, B. LaBombard, J. L. Terry, C. Boswell, and I. H. Hutchinson. Divertor physics research on alcator C-Mod. *Fusion Science and Technology*, 51(3):369–389, 2007. ISSN 15361055. doi: 10.13182/FST07-A1428.

[33] A. Kallenbach, M. Bernert, M. Beurskens, L. Casali, M. Dunne, T. Eich, L. Giannone, A. Herrmann, M. Maraschek, S. Potzel, F. Reimold, V. Rohde, J. Schweinzer, E. Viezzer, and M. Wischmeier. Partial detachment of high power discharges in ASDEX Upgrade. *Nuclear Fusion*, 55 (5):1–8, 2015. ISSN 17414326. doi: 10.1088/0029-5515/55/5/053026.

[34] The JET Team. Highly radiating and detached plasmas on carbon and beryllium targets. *Plasma Physics and Controlled Fusion*, 37(11A), 1995. ISSN 07413335. doi: 10.1088/0741-3335/37/11A/015.

[35] A. Kallenbach. H mode discharges with feedback controlled radiative boundary in the ASDEX Upgrade tokamak. *Nucl. Fusion*, 35:1231, 1995.

[36] J. A. Goetz, B. LaBombard, B. Lipschultz, C. S. Pitcher, J. L. Terry, C. Boswell, S. Gangadhara, D. Pappas, J. Weaver, B. Welch, R. L. Boivin, P. Bonoli, C. Fiore, R. Granetz, M. Greenwald, A. Hubbard, I. Hutchinson, J. Irby, E. Marmar, D. Mossessian, M. Porkolab, J. Rice, W. L. Rowan, G. Schilling, J. Snipes, Y. Takase, S. Wolfe, and S. Wukitch. High confinement dissipative divertor operation on Alcator C-Mod. *Physics of Plasmas*, 6(5 I): 1899–1906, 1999. ISSN 1070664X. doi: 10.1063/1.873447.

[37] N Asakura, N Hosogane, K Itami, A Sakasai, S Sakurai, K Shimizu, M Shimada, H Kubo, S Higashijma, H Takenaga, H Tamai, S Konoshima, T Sugie, K Masaki, Y Koide, O Naito, H Shirai, T Takizuka, T Ishijima, S Suzuki, and A Kumagai. Role of divertor geometry on detachment and core plasma performance in JT60U. *Journal of Nuclear Materials*, 266:182–188, 1999. ISSN 00223115. doi: 10.1016/S0022-3115(98)00818-6. URL `http://ac.els-cdn.com/`

`S0022311598008186/1-s2.0-S0022311598008186-main.pdf?_tid=17640c8e-1f7d-11e7-8b72-00000aacb360&acdnat=1492000958_bd1682856c932d9d571db835ff3260c7`.

[38] J. Rapp, P. Monier-Garbet, G. F. Matthews, R. Sartori, P. Andrew, P. Dumortier, T. Eich, W. Fundamenski, M. Von Hellermann, J. Hogan, L. C. Ingesson, S. Jachmich, H. R. Koslowski, A. Loarte, G. Maddison, D. C. McDonald, A. Messiaen, J. Ongena, V. Parail, V. Philipps, G. Saibene, and B. Unterberg. Reduction of divertor heat load in JET ELMy H-modes using impurity seeding techniques. *Nuclear Fusion*, 44(2):312–319, 2004. ISSN 00295515. doi: 10.1088/0029-5515/44/2/013.

[39] G. P. Maddison, C. Giroud, G. K. McCormick, J. A. Alonso, B. Alper, G. Arnoux, P. C. Da Silva Aresta Belo, M. N.A. Beurskens, A. Boboc, S. Brezinsek, I. Coffey, S. Devaux, T. Eich, W. Fundamenski, D. Harting, A. Huber, S. Jachmich, I. Jenkins, E. Joffrin, M. A.H. Kempenaars, M. Lehnen, T. Loarer, P. J. Lomas, A. G. Meigs, P. D. Morgan, V. Riccardo, F. G. Rimini, M. F. Stamp, G. Telesca, and H. Thomsen. Moderation of divertor heat loads by fuelling and impurity seeding in well-confined ELMy H-mode plasmas on JET. *Nuclear Fusion*, 51(4), 2011. ISSN 00295515. doi: 10.1088/0029-5515/51/4/042001.

[40] C. Giroud, G. Maddison, K. McCormick, M. N.A. Beurskens, S. Brezinsek, S. Devaux, T. Eich, L. Frassinetti, W. Fundamenski, M. Groth, A. Huber, S. Jachmich, A. Järvinen, A. Kallenbach, K. Krieger, D. Moulton, S. Saarelma, H. Thomsen, S. Wiesen, A. Alonso, B. Alper, G. Arnoux, P. Belo, A. Boboc, A. Brett, M. Brix, I. Coffey, E. De La Luna, D. Dodt, P. De Vries, R. Felton, E. Giovanozzi, J. Harling, D. Harting, N. Hawkes, J. Hobirk, I. Jenkins, E. Joffrin, M. Kempenaars, M. Lehnen, T. Loarer, P. Lomas, J. Mailloux, D. McDonald, A. Meigs, P. Morgan, I. Nunes, C. Perez Van Thun, V. Riccardo, F. Rimini, A. Sirinnelli, M. Stamp, and I. Voitsekhovitch. Integration of a radiative divertor for heat load control into JET high triangularity ELMy H-mode plasmas. *Nuclear Fusion*, 52(6), 2012. ISSN 00295515. doi: 10.1088/0029-5515/52/6/063022.

[41] F. Reimold, M. Wischmeier, M. Bernert, S. Potzel, D. Coster, X. Bonnin, D. Reiter, G. Meisl, A. Kallenbach, L. Aho-Mantila, and U. Stroth. Experimental studies and modeling of complete H-mode divertor detachment in ASDEX Upgrade. *Journal of Nuclear Materials*, 463:128–134, 2015. ISSN 00223115. doi: 10.1016/j.jnucmat.2014.12.019. URL `http://dx.doi.org/10.1016/j.jnucmat.2014.12.019`.

[42] F. Reimold, M. Wischmeier, M. Bernert, S. Potzel, A. Kallenbach, H. W. Müller, B. Sieglin, and U. Stroth. Divertor studies in nitrogen induced completely detached H-modes in full

tungsten ASDEX Upgrade. *Nuclear Fusion*, 55(3), 2015. ISSN 17414326. doi: 10.1088/0029-5515/55/3/033004.

[43] B. Lipschultz, J. Goetz, B. LaBombard, G. McCracken, J. Terry, D. Jablonski, C. Kurz, A. Niemczewski, and J. Snipes. Plasma-surface interactions in the Alcator C-Mod tokamak. *Journal of Nuclear Materials*, 220-222:967–970, 1995. ISSN 00223115. doi: 10.1016/0022-3115(94)00452-8.

[44] G. M. Mccracken, B. Lipschultz, B. Labombard, J. A. Goetz, R. S. Granetz, D. Jablonski, S. Lisgo, H. Ohkawa, P. C. Stangeby, and J. L. Terry. Impurity screening in Ohmic and high confinement (H-mode) plasmas in the Alcator C-Mod tokamak. *Physics of Plasmas*, 4(5): 1681–1689, 1997. ISSN 10897674. doi: 10.1063/1.872365.

[45] Artur Niemczewski, I. H. Hutchinson, B. LaBombard, B. Lipschultz, and G. M. McCracken. Neutral particle dynamics in the alcator C-MOD tokamak. *Nuclear Fusion*, 37(2):151–163, 1997. ISSN 00295515. doi: 10.1088/0029-5515/37/2/I04.

[46] P. C. Stangeby and D. Moulton. A simple analytic model of impurity leakage from the divertor and accumulation in the main scrape-off layer. *Nuclear Fusion*, 60(10), 2020. ISSN 17414326. doi: 10.1088/1741-4326/ab9e16.

[47] N. Richard, B. Terreault, E. Haddad, J. Gunn, G. Abel, S. Chiu, J. L. Gauvreau, H. H. Mai, and W. W. Zuzak. Retention of Ne and N2 in the closed and pumped TdeV divertor with attached and detached plasmas. *Journal of Nuclear Materials*, 241-243:760–764, 1997. ISSN 00223115. doi: 10.1016/s0022-3115(97)80136-5.

[48] J. A. Goetz, B. Lipschultz, C. S. Pitcher, J. L. Terry, P. T. Bonoli, J. E. Rice, and S. J. Wukitch. Impurity compression and enrichment studies on Alcator C-Mod. *Journal of Nuclear Materials*, 266:354–359, 1999. ISSN 00223115. doi: 10.1016/S0022-3115(98)00582-0.

[49] A. Sakasai, H. Takenaga, N. Hosogane, S. Sakurai, N. Akino, H. Kubo, S. Higashijima, H. Tamai, N. Asakura, K. Itami, and K. Shimizu. Helium exhaust in ELMy H-mode plasmas with W-shaped pumped divertor of JT-60U. *Journal of Nuclear Materials*, 266:312–317, 1999. ISSN 00223115. doi: 10.1016/S0022-3115(98)00580-7.

[50] H. S. Bosch, W. Ullrich, D. Coster, O. Gruber, G. Haas, J. Neuhauser, R. Schneider, and R. Wolf. Helium transport and exhaust with an ITER-like divertor in ASDEX Upgrade. *Journal of Nuclear Materials*, 290-293:836–839, 2001. ISSN 00223115. doi: 10.1016/S0022-3115(00)00539-0.

[51] M. Groth, P. Andrew, W. Fundamenski, H. Y. Guo, D. L. Hillis, J. T. Hogan, L. D. Horton, G. F. Matthews, A. G. Meigs, P. M. Morgan, M. F. Stamp, and M. Von Hellermann. Noble gas enrichment studies at JET. *Journal of Nuclear Materials*, 290-293:867–871, 2001. ISSN 00223115. doi: 10.1016/S0022-3115(00)00652-8.

[52] D. Eldon, E. Kolemen, J. L. Barton, A. R. Briesemeister, D. A. Humphreys, A. W. Leonard, R. Maingi, M. A. Makowski, A. G. McLean, A. L. Moser, and P. C. Stangeby. Controlling marginally detached divertor plasmas. *Nuclear Fusion*, 57(6), 2017. ISSN 17414326. doi: 10.1088/1741-4326/aa6b16.

[53] C. Guillemaut, M. Lennholm, J. Harrison, I. Carvalho, D. Valcarcel, R. Felton, S. Griph, C. Hogben, R. Lucock, G. F. Matthews, C. Perez Von Thun, R. A. Pitts, and S. Wiesen. Real-time control of divertor detachment in H-mode with impurity seeding using Langmuir probe feedback in JET-ITER-like wall. *Plasma Physics and Controlled Fusion*, 59(4), 2017. ISSN 13616587. doi: 10.1088/1361-6587/aa5951.

[54] A. Kallenbach, R. Dux, J. C. Fuchs, R. Fischer, B. Geiger, L. Giannone, A. Herrmann, T. Lunt, V. Mertens, R. McDermott, R. Neu, T. Pütterich, S. Rathgeber, V. Rohde, K. Schmid, J. Schweinzer, and W. Treutterer. Divertor power load feedback with nitrogen seeding in ASDEX Upgrade. *Plasma Physics and Controlled Fusion*, 52(5), 2010. ISSN 07413335. doi: 10.1088/0741-3335/52/5/055002.

[55] M. Bernert, T. Eich, A. Burckhart, J. C. Fuchs, L. Giannone, A. Kallenbach, R. M. McDermott, and B. Sieglin. Application of AXUV diode detectors at ASDEX Upgrade. *Review of Scientific Instruments*, 85(3), 2014. ISSN 10897623. doi: 10.1063/1.4867662.

[56] D. Eldon, E. Kolemen, D. A. Humphreys, A. W. Hyatt, A. E. Järvinen, A. W. Leonard, A. G. McLean, A. L. Moser, T. W. Petrie, and M. L. Walker. Advances in radiated power control at DIII-D. *Nuclear Materials and Energy*, 18(July 2018):285–290, 2019. ISSN 23521791. doi: 10.1016/j.nme.2019.01.010. URL `https://doi.org/10.1016/j.nme.2019.01.010`.

[57] Harshita Raj. Improved Heat and Particle Flux Mitigation in High Core Confinement,Baffled, Alternate Divertor Configurations in theTCV tokamak. pages 9–25, 2019.

[58] J. R. Harrison, W. A.J. Vijvers, C. Theiler, B. P. Duval, S. Elmore, B. Labit, B. Lipschultz, S. H.M. van Limpt, S. W. Lisgo, C. K. Tsui, H. Reimerdes, U. Sheikh, K. H.A. Verhaegh, and M. Wischmeier. Detachment evolution on the TCV tokamak. *Nuclear Materials and Energy*, 12:1071–1076, 2017. ISSN 23521791. doi: 10.1016/j.nme.2016.10.020.

[59] T. Ravensbergen, M. Van Berkel, S. A. Silburn, J. R. Harrison, A. Perek, K. Verhaegh, W. A.J. Vijvers, C. Theiler, A. Kirk, M. R. De Baar, The Eurofusion Mst1 Team, and The Tcv Team. Development of a real-time algorithm for detection of the divertor detachment radiation front using multi-spectral imaging. *Nuclear Fusion*, 60(6), 2020. ISSN 17414326. doi: 10.1088/1741-4326/ab8183.

[60] T Ravensbergen, M van Berkel, A. Perek, C. Galperti, B.P. Duval, O. Fevrier, R.J.R. van Kampen, F. Felici, J.T. Lammers, C. Theiler, Johan Schoukens, B. Linehan, M. Komm, S. Henderson, D. Brida, and M.R. de Baar. Real-time feedback control of the impurity emission front in tokamak divertor plasmas. *Nature Energy*, Submitted(2021):1–11, 2020. ISSN 2041-1723. doi: 10.1038/s41467-021-21268-3. URL `http://dx.doi.org/10.1038/s41467-021-21268-3`.

[61] T Ravensbergen, M van Berkel, A. Perek, C. Galperti, B.P. Duval, O. Fevrier, R.J.R. van Kampen, F. Felici, J.T. Lammers, C. Theiler, Johan Schoukens, B. Linehan, M. Komm, S. Henderson, D. Brida, and M.R. de Baar. Real-time feedback control of the impurity emission front in tokamak divertor plasmas. *Nature Energy*, 12(1105):1–11, 2021. ISSN 2041-1723. doi: 10.1038/s41467-021-21268-3. URL `http://dx.doi.org/10.1038/s41467-021-21268-3`.

[62] A. Loarte, R. D. Monk, J. R. Martín-Solís, D. J. Campbell, A. V. Chankin, S. Clement, S. J. Davies, J. Ehrenberg, S. K. Erents, H. Y. Guo, P. J. Harbour, L. D. Horton, L. C. Ingesson, H. Jäckel, J. Lingertat, C. G. Lowry, C. F. Maggi, G. F. Matthews, K. McCormick, D. P. O'Brien, R. Reichle, G. Saibene, R. J. Smith, M. F. Stamp, D. Stork, and G. C. Vlases. PLasma detachment in JET mark I divertor experiments. *Nuclear Fusion*, 38(3):331–371, 1998. ISSN 00295515. doi: 10.1088/0029-5515/38/3/303.

[63] A. R. Field, I. Balboa, P. Drewelow, J. Flanagan, C. Guillemaut, J. R. Harrison, A. Huber, V. Huber, B. Lipschultz, G. Matthews, A. Meigs, J. Schmitz, M. Stamp, and N. Walkden. Dynamics and stability of divertor detachment in H-mode plasmas on JET. *Plasma Physics and Controlled Fusion*, 2017. ISSN 13616587. doi: 10.1088/1361-6587/aa764c.

[64] Jean Jacquinot, Martin Keilhacker, and Paul-Henri Rebut. Chapter 2: Mission and Highlights of the JET Joint Undertaking: 1978-1999. *Fusion Science and Technology*, 53(4):866–890, May 2008. ISSN 1536-1055, 1943-7641. doi: 10.13182/FST08-A1742. URL `https://www.tandfonline.com/doi/full/10.13182/FST08-A1742`.

[65] R. J. Goldston, M. L. Reinke, and J. A. Schwartz. A new scaling for divertor detachment.

Plasma Physics and Controlled Fusion, 59(5), mar 2017. ISSN 13616587. doi: 10.1088/1361-6587/aa5e6e.

[66] P. M. Valanju, M. Kotschenreuther, S. M. Mahajan, and J. Canik. Super-X divertors and high power density fusion devices. *Physics of Plasmas*, 16(5), 2009. ISSN 1070664X. doi: 10.1063/1.3110984.

[67] D. D. Ryutov. Geometrical properties of a "snowflake" divertor. *Physics of Plasmas*, 14(6), 2007. ISSN 1070664X. doi: 10.1063/1.2738399.

[68] D. E. Post. A review of recent developments in atomic processes for divertors and edge plasmas. *Journal of Nuclear Materials*, 220-222:143–157, 1995. ISSN 00223115. doi: 10.1016/0022-3115(94)00453-6.

[69] G. M. McCracken, M. F. Stamp, R. D. Monk, A. G. Meigs, J. Lingertat, R. Prentice, A. Starling, R. J. Smith, and A. Tabasso. Evidence for volume recombination in JET detached divertor plasmas. *Nuclear Fusion*, 38(4):619–629, 1998. ISSN 00295515. doi: 10.1088/0029-5515/38/4/311.

[70] S. I. Krasheninnikov, A. Yu Pigarov, D. A. Knoll, B. LaBombard, B. Lipschultz, D. J. Sigmar, T. K. Soboleva, J. L. Terry, and F. Wising. Plasma recombination and molecular effects in tokamak divertors and divertor simulators. *Physics of Plasmas (1994-present)*, 4(1997):1638–1646, 1997. ISSN 1070-664X, 1089-7674. doi: 10.1063/1.872268. URL `http://scitation.aip.org/content/aip/journal/pop/4/5/10.1063/1.872268\%5Cnhttp://scitation.aip.org/deliver/fulltext/aip/journal/pop/4/5/1.872268.pdf?itemId=/content/aip/journal/pop/4/5/10.1063/1.872268&mimeType=pdf&containerItemId=content/aip/journal/pop`.

[71] M Groth, E M Hollmann, A E Jaervinen, A W Leonard, A G Mclean, C M Samuell, D Reiter, S L Allen, P Boerner, S Brezinsek, I Bykov, G Corrigan, M E Fenstermacher, D Harting, C J Lasnier, B Lomanowski, M A Makowski, M W Shafer, H Q Wang, J G Watkins, S Wiesen, and R S Wilcox. EDGE2D-EIRENE predictions of molecular emission in DIII-D high-recycling divertor plasmas. *Nuclear Materials and Energy*, 19(February):211–217, 2019. ISSN 2352-1791. doi: 10.1016/j.nme.2019.02.035.

[72] U. Fantz. Basics of plasma spectroscopy. *Plasma Sources Science and Technology*, 15(4), jun 2006. ISSN 09630252. doi: 10.1088/0963-0252/15/4/S01.

[73] Open-adas. University of Strathclyde ADAS project, 2018. URL `http://open.adas.ac.uk/`.

[74] Wiese W L, Fuhr J R, and Deters T M. Atomic Transition. Probabilities of Carbon, Nitrogen, and Oxygen — A Critical Data Compilation, 1996.

[75] P. C. Stangeby. *The plasma boundary of magnetic fusion devices.* Plasma physics series. Institute of Physics Pub, Bristol ; Philadelphia, 2000. ISBN 978-0-7503-0559-4.

[76] S I Krasheninnikov and A S Kukushkin. Physics of ultimate detachment of a tokamak divertor plasma. 2017. doi: 10.1017/S0022377817000654.

[77] G Federici, C H Skinner, J N Brooks, J P Coad, C Grisolia, A A Haasz, A Hassanein, V Philipps, C S Pitcher, J Roth, W R Wampler, and D G Whyte. Plasma–material interactions in current tokamaks and their implications for next step fusion reactors. *Nuclear Fusion*, 41(12):172, 2001.

[78] P.C. Stangeby and G.M. McCracken. Plasma boundary phenomena in tokamaks. *Nuclear Fusion*, 30(7):1225–1379, July 1990. ISSN 0029-5515, 1741-4326. doi: 10.1088/0029-5515/30/7/005. URL `https://iopscience.iop.org/article/10.1088/0029-5515/30/7/005`.

[79] P. C. Stangeby. Basic physical processes and reduced models for plasma detachment. *Plasma Physics and Controlled Fusion*, 60(4), 2018. ISSN 13616587. doi: 10.1088/1361-6587/aaacf6.

[80] S I Krasheninnikov, A S Kukushkin, and A A Pshenov. Divertor plasma detachment. 055602 (May), 2016. doi: 10.1063/1.4948273. URL `http://dx.doi.org/10.1063/1.4948273`.

[81] G. S. Xu, Q. P. Yuan, K. D. Li, L. Wang, J. C. Xu, Q. Q. Yang, Y. M. Duan, L. Y. Meng, Z. S. Yang, F. Ding, J. B. Liu, H. Y. Guo, H. Q. Wang, D. Eldon, Y. Q. Tao, K. Wu, N. Yan, R. Ding, Y. F. Wang, Y. Ye, L. Zhang, T. Zhang, Q. Zang, Y. Y. Li, H. Q. Liu, G. Z. Jia, X. J. Liu, H. Si, E. Z. Li, L. Zeng, J. P. Qian, S. Y. Lin, L. Q. Xu, H. H. Wang, X. Z. Gong, and B. N. Wan. Divertor impurity seeding with a new feedback control scheme for maintaining good core confinement in grassy-ELM H-mode regime with tungsten monoblock divertor in EAST. *Nuclear Fusion*, 60(8), 2020. ISSN 17414326. doi: 10.1088/1741-4326/ab91fa.

[82] P. C. Stangeby and Chaofeng Sang. Strong correlation between D 2 density and electron temperature at the target of divertors found in SOLPS analysis. *Nuclear Fusion*, 57(5), 2017. ISSN 17414326. doi: 10.1088/1741-4326/aa5e27.

[83] B. Lipschultz, J. L. Terry, C. Boswell, J. A. Goetz, A. E. Hubbard, S. I. Krasheninnikov, B. LaBombard, D. A. Pappas, C. S. Pitcher, F. Wising, and S. Wukitch. The role of particle

sinks and sources in Alcator C-Mod detached divertor discharges. *Physics of Plasmas*, 6(5 I): 1907–1916, 1999. ISSN 1070664X. doi: 10.1063/1.873448.

[84] A A Pshenov, A S Kukushkin, and S I Krasheninnikov. Energy balance in plasma detachment. *Nuclear Materials and Energy*, 12:948–952, 2017. ISSN 2352-1791. doi: 10.1016/j.nme.2017.03.019. URL `https://doi.org/10.1016/j.nme.2017.03.019`.

[85] A. Kallenbach, M. Bernert, R. Dux, F. Reimold, and M. Wischmeier. Analytical calculations for impurity seeded partially detached divertor conditions. *Plasma Physics and Controlled Fusion*, 58(4):45013, 2016. ISSN 13616587. doi: 10.1088/0741-3335/58/4/045013. URL `http://dx.doi.org/10.1088/0741-3335/58/4/045013`.

[86] A. Loarte. Understanding the edge physics of divertor experiments by comparison of 2D edge code calculations and experimental measurements. *Journal of Nuclear Materials*, 241-243: 118–134, 1997. ISSN 00223115. doi: 10.1016/s0022-3115(97)80035-9.

[87] A Scarabosio, M Groth, M Wischmeier, and F Reimold. SOL parallel momentum loss in ASDEX Upgrade and comparison with SOLPS. 12:181–186, 2017. doi: 10.1016/j.nme.2017.01.026.

[88] A. Fil, B. Dudson, B. Lipschultz, D. Moulton, K. Verhaegh, O. Fevrier, and M. Wensing. Identification of the primary processes that lead to the drop in divertor target ion current at detachment in TCV. *Contributions to Plasma Physics*, 58(6-8):746–750, 2018. ISSN 15213986. doi: 10.1002/ctpp.201700171.

[89] K. Verhaegh, B. Lipschultz, B. P. Duval, O. Février, A. Fil, C. Theiler, M. Wensing, C. Bowman, D. S. Gahle, J. R. Harrison, B. Labit, C. Marini, R. Maurizio, H. De Oliveira, H. Reimerdes, U. Sheikh, C. K. Tsui, N. Vianello, and W. A.J. Vijvers. An improved understanding of the roles of atomic processes and power balance in divertor target ion current loss during detachment. *Nuclear Fusion*, 59(12), 2019. ISSN 17414326. doi: 10.1088/1741-4326/ab4251.

[90] D Moulton, P C Stangeby, X Bonnin, and R A Pitts. Comparison between SOLPS-4 . 3 and the Lengyel Model for ITER baseline neon-seeded plasmas. (20):1–30.

[91] D. Moulton, J. Harrison, B. Lipschultz, and D. Coster. Using SOLPS to confirm the importance of parallel area expansion in Super-X divertors. *Plasma Phys. Control. Fusion*, 59(6), 2017.

[92] Xavier BONNIN, Wouter DEKEYSER, Richard PITTS, David COSTER, Serguey

VOSKOBOYNIKOV, and Sven WIESEN. Presentation of the New SOLPS-ITER Code Package for Tokamak Plasma Edge Modelling. *Plasma and Fusion Research*, 11(0):1403102–1403102, 2016. ISSN 1880-6821. doi: 10.1585/pfr.11.1403102.

[93] K. Jesko, Y. Marandet, H. Bufferand, J. P. Gunn, H. J. van der Meiden, and G. Ciraolo. Soledge2D-Eirene simulations of the Pilot-PSI linear plasma device compared to experimental data. *Contributions to Plasma Physics*, 58(6-8):798–804, 2018. ISSN 15213986. doi: 10.1002/ctpp.201700186.

[94] Scott Silburn. Calcam. Zenodo, 2018.

[95] A. Huber, S. Brezinsek, Ph Mertens, B. Schweer, G. Sergienko, A. Terra, G. Arnoux, N. Balshaw, M. Clever, T. Edlingdon, S. Egner, J. Farthing, M. Hartl, L. Horton, D. Kampf, J. Klammer, H. T. Lambertz, G. F. Matthews, C. Morlock, A. Murari, M. Reindl, V. Riccardo, U. Samm, S. Sanders, M. Stamp, J. Williams, K. D. Zastrow, and C. Zauner. Development of a mirror-based endoscope for divertor spectroscopy on JET with the new ITER-like wall (invited). *Review of Scientific Instruments*, 83(10), 2012. ISSN 00346748. doi: 10.1063/1.4731759.

[96] Ralph Dux. Diagnostics of Fusion Plasmas. In *IPP Summer School*, 2009.

[97] Z. Zhang. A Flexible New Technique for Camera Calibration. *Microsoft Research*, 1998.

[98] G. Bradski. The OpenCV Library. *Dr. Dobb's Journal of Software Tools*, 2000.

[99] T. Odstrčil, T. Pütterich, M. Odstrčil, A. Gude, V. Igochine, U. Stroth, and ASDEX Upgrade Team. Optimized tomography methods for plasma emissivity reconstruction at the ASDEX Upgrade tokamak. *Review of Scientific Instruments*, 87(12):123505, December 2016. ISSN 0034-6748, 1089-7623. doi: 10.1063/1.4971367. URL `http://aip.scitation.org/doi/10.1063/1.4971367`.

[100] A. H. Andersen and A. C. Kak. Similtaneous Algebraic Reconstruction Technique (SART): A Superior Implementation Of The Art Algorithm. *Ultrasonic Imaging*, 6:81–94, 1984. ISSN 1559-6915. doi: 10.1145/2387358.2387363.

[101] S Arshad, R Budny, JG Cordey, V Drozdov, S Gerasimov, DC McDonald, A Murari, V Riccardo, I Voitsekhovich, and Others. Consistency of Stored Energy Measurements on JET. *EFDA Report*, (05), 2004. URL `http://www.iop.org/Jet/fulltext/EFDC050250.pdf`.

[102] G. S. Kirnev, G. Corrigan, D. Coster, S. K. Erents, W. Fundamenski, G. F. Matthews, and R. A. Pitts. EDGE2D code simulations of SOL flows and in-out divertor asymmetries in JET.

Journal of Nuclear Materials, 337-339(1-3 SPEC. ISS.):271–275, 2005. ISSN 00223115. doi: 10.1016/j.jnucmat.2004.09.032.

[103] A E Hubbard. Physics and scaling of the H-mode pedestal. *Plasma Physics and Controlled Fusion*, 42(5A):A15–A35, May 2000. ISSN 0741-3335, 1361-6587. doi: 10.1088/0741-3335/42/5A/302. URL `https://iopscience.iop.org/article/10.1088/0741-3335/42/5A/302`.

[104] D B Schaeffer, D S Montgomery, A S Bondarenko, L A Morton, R P Johnson, T Shimada, C G Constantin, E T Everson, S A Letzring, S A Gaillard, K A Flippo, S H Glenzer, and C Niemann. Thomson Scattering Measurements of Temperature and Density in a Low-Density, Laser-Driven Magnetized Plasma. *Journal of Instrumentation*, 7(02):P02002–P02002, February 2012. ISSN 1748-0221. doi: 10.1088/1748-0221/7/02/P02002. URL `https://iopscience.iop.org/article/10.1088/1748-0221/7/02/P02002`.

[105] W. P. West, C. J. Lasnier, T. A. Casper, T. H. Osborne, K. H. Burrell, P. B. Snyder, D. M. Thomas, E. J. Doyle, and A. W. Leonard. Pedestal profiles during QH-mode operation on DIII-D. *Plasma Physics and Controlled Fusion*, 46(5 SUPPL. A), 2004. ISSN 07413335. doi: 10.1088/0741-3335/46/5A/019.

[106] R. J. Groebner and T. H. Osborne. Scaling studies of the high mode pedestal. *Physics of Plasmas*, 5(5 PART 1):1800–1806, 1998. ISSN 1070664X. doi: 10.1063/1.872849.

[107] M. Brix, D. Dodt, A. Korotkov, P. Morgan, D. Dunai, R. Fischer, A. Meigs, I. S. Nedzelskiy, J. Schweinzer, J. Vince, and S. Zoletnik. Upgrade of the lithium beam diagnostic at JET. *Review of Scientific Instruments*, 81(10):1–4, 2010. ISSN 00346748. doi: 10.1063/1.3502320.

[108] A. M. Howald, J. M. McChesney, and W. P. West. The TEXT neutral lithium beam edge density diagnostic. *Review of Scientific Instruments*, 66(1):312–314, 1995. ISSN 00346748. doi: 10.1063/1.1146487.

[109] H. J. Hartfuss, T. Geist, and M. Hirsch. Heterodyne methods in millimetre wave plasma diagnostics with applications to ECE, interferometry and reflectometry. *Plasma Physics and Controlled Fusion*, 39(11):1693–1769, 1997. ISSN 07413335. doi: 10.1088/0741-3335/39/11/001.

[110] S. S. Henderson, M. Bernert, S. Brezinsek, M. Carr, M. Cavedon, R. Dux, B. Lipschultz, M. G. O'Mullane, F. Reimold, and M. L. Reinke. Determination of volumetric plasma parameters from spectroscopic N II and N III line ratio measurements in the ASDEX Upgrade divertor. *Nuclear Fusion*, 58(1):0–10, 2018. ISSN 17414326. doi: 10.1088/1741-4326/aa96be.

[111] S. K. Rathgeber, R. Fischer, S. Fietz, J. Hobirk, A. Kallenbach, H. Meister, T. Pütterich, F. Ryter, G. Tardini, and E. Wolfrum. Estimation of profiles of the effective ion charge at ASDEX Upgrade with Integrated Data Analysis. *Plasma Physics and Controlled Fusion*, 52 (9), 2010. ISSN 07413335. doi: 10.1088/0741-3335/52/9/095008.

[112] D. Brunner, S. M. Wolfe, B. Labombard, A. Q. Kuang, B. Lipschultz, M. L. Reinke, A. Hubbard, J. Hughes, R. T. Mumgaard, J. L. Terry, and M. V. Umansky. Surface heat flux feedback controlled impurity seeding experiments with Alcator C-Mod's high-Z vertical target plate divertor: Performance, limitations and implications for fusion power reactors. *Nuclear Fusion*, 57(8), 2017. ISSN 17414326. doi: 10.1088/1741-4326/aa7923.

[113] S. S. Henderson, M. Bernert, S. Brezinsek, M. Carr, M. Cavedon, R. Dux, D. S. Gahle, J. Harrison, A. Kallenbach, B. Lipschultz, B. Lomanowski, A. Meigs, M. O'Mullane, F. Reimold, M. L. Reinke, and S. Wiesen. An assessment of nitrogen concentrations from spectroscopic measurements in the JET and ASDEX upgrade divertor. *Nuclear Materials and Energy*, 18: 147–152, jan 2019. ISSN 23521791. doi: 10.1016/j.nme.2018.12.012.

[114] A. Kallenbach. Overview of ASDEX Upgrade results. *Nuclear Fusion*, 47(10), 2017. ISSN 00295515. doi: 10.1088/0029-5515/47/10/S11.

[115] V. I. Demidov, S. V. Ratynskaia, and K. Rypdal. Electric probes for plasmas: The link between theory and instrument. *Review of Scientific Instruments*, 73(10):3409, 2002. ISSN 00346748. doi: 10.1063/1.1505099.

[116] M. R.K. Wigram, C. P. Ridgers, B. D. Dudson, J. P. Brodrick, and J. T. Omotani. Incorporating nonlocal parallel thermal transport in 1D ITER SOL modelling. *Nuclear Fusion*, 60(7), 2020. ISSN 17414326. doi: 10.1088/1741-4326/ab868b.

[117] E. Militello-Asp, G. Corrigan, P da Silva Aresta Belo, L. Garzotti, and D. Harting. ITER Fuelling Requirements and Scenario Development for H , He and DT through JINTRAC. *26th IAEA Fusion Energy Conference (Kyoto, Japan, 17–22 October)*, (19):1–8, 2016.